Brno University of Technology
Faculty of Mechanical Engineering
Institute of Machine and Industrial Design

Vysoké učení technické v Brně
Fakulta strojního inženýrství
Ústav konstruování

RESEARCH AND DEVELOPMENT OF ADDITIVELY MANUFACTURED LATTICE STRUCTURES

VÝZKUM A VÝVOJ ADITIVNĚ VYRÁBĚNÝCH MIKRO-PRUTOVÝCH STRUKTUR

Ing. Jan Jaroš
Author
Autor práce

doc. Ing. Daniel Koutný, Ph.D.
Supervisor
Vedoucí práce

Dissertation Thesis
Dizertační práce

Brno 2025

Brno University of Technology
Faculty of Mechanical Engineering
Institute of Machine and Industrial Design

Vysoké učení technické v Brně
Fakulta strojního inženýrství
Ústav konstruování

RESEARCH AND DEVELOPMENT OF ADDITIVELY MANUFACTURED LATTICE STRUCTURES

VÝZKUM A VÝVOJ ADITIVNĚ VYRÁBĚNÝCH MIKRO-PRUTOVÝCH STRUKTUR

Ing. Jan Jaroš
Author
Autor práce

doc. Ing. Daniel Koutný, Ph.D.
Supervisor
Vedoucí práce

Dissertation Thesis
Dizertační práce

Brno 2025

STATEMENT

I hereby declare that I have written the PhD thesis *Research and development of additively manufactured lattice structures* on my own according to advice of my supervisor doc. Ing. Daniel Koutný, Ph.D., and using the sources listed in the references.

Brno, _____ .....

Ing. Jan Jaroš

BIBLIOGRAPHICAL REFERENCE

JAROŠ, J. *Research and development of additively manufactured lattice structures*. Brno, 2025, 132 p. PhD thesis. Brno University of Technology, Faculty of Mechanical Engineering, Institute of Machine and Industrial Design. Supervisor: doc. Ing. Daniel Koutny, Ph.D.

ACKNOWLEDGEMENT

I would like to thank all the people who have supported me during my doctoral studies. First of all, I would like to thank my supervisor doc. Daniel Koutný, Ph.D., who supported and guided me throughout my doctoral studies. I would like to thank my colleagues from the RIAT group who were able to help me solve problems. Many thanks to my family, friends and especially my wife for her tireless support. Without them, completing my studies would not have been possible.

ABSTRACT

Developments in additive technologies have enabled the production of porous lattice structures from a wide range of metal alloys. These can be used to replace solid material and produce components with significantly reduced mass or higher heat dissipation. In addition, the combination of lattice structures and magnesium alloys potentially enables the production of biodegradable implants that promote bone tissue ingrowth and exhibit mechanical properties close to those of bone tissue due to the magnesium alloy. For the potential application of such components in various industries, it is necessary to ensure high-quality production. This is associated with a high relative material density, low surface roughness and high dimensional accuracy. Lattice structures are difficult to process after production, which places high demands on the production itself. Laser powder bed fusion need the selection of suitable process parameters that lead to a minimization of imperfections. This dissertation therefore focuses on the production of lattice structures with the aim of minimizing imperfections as much as possible. The geometry of the lattice structures is divided into smaller parts in order to understand the influence of the manufacturing parameters on the formation of imperfections. In the first phase, manufacturing is focused on the strut geometry. The contour strategy is used, which seems to be suitable for manufacturing parts with low volume and round cross-section. As this is the base part of the structure, a good processable aluminum alloy AlSi10Mg is used to understand well the effects of the process parameters. The next phase focuses on the geometry of the unit cell, for which the magnesium alloy WE43 is used. In the last phase, the effect of contour and hatch strategies on the imperfections and mechanical properties of the lattice structures produced from WE43 magnesium alloy is investigated. The results confirm that by adjusting the process parameters, it is possible to produce lattice structures even from a difficult-to-process material such as a magnesium alloy. The relative density of the material reached more than 99.5% and the Young's modulus was 40 GPa. The described effects of the process parameters on the formation of imperfections could therefore help to ensure that porous structures can be used for more applications in the future.

KEYWORDS

Laser beam powder bed fusion, lattice structures, aluminum alloy, magnesium alloy, material quality, relative material density, surface roughness, dimensional accuracy, mechanical properties

ABSTRAKT

Vývoj v oblasti aditivních technologií umožnil výrobu porézních mikro-prutových struktur z široké škály kovových slitin. Ty je možné použít jako náhradu plného materiálu a vyrábět tak díly s výraznou úsporou hmotnosti, nebo vyšším odvodem tepelné energie. Spojení mikro-prutových struktur a hořčíkových slitin navíc potenciálně umožňuje výrobu biodegradabilních implantátů, které svojí strukturou podpoří prorůstání kostní tkáně a zároveň budou mít mechanické vlastnosti blízké kostní tkáni díky hořčíkové slitině. Pro potenciální aplikaci takových dílů v různých průmyslových odvětvích je nutné zajistit vysokou kvalitu výroby. Ta je spojená s vysokou relativní hustotou materiálu, nízkou drsností povrchu a vysokou přesností. V případě mikro-prutových struktur, které jsou obtížně opracovatelné po výrobě, to klade vysoké požadavky na samotnou výrobu. V případě laserové fúze s práškovým ložem jde o vhodné zvolení procesních parametrů vedoucí k minimalizaci imperfekcí. Proto se disertační práce zaměřuje na výrobu mikro-prutových struktur s cílem maximální minimalizace imperfekcí. Geometrie mikro-prutových struktur je rozdělena na menší části s cílem pochopit vliv výrobních parametrů na vznik imperfekcí. V první fázi je výroba zaměřena na geometrii prutu, kde je použita contour strategie, která se jeví jako vhodná pro výrobu nízko-objemových dílů s kulatým průřezem. Jelikož se jedná o základní část struktury, je použita dobře zpracovatelná hliníková slitina AlSi10Mg, aby bylo možné vlivy procesních parametrů dobře objasnit. Další fáze je zaměřena na geometrii základní buňky, kde je použita hořčíková slitina WE43. V poslední fázi je zkoumán vliv contour a hatch skenovacích strategií na imperfekce a mechanické vlastnosti mikro-prutových struktur vyrobených z hořčíkové slitiny WE43. Výsledky potvrzují, že vhodným nastavením procesních parametrů je možné vyrábět mikro-prutové struktury i z obtížně zpracovatelného materiálu jakým je hořčíková slitina. Relativní hustota materiálu dosahovala více než 99.5% a Youngův modul byl 40 GPa. Popsané vlivy procesních parametrů na vznik imperfekcí by tak mohly v budoucnu přispět k rozšíření porézních struktur do více aplikací.

KLÍČOVÁ SLOVA

Laserová fúze s práškovým ložem, mikro-prutové struktury, hliníkové slitiny, hořčíkové slitiny, kvalita materiálu, relativní hustota materiálu, drsnost povrchu, rozměrová přesnost, mechanické vlastnosti

CONTENT

1 INTRODUCTION

Additive manufacturing of metal components is being used more and more frequently in many companies. The main advantage is that components can be customized to specific requirements without incurring additional tooling costs or production delays. Additive technology enables the production of complex components with specific shapes, as production constraints are lower compared to traditional methods. The material is added layer by layer until the entire component is finished. This process minimizes material waste and the impact on the environment. In addition, complex components can be produced that are difficult to manufacture using conventional methods. For this reason, additive manufacturing is used in many industrial sectors such as the automotive, aerospace and medical industries.

Lattice structures can be produced with the advantages of additive manufacturing. They consist of thin struts that are stacked into a pattern defined by a unit cell. The simple geometry based on the struts makes it easy to modify them as required. Due to the small volume of material, large surface area and precise layout, they can be used in many applications where the aim is to reduce mass, increase heat dissipation or improve energy absorption.

One of the additive manufacturing technologies that can be used to produce lattice structures is laser beam powder bed fusion (PBF-LB). Thanks to the high-energy laser and the protective atmosphere, perspective materials such as magnesium alloys can be processed. Due to their good strength-to-weight ratio, damping characteristics and thermal conductivity, they are already used in many sectors such as the automotive and aerospace industries. In addition, magnesium alloys are biocompatible and have mechanical properties close to those of human bone, making them a promising material for biomedical applications.

Magnesium alloy lattice structures can combine the advantages of both, such as the mass reduction, structural design and biodegradability of magnesium. Potential applications may include biodegradable implants that reduce the need for reoperation. However, the complexity of the lattice structures makes them even more susceptible to imperfections such as material porosity, rough surfaces and dimensional inaccuracies. High demands are therefore placed on production quality. In the case of PBF-LB, the small volume of the lattice structures makes their production complicated and requires special adjustment of the process parameters. This effect is even more magnified by magnesium alloys, which have a low melting point. Therefore, this dissertation focuses on the new approach of selecting process parameters based on the specific geometry of samples representing lattice structures. As a result, the quality of the produced lattice structures can be improved, which supports the use of lattice structures in the optimization of components and their use in industrial applications.

2 STATE OF THE ART

2.1 Laser Beam Powder Bed Fusion

Laser Beam Powder Bed Fusion (PBF-LB) technology is based on melting powder particles into the shape of the finished part [1]. The technology uses the high energy of the laser to melt powder particles of various materials from aluminum alloys to titanium. The cross-section of the part is built up layer by layer [2]. The quality of the manufactured part depends on many factors such as the shape of the part, the quality of the powder material, the stability of the production process and the process parameters [3–6]. These factors influence the formation of pores in the material, the surface roughness and the dimensional accuracy.

Factors related to the PBF-LB process include oxidation of the material, the balling effect, temperature fluctuations and the loss of alloying elements. These factors mainly lead to poor bonding between the layers, low relative material density, instability of the laser tracks, cracking and delamination of the layers [7–9]. In order to understand the factors, mechanism of melt pool solidification, consistency and quality of manufactured parts, various parameters of PBF-LB production and their influence on material properties were identified (Fig. 2-1) [10]. Suitable combinations of process parameters, powder preheating, laser strategy and protective gas can reduce imperfections in the production of parts using the PBF-LB process [11, 12].

Parameters	Material properties
Controlled	Viscosity
Laser scanners	Surface tension
Laser power	Particle size distribution
Mechanical layering of powder	Particle shape
Atmospheric control	Absorptivity/reflectivity
Air flow	Thermal conductivity
Heaters (bed temperature)	Specific heat
Machine-specific	Emissivity
Laser type	Melting temperature
Scan radius	
Geometry-specific	
Scan vector length	

Fig. 2-1 Overview of the parameters that influence the material properties [10]

2.1.1 Energy of process parameters

When considering the factors of SLM production, the thesis focuses on the effects of the process parameters in relation to the laser and laser scanning. Different PBF-LB process parameters lead to different performances of the produced parts. Therefore, the energy of process parameters is often used to describe the influence of several process parameters[13–16]. Usually, three equations are used. The linear energy takes into account the laser power and the laser speed (Equation 1). The area energy describes the effect of laser exposure in the 3D, therefore the hatch distance is taken into account (Equation 2). The volume energy also takes into account the layer thickness used for PBF-LB production (Equation 3). The equations are as follows:

$$\mathrm{E_{lin}} = \frac{\mathrm{LP}}{\mathrm{LS}}\ (\mathrm{J \cdot mm^{-1}}) \tag{1}$$

, where E_{lin} is linear energy ($J \cdot mm^{-1}$), *LP* is laser power (W), *LS* is laser speed ($mm \cdot s^{-1}$)

$$\mathrm{E}_{area} = \frac{\mathrm{LP}}{\mathrm{LS \cdot HD}}\ (\mathrm{J \cdot mm^{-2}}) \tag{2}$$

, where E_{area} is area energy ($J \cdot mm^{-2}$), *LP* is laser power (W), *LS* is laser speed ($mm \cdot s^{-1}$), *HD* is hatch distance (mm)

$$\mathrm{E}_{vol} = \frac{\mathrm{LP}}{\mathrm{LS \cdot HD \cdot LT}}\ (\mathrm{J \cdot mm^{-3}}) \tag{3}$$

, where Eobj is volume energy ($J \cdot mm^{-1}$), LP is laser power (W), LS is laser speed ($mm \cdot s^{-1}$), HD is hatch distance (mm), LT is powder layer thickness (mm)

Usually, the energies are used to describe the formation of single welds. Low energy results in discontinuous welds that are insufficient to join the welds and build up the part. Low energy results in high porosity of the material and poor surface quality. On the other hand, high energy leads to a large width of the weld with insufficient height. High energy can also lead to the vaporization of alloying elements and thus to the formation of pores [17, 18].

2.2 Lattice structures

The porous structures can be divided into many categories, such as natural or man-made, open or closed, random or periodic, 2D or 3D, etc. (Fig. 2-2) [19]. The natural structures can be found in wood, butterfly wings, mushrooms or corals [20, 21]. The man-made structures are mainly inspired by the structures in the nature, such as the honeycomb structure (Fig. 2-2n) or the lattice structures inspired by crystal grid (Fig. 2-2i, j, k, l). The main advantage of these structures is the weight reduction and the possibility to adjust the mechanical properties depending on the load. In addition, the surface area of the structures is larger, making them suitable for coolers due to their high heat dissipation rate [22]. PBF-LB production of the structured part also leads to a reduction in material consumption and a reduction in production time [23].

In PBF-LB production of porous structures, one of the biggest challenges is to produce high quality lattice structures. Melting the powder material with a high-power laser can lead to imperfections such as porosity, rough surface and dimensional inaccuracies. To minimize these imperfections, the appropriate process parameters must be defined [24].

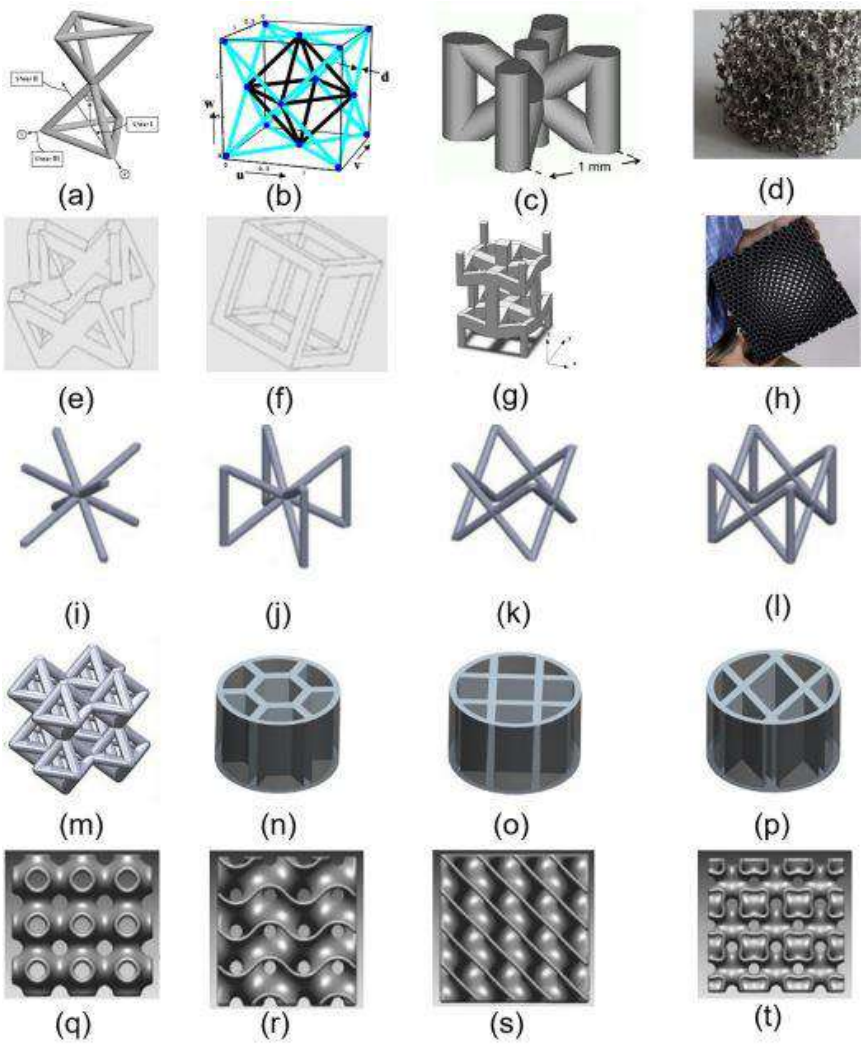

Fig. 2-2 Examples of one cell topologies: (a) Kagome, (b) Octet, (c) MS1, (d) Stochastic foam, (e) Pilar textile, (f) Square collinear/cubic, (g) Re-entrant auxetic, (h) Spatially variant self-collimating lattice, (i) Body-centered cubic, (j) Body-centered cubic with vertical struts, (k) Face-centered cubic, (l) Face-centered cubic with vertical struts, (m) Octahedron, (n) Honeycomb, (o) Square, (p) Diamond, (q) TPMS P-type, (r) TPMS gyroid, (s) TPMS D-type, (t) TPMS I-WP type [19]

2.2.1 Limitations

Lattice structures are composed of unit cells. The unit cell is defined as a cube with a certain dimension. In the unit cell, the arrangement of the struts defines the geometry of the lattice structure (Fig. 2-3) [25]. The typical arrangement of unit cells corresponds to the geometry of body-centered cubic (BCC) and face-centered cubic (FCC) cells. These geometries are often supplemented by struts in the vertical direction. The PBF-LB production of lattice structures has a limitation in the production of horizontal struts. In the case of BCC lattice structures, the struts are inclined at an angle of 35.26°. The limit of PBF-LB production without support is basically known as an inclination of 45° [26]. For the production of lattice structures, the supports cannot be used because it is not possible to remove supports within the structure.

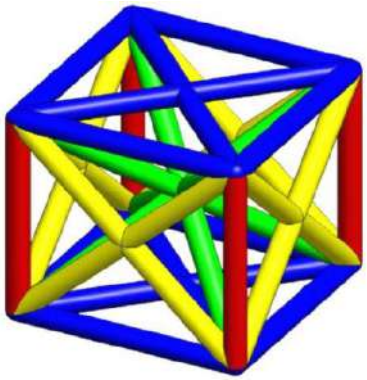

Fig. 2-3 Arrangement of struts in the unit cell: BCC – green, FCC – yellow, vertical struts – red, horizontal struts - blue [26]

2.2.2 Heat dissipation

In order to ensure sufficient quality of the lattice structures produced with PBF-LB, the inclination of the struts and the volume of the struts must be taken into account. In the case of an inclination, the vertical struts dissipate the heat (induced by a high-power laser) mainly via the previously produced material (Fig. 2-4a). Only small amounts of heat are dissipated via the surrounding powder particles. Inclined struts also dissipate the heat mainly via the previously produced material. However, the temperature gradient runs in a vertical direction, which has an effect on the downskin of the inclined strut (Fig. 2-4b) [27, 28].

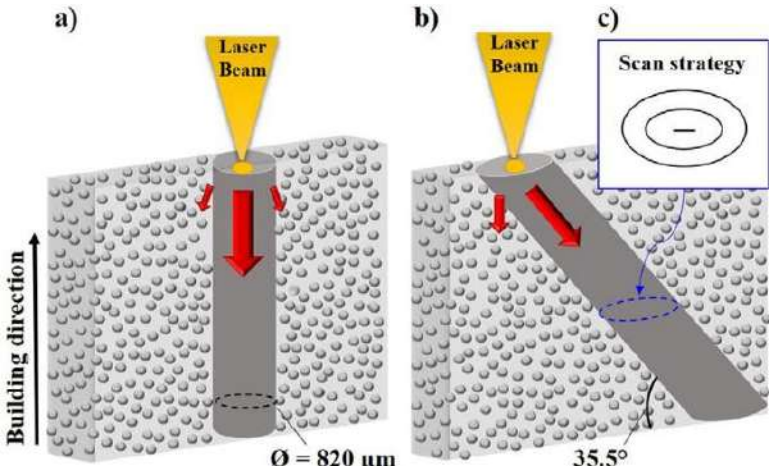

Fig. 2-4 Heat dissipation for: (a) vertical, (b) inclined struts [27]

The material in the inclined part of the struts is kept at a high temperature over a long period of time. This leads to the formation of pores due to the vaporization of alloying elements. In addition, the material of the struts can lead to two areas with different relative material density and microstructure due to the different dissipation rate (Fig. 2-5b). The upskin area contains a small number of pores and has a fine microstructure (Fig. 2-5c-A), which corresponds to the situation in the vertical struts (Fig. 2-5a). The downskin area contains many pores and has a coarse cellular dendritic microstructure (Fig. 2-5c-B). Heat dissipation also occurs via the surrounding powder particles, which have a low heat dissipation rate due to the point contact between the rounded particles. Therefore, the powder particles are partially melted and bonded to the surface of the inclined struts [16, 27, 28].

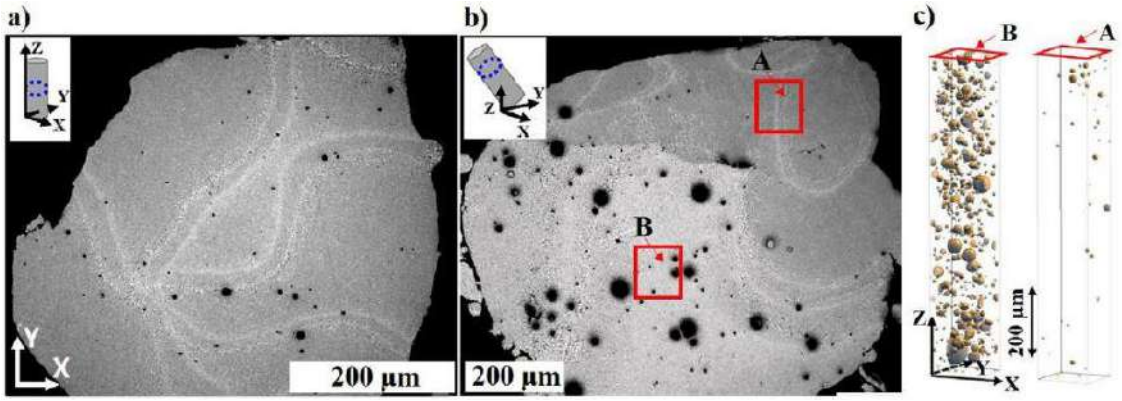

Fig. 2-5 Pores contained in the: (a) vertical strut, (b) inclined strut, (c) pores in the upskin area A and downskin area B of the inclined strut [27]

Heat dissipation is also influenced by the volume of material in the lattice structures, as shown by Dong et al. [29]. The vertical struts with diameters of 4 and 5 mm resulted in a coarse cellular-dendritic microstructure with a low occurrence of pores. The process parameters were optimized for the bulk samples. The heat dissipation rate was suitable for samples with this volume; therefore, the relative material density of the struts was above 99.88%. At smaller strut diameters (1, 2 and 3 mm), the heat dissipation rate was lower, resulting in a fine cellular dendritic microstructure, but the occurrence of pores was higher. The relative material density was between 99.43-98.13%. (Fig. 2-6)

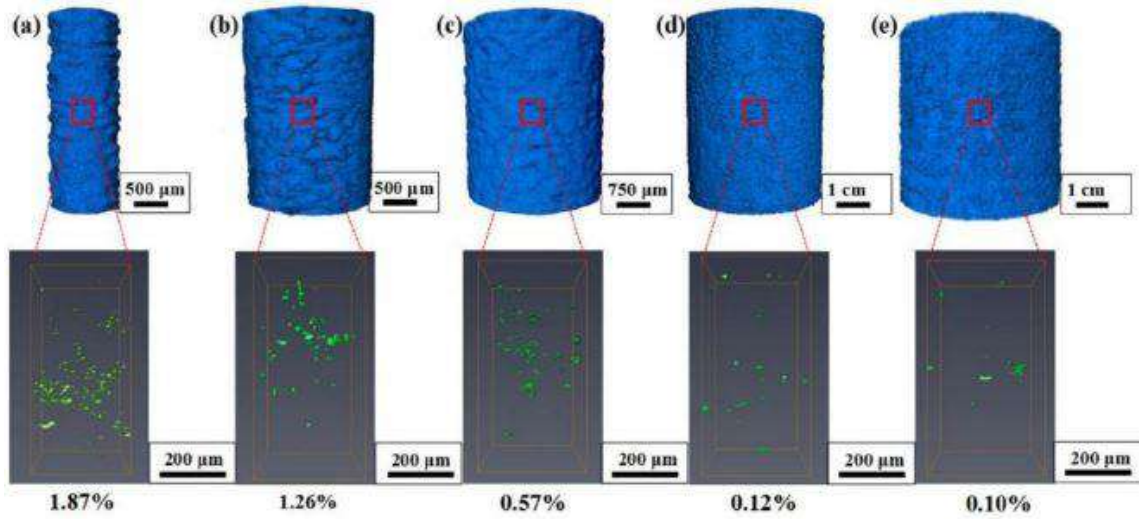

Fig. 2-6 Porosity of vertical struts produced with same process parameters for diameters of: (a) 1 mm; (b) 2 mm; (c) 3 mm; (d) 4 mm; (e) 5 mm [29]

2.2.3 Influence of process parameters

Relative material density

The process parameters influence the formation of pores. Qiu et al. [30] described the influence of laser power and laser speed on the relative material density. Diamond lattice structures produced with PBF-LB with a nominal diameter of 0.3 mm were analyzed. The laser power (Fig. 2-7a) and laser speed (Fig. 2-7b) showed a similar dependence on the pore formation, especially on the relative material density. Low and high laser power and laser speed led to a high relative material density. Low energy of the process parameters was sufficient for low volume samples to melt the powder particles without imperfections. At high energy, the height of the welds is reduced below the layer thickness in many cases. However, the depth of the welds increases. This situation resulted in a higher layer thickness being applied, which is why the high energy is required to melt the powder particles. The medium energy causes vaporization of the material, which leads to circular gas pores.

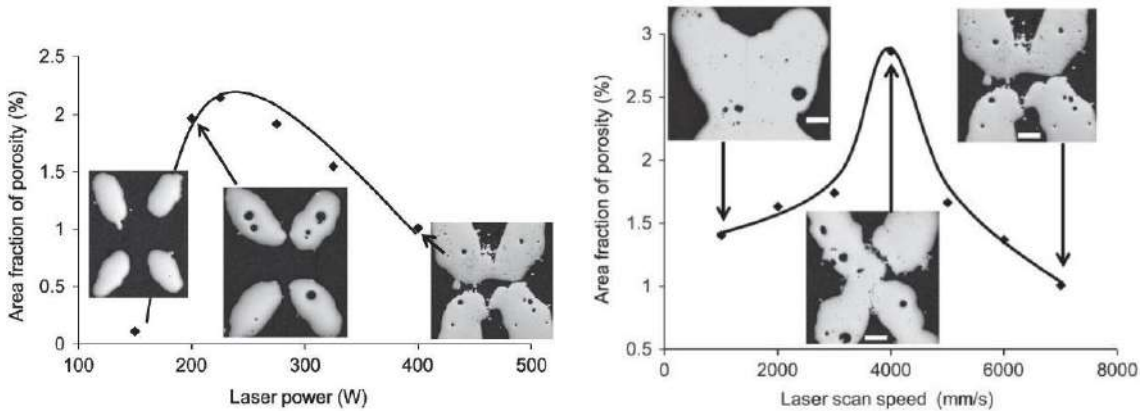

(a) **(b)**

Fig. 2-7 Relative material density of diamond lattice structures dependent on: (a) laser power with constant laser speed of 7000 mm/s (b) laser speed with constant laser power of 400 W [30]

Aboulkhair et al. [4] reduced the relative material density by adjusting the hatch distance (Fig. 2-8). The connection between two neighboring welds is also crucial. A high hatch distance resulted in an insufficient connection and irregular pores between the welds. The smaller hatch distance resulted in a higher relative material density (over 97%). Although the relative material density was higher, the large pores in the material remained. The authors [31–33] achieved a relative material density of over 99% by adjusting the hatch distance.

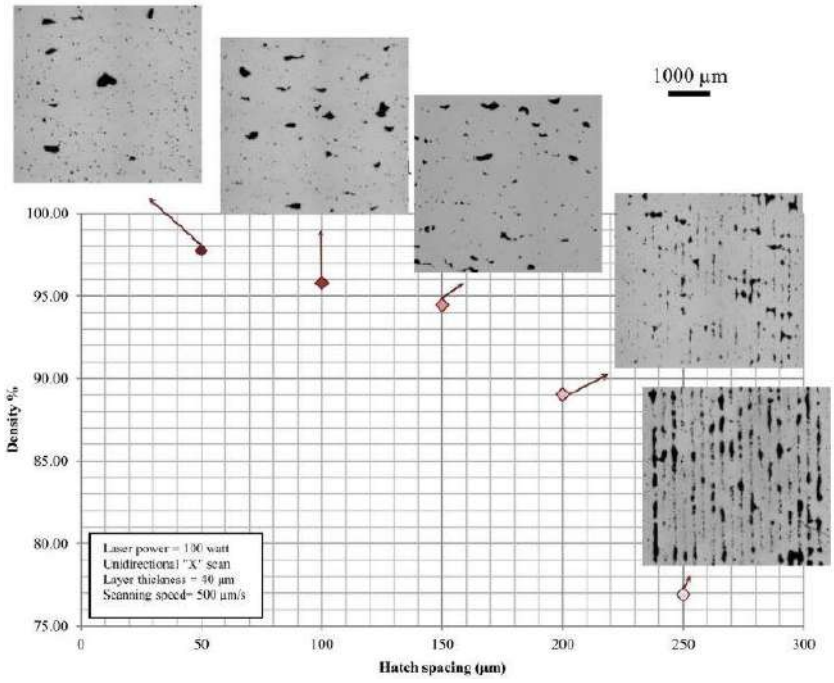

Fig. 2-8 Influence of hatch distance on pores formation between welds [4]

The small volume of lattice structures makes them susceptible to pore formation. In addition, the pores reduce the load-bearing diameter of the struts and can lead to cracking during loading, especially cyclic loading [34, 35]. The shape of the pores can be used to determine dangerous pores. Nudelis et al. [36] used data from CT scans to sort the pores according to compactness and sphericity (Fig. 2-9). Compactness is determined as the volume of the pore distributed in space (Equation 4). The ratio between pore volume and pore surface area is referred to as sphericity (Equation 5). The dangerous pores are in the range of 0-0.5 of compactness and sphericity. The pores with higher stress concentrations were located in this range. In order to determine sufficient process parameters, the number of dangerous pores should be minimized.

$$\Psi = \frac{S_n}{S_{pore}} = \frac{\sqrt[3]{36\Pi V_{pore}^2}}{S_{pore}} \tag{4}$$

$$\Omega = \frac{V_{pore}}{V_n} = \frac{V_{pore}}{\frac{4}{3}\Pi R_{pore}^3} \tag{5}$$

, where S_n represents surface area of a sphere with the same volume (mm^2), S_{pore} pore surface area (mm^2), V_{pore} pore volume (mm^3), V_n volume of sphere.

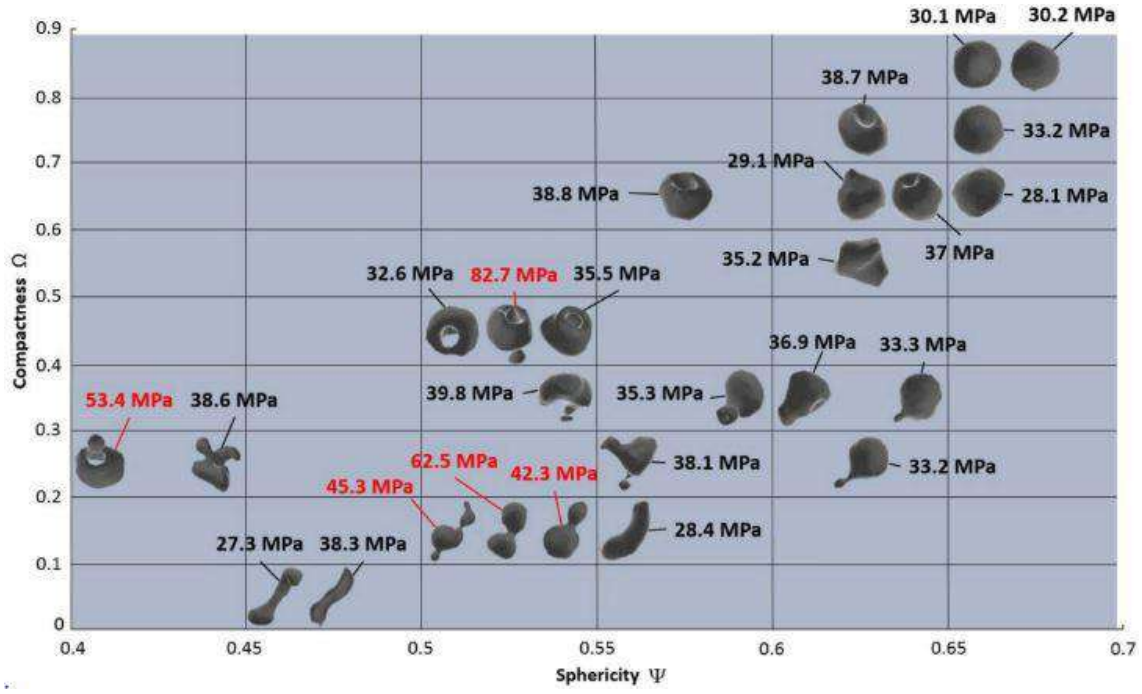

Fig. 2-9 Stress concentration for different shapes of pores determined by compactness and sphericity [36]

Surface roughness

Another important imperfection that occurs in PBF-LB production is the rough surface. The layer-by-layer production process in additive manufacturing technology leads to a staircase effect (Fig. 2-10a). The next layer is built on top of the previous one, but in the case of the inclined part, the new layer is partially produced on top of the powder. This effect causes melting or partial melting of the powder particles, which are melted into or bonded to the surface of the inclined parts [37]. The lower the angle of inclination and the higher the energy of the process parameters, the higher the surface roughness (Fig. 2-10b) as reported by the authors [16, 38]. The staircase effect is mainly observed in the upskin area, where the surface roughness increases slightly with the lower inclination angle. In the case of downskin area the increasing surface roughness is mainly due to the binding of partially melted powder particles on the surface of the part. The opposite phenomenon was observed by Han et al. [37]. They found that a higher amount of bonded powder particles on the downskin of the part can lead to a lower surface roughness. The molten material flows between the powder particles and fills the gaps (Fig. 2-10a).

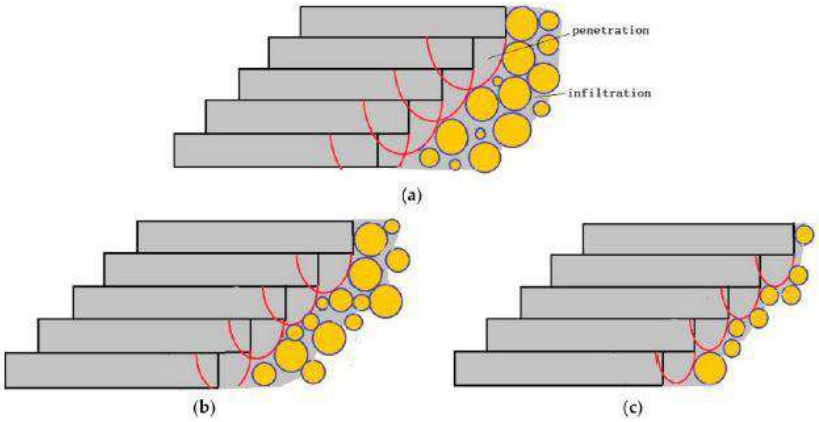

(a)

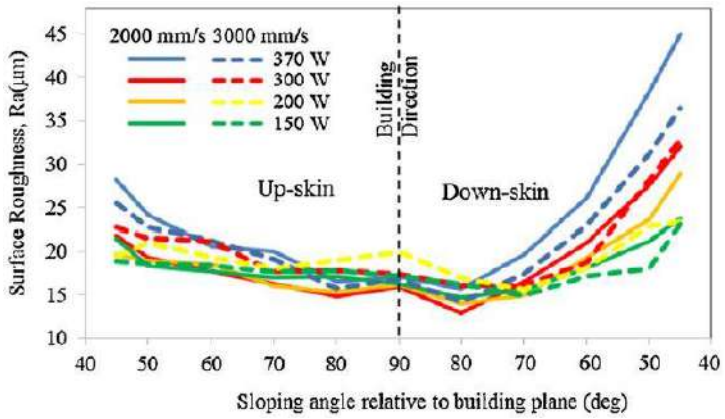

(b)

Fig. 2-10 (a) visualization of staircase effect and powder particles bonded on the downskin area of part [37] (b) influence of process parameters and inclination on surface roughness [38]

Dimensional accuracy

The dimensional accuracy is influenced by the heat dissipation and the process parameters used in PBF-LB production. The authors [39–41] have shown that the heat dissipation in the lattice structures influences the geometry of the lattice structures. The high temperature in the downskin area of lattice structures [27] led to melting of the surrounding powder particles, which increased the size of the material. This effect led to an elliptical cross-section shape of the inclined struts (Fig. 2-11). The more material means a higher weight and leads to different mechanical properties [42].

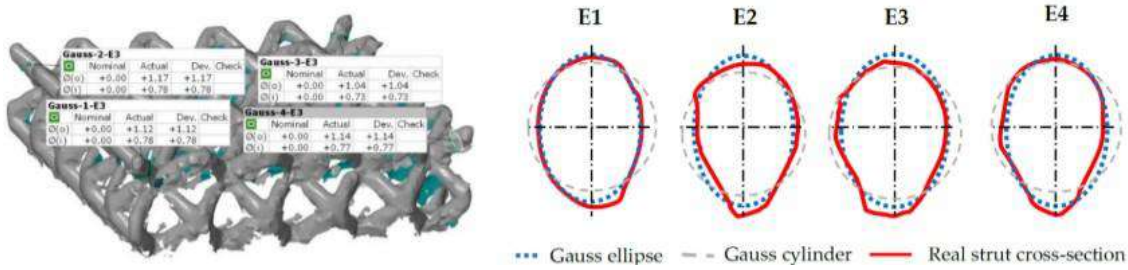

Fig. 2-11 Elliptical cross section of the inclined struts [42]

Qiu et al. [30] described the influence of laser speed and laser power on the real diameter of diamond lattice structures with a nominal diameter of 0.3 mm. At a constant laser power of 400 W and a laser speed of over 4000 mm/s, a minimum diameter of 0.5-0.6 mm was achieved (Fig. 2-12a). A lower laser speed increased the diameter up to 0.8 mm. The constant laser speed of 7000 mm/s and increasing laser power led to an increase in the strut diameter (Fig. 2-12b). The range of diameters was between 0.25 and 0.55 mm. The higher energy of the process parameters caused the melting of a larger amount of powder particles, which led to an increase in the strut diameters.

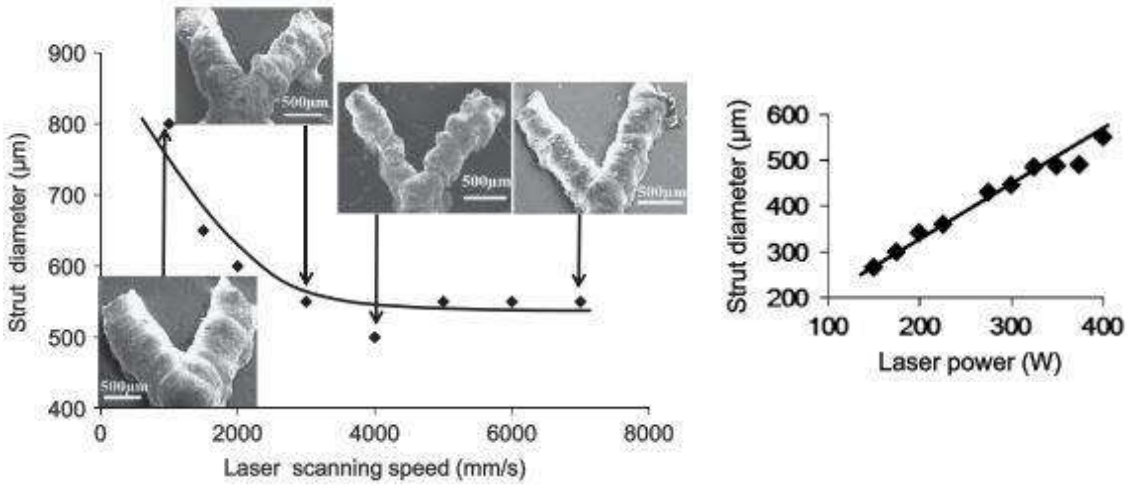

(a) **(b)**

Fig. 2-12 (a) influence of strut diameter on laser speed with constant laser power of 400W; (b) influence strut diameter on laser power with constant laser speed of 7000 mm/s [30]

2.2.4 Laser strategies

The laser strategies define the trajectory of the laser for each layer during PBF-LB production. The laser strategy also influences the formation of defects. Pauly et al. [6] used three scanning strategies to produce struts with a diameter of 3 mm (Fig. 2-13). One of the strategies was the chessboard strategy (Fig. 2-13c, d) which is based on the principle of dividing the cross-section into small square regions that are melted by a laser. The regions are melted in a specific sequence to give the material time to dissipate the heat. This strategy requires a special adjustment of the process parameters to minimize the formation of pores at the boundaries of the regions. The chessboard strategy is mainly used for large-volume parts. In the case of lattice structures, the cross-sections have a small volume, which is not ideal for this strategy.

The contour strategy consists of concentric laser trajectories (Fig. 2-13a, b). Therefore, this strategy is suitable for circular or elliptical cross-sections of the vertical or inclined struts in the lattice structure. The pores were mainly distributed between the laser trajectories. These pores can be reduced by a suitable hatch distance between the laser trajectories [16].

The hatch (meander) laser strategy hatches the cross sections with the parallel laser trajectories (Fig. 2-13e, f). One contour trajectory is used for the edge of the cross-sections. The parallel laser trajectories rotate 67° in each layer, which ensures a uniform microstructure. This strategy is commonly used for the production of PBF-LB parts. Therefore, powder manufacturers recommend this laser strategy and their process parameters they have developed for powder processing. This strategy resulted in irregularly shaped pores in the strut, which are crucial for the mechanical performance of the lattice structures.

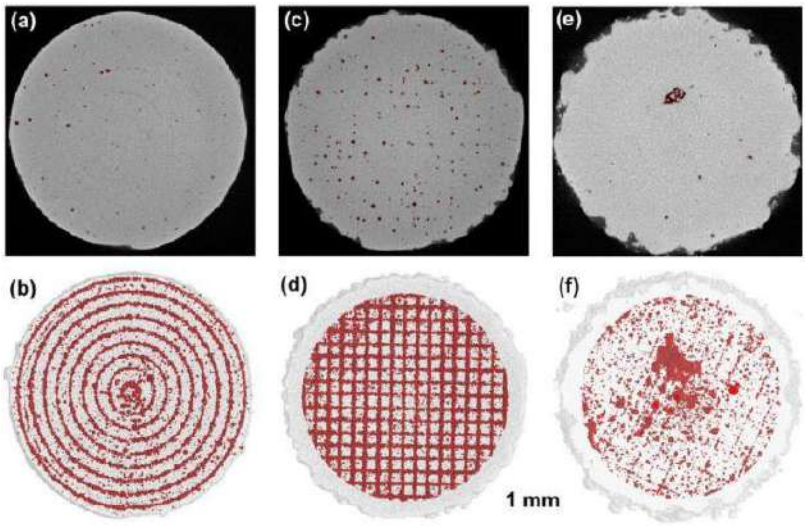

Fig. 2-13 Porosity distribution in struts for: (a); (b) contour strategy; (c); (d) chessboard strategy; (e); (f) hatch strategy [6]

The hatch strategy is particularly susceptible to pore formation in the border area [43]. This is due to the acceleration and deceleration of the laser at the ends of the trajectories. The movements of the laser are controlled by a high-precision electro-optical galvanometer system. The galvanometer mirrors need a certain amount of time to accelerate and decelerate. This occurs at the beginning and end of the trajectory, where the speed of the laser is not constant [44].

In this case, skywriting can be used to extend the laser trajectories (Fig. 2-14) beyond the cross section [45]. The extended trajectories are used to accelerate and decelerate the laser, the laser therefore has a constant velocity in the cross-section. This measure reduces the formation of pores at the beginning and end of the laser trajectories.

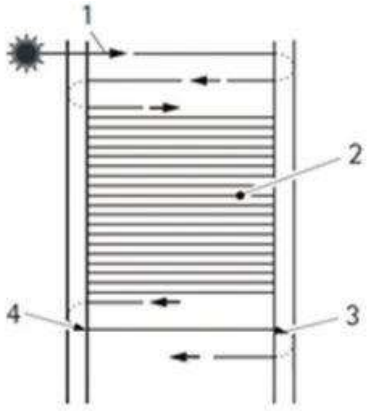

Fig. 2-14 Schematic representation of skywriting used for hatch strategy [45]

2.2.5 Mechanical performance

The mechanical performance of the lattice structures is strongly influenced by the PBF-LB imperfections that occur during fabrication. Gibson et al. [46] determined a material model that takes into account the mechanical properties of the structures. The material model was based on the cell topology, the mechanical properties of the parent material and the relative density of the structure, which is defined as a percentage of the material volume in the unit cell [47, 48].

In the study, the topology of the body-centered cubic (BCC) lattice structure is considered. The BCC lattice structure consists of struts with inclination angle of 35.5% [49]. The inclination angle represents the most unfavorable case of lattice structures; therefore, the production imperfections have the greatest impact on the mechanical performance. Moreover, according to Maxwell's criterion [50], the BCC topology represents a bending-dominated deformation mechanism, which is less effective in load transfer than the stretching-dominated cell topologies [51].

Dong et al. [29, 52] observed the influence of strut diameter and strut inclination on mechanical properties. The authors used a set of process parameters to observe only the influence of diameter and inclination. The smaller strut diameter led to a decrease in mechanical properties (Fig. 2-15a, b), i.e. modulus of elasticity (E), ultimate tensile strength (UTS), yield strength (YS) and elongation (EL). The modulus of elasticity E (Young's modulus) decreased by about 30% as the diameter decreased from 5 mm to 1 mm. The same effect was observed with a decreasing angle of inclination (Fig. 2-15c, d). The Young's modulus decreased by about 12% from the vertical strut to the strut produced with an inclination angle of 35.5%. The mechanical properties might have been influenced by imperfections such as lower relative material density at lower diameter and inclination angle, as observed by other authors [27, 38].

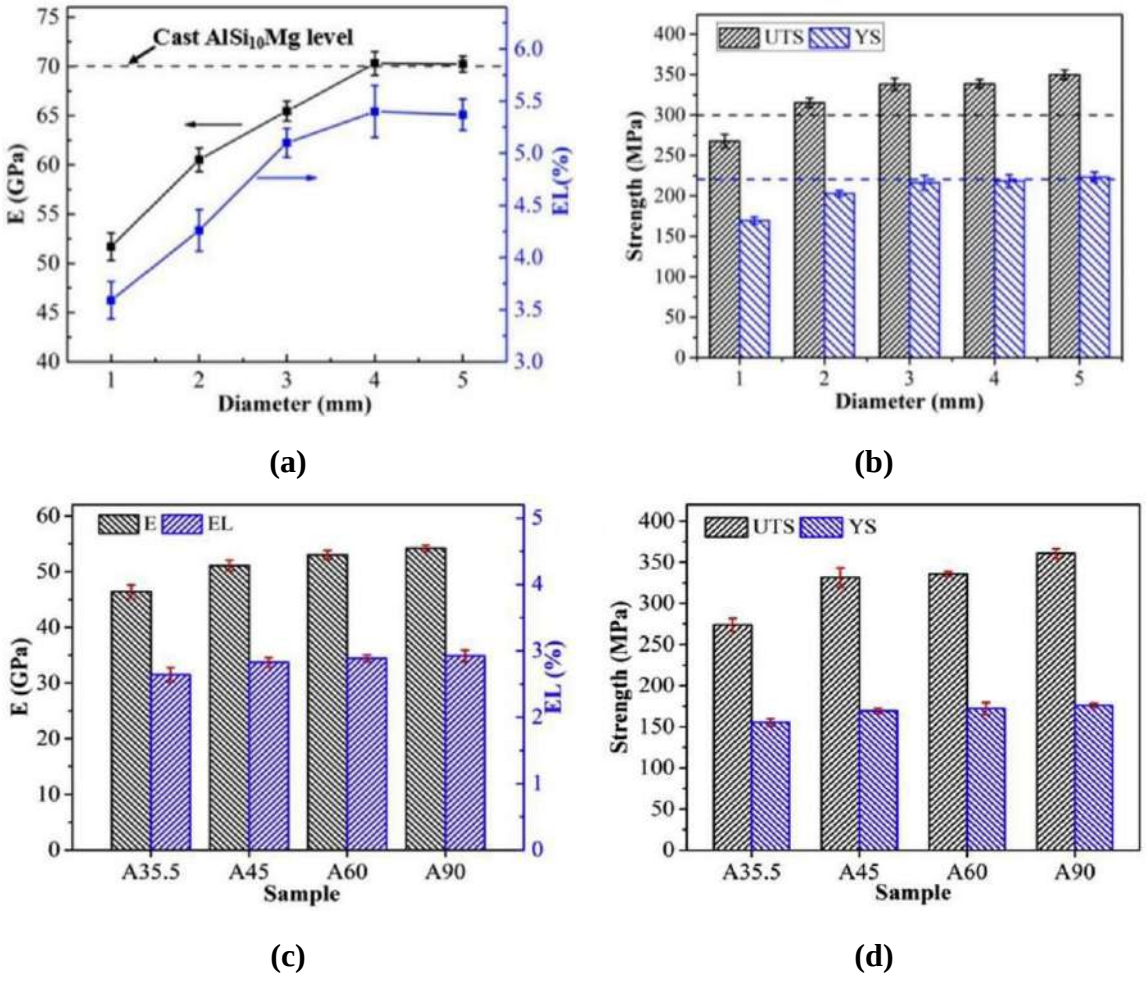

Fig. 2-15 (a), (b) influence of strut diameter on the tensile mechanical properties [29]; (c), (d) influence of strut inclination on the tensile mechanical properties [52]

To determine the mechanical properties of lattice structures, the different samples must be used. The authors [53, 54] modified typical tensile specimens to multi-struts specimens. The multi-strut specimen represented the deformation behavior of the lattice structures. Červinek et al. [54] obtained a good correlation between simulation and experiment in compressive loading of lattice structures when the mechanical properties were measured on the multi-struts tensile specimens. These results were used by Vaverka et al. [55] to determine the actual Young's modulus of lattice structures from the compressive deformation of lattice structures. The actual Young's modulus of lattice structures was determined by comparing the effective elastic modulus of simulation and experiment, where the Young's modulus was a variable in the simulation. The Young's modulus can be effectively used to determine the performance of lattice structures as only the performance of the material is considered.

2.3 Material

2.3.1 Aluminum alloys

Due to their excellent strength-to-weight ratio, ease of processing, good corrosion resistance and thermal conductivity, aluminum alloys are suitable for many applications in the aerospace, automotive and marine industries [56–59]. In the case of PBF-LB technology, aluminum alloys are widely used materials. Processing is very well managed, and powder manufacturers often offer process parameters that lead to high material quality.

For new aluminum alloys, the perspective process parameters are defined based on the process parameter window (Fig. 2-16). Maamoun et al. [5] produced cubes to determine the influence of process parameters on dimensional accuracy (Fig. 2-16b), relative material density (Fig. 2-16c) and surface roughness Ra (Fig. 2-16d). All three parameters showed a similar dependence on the energy of the process parameters. Low energy led to smaller dimensions, low relative material density and high surface roughness. This is mainly related to the balling effect and insufficient bonding between the laser tracks [60, 61]. Higher energy resulted in larger dimensions, high relative material density and low surface roughness. The optimal process parameters were determined based on the cross-section of the three windows (Fig. 2-16a) mentioned above.

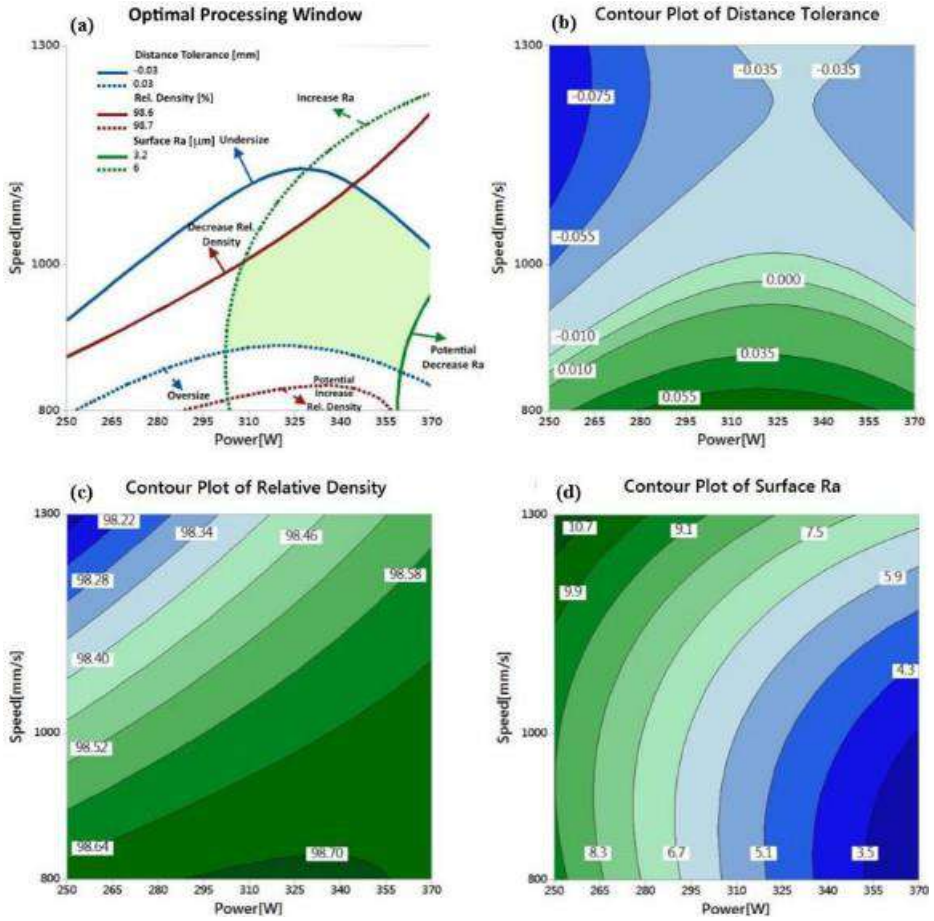

Fig. 2-16 Process parameters window for AlSi10Mg aluminum alloy: (a) optimal processing window, (b) dimensional accuracy, (c) relative material density, (d) surface roughness Ra [5]

However, the optimum window of process parameters has been determined. The final process parameters depend on the machine, the powder and also the geometry of the samples, as will be mentioned in further sections.

2.3.2 Magnesium alloys

Magnesium (Mg) and its alloys have a low density, high specific strength and stiffness, can significantly damp vibrations, serve as electromagnetic shielding and are biocompatible. Therefore, they have a wide range of applications, especially in transportation, consumer electronics, aerospace, military and medicine [62–66]. Magnesium alloys are mainly produced by casting. The crystalline structure of magnesium (closed hexagonal structure) shows low formation of slidding systems and low plastic deformation at room temperature. However, the solid and liquid phase regions of Mg-Al and Mg-Zn alloys are wide, so they are prone to precipitation of segregated elements in the Mg matrix, resulting in poor microstructural uniformity. The manufactured parts must be optimized by subsequent hot forming (extrusion, forging, rolling) or heat treatment. Another disadvantage of the conventional manufacturing process is its high cost and the long cycle that must be adhered to when forming complex parts. This limits the development and use of improved magnesium alloys [67–71]. Therefore, advanced production methods such as PBF-LB are used [72–74].

Processing of magnesium alloys with PBF-LB results in less formation of defects such as elemental segregation, porosity and deposition of impurities. The PBF-LB production process, in which the powder material is melted layer by layer, leads to a remelting of the previous layers so that a homogenization of the defects takes place. In addition, the melt pool solidifies very quickly, which contributes to the development of fine grains. This situation contributes to a high mechanical performance. However, the properties of the material, such as the rapid oxidation and vaporization of magnesium, make it difficult to process magnesium alloys. Currently, the following problems are particularly associated with the processing of magnesium alloys:

- Rapid formation of oxide layers due to the affinity of magnesium for oxygen during the PBF-LB process (Fig. 2-17). The oxide layers reduce the melting rate of the powder and lead to the formation of metallurgical defects [75].
- Magnesium has a narrow temperature range (450°C) between boiling point (650°C) and vaporization point (1107°C). Therefore, magnesium evaporates more easily than other alloying elements (Al, Ni, Ti) during the PBF-LB process [76]. This situation leads to imperfections such as porosity, rough surface and inaccurate dimensions.

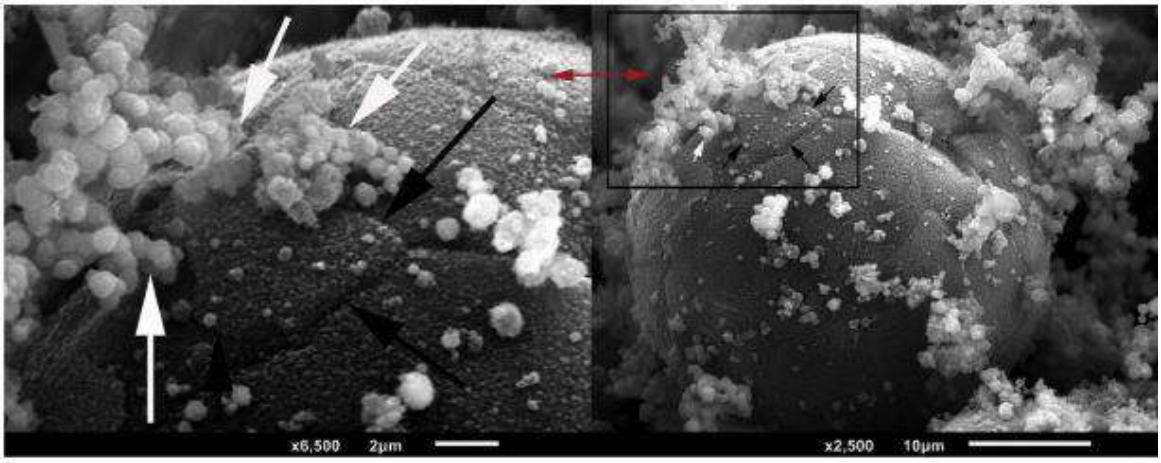

Fig. 2-17 Narušení oxidové vrstvy (černá šipka) na hranici zrn částice Mg a tvorba shluků oxidů (bílé šipky) [75]

The possible solution can be found on the basis of the other manufacturing processes:

- Oxidation can be reduced by forming magnesium alloys that reduce oxidation with alloying elements. In addition, oxidation can be reduced by setting the process parameters to a suitable energy that melts the powder particles but does not cause magnesium vaporization.
- Evaporation can be significantly reduced by alloying elements that adjust the boiling point and melting point of the magnesium alloy.

PBF-LB processing of magnesium alloys opens up new possibilities. Magnesium is an essential element found in human bones [77–79]. The presence of magnesium in bone leads to stimulation of new bone tissue growth [80, 81]. The combination of these factors with a modulus of elasticity close to that of bone tissue (Tab. 2-1) can lead to the avoidance or delay of reoperation [77]. Magnesium implants have already been tested on animals. In particular, the magnesium implant nourished the bone tissue for 12-18 weeks and helped to maintain its mechanical integrity before it was replaced by new bone tissue [82]. Moreover, WE43 is characterized by its corrosion resistance, making it a suitable candidate for biomedical applications [83].

Tab. 2-1 Mechanical properties of materials used for implants [77, 83]

	Bone	**Mg alloys**	**Ti alloys**	**Stainless steel alloys**
Elastic modulus (GPa)	3-20	41-45	110-117	189-205

The main advantage of PBF-LB processing of magnesium alloys is the ability to produce complex shapes. In particular, porous structures can be produced to achieve mechanical properties even closer to bone tissue. Structured bone implants can also contribute to the regeneration of bone tissue and its ingrowth through the implant [84]. Therefore, the fabrication of magnesium alloy structures can contribute to the utilization of magnesium alloys. In addition to biomedical use, magnesium structures can also be used in many other areas where weight reduction is required.

Process parameters

Ng et al. [85] succeeded in melting single welds from a magnesium alloy using a small PBF-LB system in an argon atmosphere, thus demonstrating the potential of PBF-LB technology for processing magnesium alloys. In the literature, the authors have dealt with the interaction between laser source and Mg powder. The effects of laser power, laser speed and continuous and pulsed laser modes were investigated. Based on the experiment with single welds, the window of suitable process parameters for pure magnesium powder was determined [86, 87]. The influence of the process parameters on magnesium alloys (Mg-9% Al, AZ91D, ZK60 and WE43) was also described [88–92]. An example of a window describing the influence of process parameters on single welds can be found in Fig. 2-18.

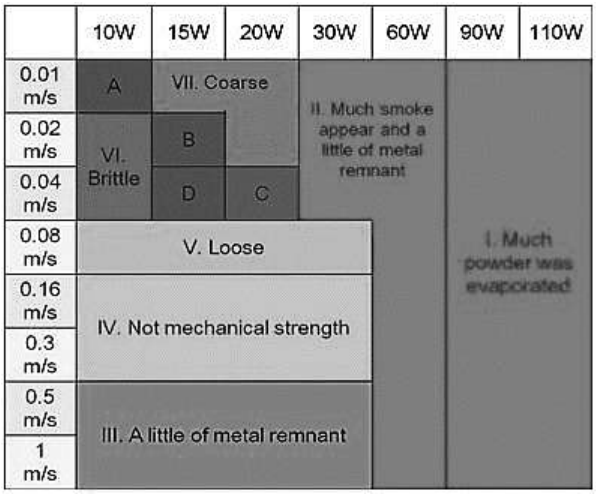

Fig. 2-18 Window of process parameters for processing of magnesium alloys Mg-Al [90]

The process parameter window is divided into sections depending on the laser power and the laser speed. In general, these two parameters can be described as linear energy (Equation 1). Based on the quality of the single welds, the four main regions can be defined as follows:

1. High input energy region: in this region, the energy of the laser is high. The magnesium vaporizes due to the low vaporization temperature (1107°C). The vapors expand rapidly and cause a strong recoil in the molten pool, blowing away both the molten material and the powder particles. Evaporation also leads to the formation of vapors, that reduce the energy of the laser. In addition, the vapors lead to the condensation of volatile substances on the laser glass [8]. The high temperature of the molten pool has an effect on the dynamic viscosity and leads to the instability of the molten pool. Magnesium molten pool has a much lower dynamic viscosity (1.5 Pa·s) than molten iron (6.93 Pa·s) and titanium alloys (2.2 Pa·s). The high temperature of the melt pool causes high thermal stresses that lead to a decrease in viscosity, which can also lead to imperfections in the material [13].
2. Low input energy region: In this region, the energy is not sufficient to melt magnesium powder (650°C), resulting in partially melted powder particles. Even if the powder particles fuse into the shape of the part, the final part is brittle and lacks mechanical strength. The process parameters in this area lead to delamination of layers, brittle fracture and high porosity [93]. At high laser speeds, a larger quantity of powder particles is blasted away due to the low density. The chemical activity of magnesium leads to oxidation, where MgO forms in a black cloud that contaminates the inert gas in the build chamber [89].
3. Region with suitable process parameters: It provides a good bond between the laser welds and results in good relative material density. Parts with a relative material density of 75-99.5% can be produced without obvious macro defects. In this range, the molten pool temperature is high while the viscosity of the molten pool decreases. The material can then be effectively dispersed, which increases the efficiency of the PBF-LB process [94, 95].
4. Region with “ball” effect: This effect is caused by a combination of low laser power, insufficient laser input energy and high layer thickness [96]. The “ball” effect is caused by the lack of wetting of the melt pool with the previous layer. The cohesion of the formed welds is impaired, which prevents the formation of further layers [97, 98]. The “ball” effect is a complex metallurgical process caused by the instability of the molten pool and by the Marangoni effect [9]. The occurrence of balls causes deterioration of the surface due to the combination of thermal stress and weak interlayer bonding.

The described areas in the process parameter window are typical for magnesium and magnesium alloys. However, the definition of the exact linear energy for each region depends on the parameters of the machine, the powder and the process parameters.

Loss of alloying elements

The melting of the powder particles by the high-energy laser leads to the loss (burning or vaporization) of Mg alloying elements during PBF-LB (Fig. 2-19a). The loss of Mg alloying elements has a negative effect on the stability of the melt and also changes the composition and microstructure [99]. This reduces corrosion resistance and significantly limits the production of high-quality components. The loss of alloying elements depends on the temperature and vapor pressure during the processing of Mg alloys, so that the loss of alloying elements occurs more easily at high temperature and high pressure. As shown in Fig. 2-19b, the vapor pressure of Al (2.9·10-14 Pa) at 400 °C is 13 orders of magnitude lower than that of Mg (3.6·10-1 Pa). At 713 °C and 886 °C, the vapor pressure of molten Mg is 1013 Pa. Increasing the melting temperature significantly increases the vapor pressure, which converts the molten pool into vapors.

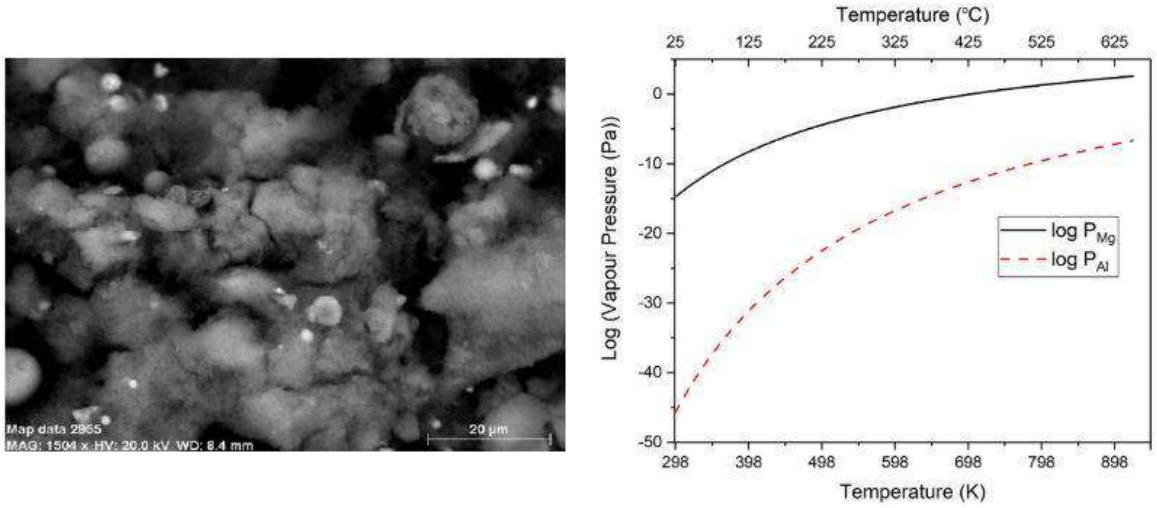

(a) **(b)**

Fig. 2-19 (a) SEM image of vapors of Mg alloy elements during the PBF-LB [76]; (b) vapor pressure of Mg and Al depending on the temperature [75]

In the PBF-LB process, the melting temperature of Mg is controlled by the laser energy. Wei et al. [91] found that the laser energy (over 214 J·mm3) led to strong vaporization of the Mg elements in the AZ91D alloy. The vaporized gas expanded rapidly and created a large recoil onto the molten pool, blasting away the surrounding unmelted powder particles. In addition, the high laser energies forced the melt pool to expand both longitudinally and transversely, causing the surrounding powder to be blown away. The rapid solidification reduces the volume of the melt pool and leads to large and deep pores, which roughen the surface considerably [76]. Wei et al. [100] processed the alloy ZK60 with PBF-LB. The alloy had a higher Mg:Zn ratio, but the total Mg and Zn content was lower, which was influenced by the shrinkage of the melt and the evaporation of alloying elements.

Microstructure

Melting the material with a high-energy laser requires sufficient heat dissipation to cool the parts. During the solidification of the material, the morphology of the melt pool and the metallurgical bond with the solidified material is established [101]. Suitable process parameters can lead to a fine microstructure with clear melt pool boundaries [102]. On the other hand, process parameters with high energy can lead to unrecognizable melt pool boundaries and a coarse microstructure [103, 104]. Unrecognizable boundaries and a coarse microstructure can reduce the mechanical performance of magnesium alloys [105].

3 ANALYSIS AND CONCLUSION OF LITERATURE REVIEW

The following section summarizes the state of the art in the production of lattice structures using PBF-LB. It describes two materials used in the study, namely an easily processable aluminum alloy and a magnesium alloy, with regard to their use for lattice structures. It also describes the influence of PBF-LB process parameters on the production of lattice structures. The main areas identified for further investigation are summarized in the subsection at the end of the section.

3.1 PBF-LB production of lattice structures

The lattice structures can be subdivided according to the topology of the unit cell. The body-centered cubic (BCC) topology is the least favorable due to the 35.26° inclination angle of the struts [19, 25], with the 45° inclination angle being considered the limit for PBF-LB production without support structures [26]. Due to the inclination, the BCC lattice structures are susceptible to the formation of imperfections such as porosity, rough surface and dimensional inaccuracy.

The formation of imperfections is influenced by the heat dissipation through the small-volume material of the lattice structures. In vertical struts, the heat is mainly dissipated by the material in the previous layers. Inclined struts lead to an accumulation of thermal energy in the downskin, where part of the energy is dissipated through the powder particles [27]. This situation leads to a different microstructure in the downskin and to the formation of imperfections [27, 29].

One of these imperfections is the porosity of the material. The pores reduce the load-bearing cross-section of the lattice structures and significantly impair their performance. The formation of pores in the material can be influenced by many PBF-LB parameters. The most important parameters are the laser power, the laser speed and the hatch distance. The combination of these parameters can lead to three situations depending on the energy of the process parameters [4, 30]: low energy, suitable energy and high energy. The low energy leads to a balling effect and irregular pores [31], that are dangerous and can lead to cracking [36–38]. The high energy causes overheating of the material, which leads to regular pores caused by the vaporization of alloying elements [30]. If the process parameters have enough energy to melt the material and the previously produced material is able to dissipate this energy at the same time, a relative material density of over 99% can be achieved [31–33].

The downskin of the inclined struts is partially built up directly on the powder particles due to the staircase effect typical of additive manufacturing technologies. Therefore, the heat accumulates in the downskin [27]. This leads to melting or partial melting of the surrounding powder particles that are bonded to the surface of the struts, which increases the surface roughness [37]. The surface roughness is influenced by an angle of inclination, whereby the lower the inclination, the higher the measured surface roughness [16, 38]. The energy of the process parameters also influences the surface roughness on the downskin [37]. A high energy leads to a higher flowability of the molten material, which can fill the gaps between the partially melted powder particles. The lower the energy, the lower the flowability of the material and the higher the surface roughness.

The molten powder particles on the downskin surface influence the weight and shape of the lattice structures [39–42]. The lattice structures are used in many cases to reduce weight; therefore, the weight is crucial to achieve this goal. The shape of the cross-section of inclined struts changes from circular to elliptical, which influences the mechanical performance of lattice structures. The energy of the process parameters also leads to changes in the strut diameters. The production of the desired strut diameter requires the determination of the combination of process parameters [30].

The imperfections can be reduced by a laser strategy that defines a hatching pattern for the cross-sections of the PBF-LB part in each layer. Usually, the hatch strategy (meander strategy) is used [6]. The hatch strategy consists of a contour trajectory and parallel trajectories which hatch the inner region, which rotates 67° in each layer. This strategy is susceptible to pore formation in the subsurface [43, 44]. Subsurface formation of pores can be reduced by skywriting, where the laser trajectories are extended beyond the cross section. Therefore, the acceleration of the laser velocity takes place outside the cross-section. In the cross-section, the laser speed is constant, which reduces the formation of pores at the beginning and end of the laser trajectories [45].

The geometry of lattice structures is suitable for production using the contour strategy. The contour strategy uses concentric laser trajectories to hatch the cross-sections. The pores are mainly formed between the laser trajectories [6, 16].

The imperfections affect the mechanical performance of lattice structures. To define the mechanical performance of lattice structures [46], the cell topology, the mechanical properties of the parent material and the relative density of the structure, which is defined as a percentage of the material volume in the unit cell, must be taken into account [47, 48]. The BCC lattice structures have a bending-dominated deformation mechanism according to Maxwell’s criterion [50], which is less effective than the stretching-dominated deformation mechanism [51].

The mechanical properties are also influenced by the material volume of lattice structures. Mechanical properties such as the modulus of elasticity, ultimate tensile strength, yield strength and elongation decrease with decreasing strut diameter [29] and decreasing strut inclination angle [52]. A reduction in the strut diameter from 5 to 1 mm led to a decrease in the modulus of elasticity of around 30%. The inclination from 90° to 35° led to a decrease in the modulus of elasticity of about 12%. The determination of the mechanical properties of lattice structures therefore requires different approaches. One of the possibilities is the use of modified tensile specimens consisting of several struts with nominal strut diameters [54]. The mechanical properties measured on these specimens led to a better correlation between the experimental and simulated compression testing of lattice structures [54]. Simulation can be used to determine Young's modulus of the material, which accounts for the performance of the material regardless of the cell topology or strut diameter [55].

3.2 PBF-LB processing of aluminum alloys

Processing of aluminum alloys is handled very well. They are used in many applications due to their good processability and their weight-to-load ratio [56–59]. The window of sufficient process parameters to produce parts with high relative material density, low surface roughness and high dimensional accuracy is relatively large [5]. This makes the aluminum alloy suitable for research in the field of lattice structures produced with PBF-LB.

3.3 PBF-LB processing of magnesium alloys

Magnesium alloys have a low density and high specific strength and stiffness, which makes them suitable for many applications [62, 64–66, 106]. One of the possible applications is bone implants. Magnesium alloys have mechanical properties close to those of human bone [80, 81], and magnesium stimulates the growth of new bone tissue [78, 79], which can avoid reoperations [77]. These properties make them interesting for further development.

Magnesium alloys can be processed using PBF-LB technology [72–74], but they are susceptible to the formation of imperfections. Magnesium alloys have a high affinity for oxygen; therefore, oxygen layers form during the PBF-LB process. The oxide layers reduce the melting rate of the powder and lead to the formation of metallurgical defects [75]. In addition, the narrow temperature range of 450°C makes magnesium alloys more susceptible to the vaporization of alloying elements [76].

PBF-LB processing of magnesium alloys can be divided into four areas depending on the energy input [88–92]. A high energy input leads to the vaporization of alloying elements and fumes influence the energy input. In addition, the fumes condense on the laser glass [8]. This led to the formation of imperfections [13, 76, 91, 99, 100]. High energy input also resulted in undetectable melt pool boundaries and coarse microstructure [103, 104], which can affect mechanical performance [105]. Low input energy led to delamination of the layers, brittle fracture and high material porosity [93]. The region with the "ball" effect is characterized by melt pool instability [9] due to low laser power, insufficient input energy and high layer thickness [96–98]. The appropriate input energy resulted in a high quality of the material with a relative material density of over 99% and a fine microstructure [94, 95, 102].

3.4 Lack of knowledge

Based on the analysis of the literature, the perspective areas for further research are selected. The most important aspects of the missing knowledge are addressed in the following bullet points:

- The lattice structures are a perspective for weight reduction, optimization of mechanical performance or heat dissipation. Although the PBF-LB can process lattice structures, the quality is crucial for their further use. Literature describes the influence of process parameters, but a precise optimization focusing on the reduction of imperfections such as material porosity, surface roughness and dimensional inaccuracy is missing.
- The inclination and material volume of the samples are crucial for the quality of the lattice structures. A low inclination angle leads to a higher occurrence of imperfections, as does a low material volume. However, the influence of the contour strategy on the quality of inclined struts with different volumes is not described.
- The production of lattice structures depends not only on the appropriate choice of LBF-PB process parameters, but also on the laser strategy. The contour strategy seems to be suitable for circular or elliptical cross-sections of lattice structures. However, the influence of the contour strategy on the quality and mechanical performance of lattice structures is not described.
- Lattice structures consist of struts and nodes, which are defined by the connection of the struts. The nodes have a different cross-section than the struts. In addition, the material in the nodes has a larger volume, which leads to a different heat dissipation. However, the influence of the contour strategy on the quality of the nodes is not investigated.

- The connection between the PBF-LB production of lattice structures and magnesium alloys makes them interesting for many applications. The weight reduction of lattice structures and the low density of magnesium alloys can lead to a significant weight reduction and more. However, the LBF-PB production of lattice structures from magnesium alloys has not yet been sufficiently explored.

4 AIM OF THE THESIS

The dissertation aims to LBF-PB production of lattice structures from lightweight materials. The dissertation focuses on improving the main imperfections, namely material porosity, production accuracy and rough surface. Imperfections affect the mechanical performance of the lattice structure; therefore, the mechanical performance should be discussed in relation to the quality of production. To achieve the main objective of this thesis, the following steps must be taken:

- Identify important process parameters for the production of lattice structures.
- Identify and perform the experimental procedures required to produce vertical and inclined struts as part of a lattice structure using an aluminum alloy and contour strategy.
- Identify and perform the experimental procedures required to produce cells forming a lattice structure using a magnesium alloy and contouring strategy.
- Identify and perform experimental procedures required to produce and determine the mechanical performance of magnesium alloy lattice structures.

4.1 Scientific questions

The analysis and review of the literature led to the identification of the following scientific questions.

Q1 Does the contour strategy lead to a reduction of imperfections such as material porosity, dimensional inaccuracy and rough surface that occur during PBF-LB production of lattice structures compared to the commonly used process parameters?

Q2 Does the contour strategy result in a relative material density of over 99.5% for lattice structures when using the magnesium alloy WE43?

Q3 Does the contour strategy improve the mechanical performance of the lattice structures compared to the hatch strategy for WE43 magnesium alloy?

4.2 Hypothesis

Each scientific question was tested against a working hypothesis formulated on the basis of the literature review.

Working hypothesis 1

Lattice structures can be considered as low volume geometries that require different PBF-LB process parameters than volume geometries to obtain high quality parts. A small volume of material is not able to dissipate the thermal energy fast enough during PBF-LB processing [27] which leads to the formation of imperfections [27, 29]. The effect is intensified with decreasing diameter of the struts and angle of inclination [29, 38, 52]. The main imperfections encountered in PBF-LB production of lattice structures are material porosity, rough surfaces and dimensional inaccuracies [16, 30, 31, 37–42]. The imperfections can be reduced with appropriate process parameters and a suitable laser strategy [30–33, 37]. Due to the geometry of lattice structures, the contour strategy appears to be suitable for their production [6, 16]. The contour strategy consists of circumscribed laser trajectories. The pores are mainly created between the laser trajectories. This could be reduced by a precise adjustment of the hatch distance. In addition, only three main process parameters could be used to control the energy input, namely the laser power, the laser speed and the hatch distance.

Working hypothesis 2

PBF-LB processing of magnesium alloys is more difficult than processing aluminum alloys [72–75]. Magnesium alloys have a narrow range of 450° between the melting point and the boiling point [76]. Therefore, precise selection of process parameters is required for PBF-LB production of parts with minimum imperfections [88–92]. Otherwise, the low energy can lead to delamination of the layers, brittle fracture and high material porosity [9, 93, 96–98]. High energy can lead to vaporization of alloying elements and coarse microstructure, resulting in low mechanical performance [8, 13, 76, 91, 99, 100]. Appropriate energy can lead to the PBF-LB production of parts with a relative material density of over 99% [94, 95, 102]. Considering the small volume of lattice structures [27, 29], the production of magnesium alloy lattice structures is more challenging. Therefore, the use of a contour strategy suitable for lattice structures [6] could be crucial and lead to the production of lattice structures with a relative material density above 99.5%.

Working hypothesis 3

The contour strategy can potentially reduce imperfections in lattice structures [6, 16]. The imperfections such as material porosity, rough surface, dimensional inaccuracy and coarse microstructure can lead to a reduction in mechanical performance [29, 38, 42, 52, 105]. This is caused by the reduction of the load-bearing diameter of the lattice structure due to material porosity [34, 35]. A rough surface can lead to the formation of cracks, especially under cyclic loading [38]. Dimensional inaccuracy affects the amount of material involved in load transfer [30, 42]. The performance of the lattice structure also depends on the cell topology and the relative density of the structure [46–48]. The influence of the PBF-LB process parameters on the performance of the lattice structure can be described by the Young's modulus, which describes the quality of the material [55].

4.3 Thesis layout

The dissertation consists of three scientific papers published in peer-reviewed journals with an impact factor. Each paper answers a scientific question. The first paper [I.] addresses the question of how the contour strategy affects the imperfection caused by PBF-LB production of lattice structures. To test the hypothesis, the lattice structure was simplified on the struts on which the influence of the process parameters was tested. The influence of the contour strategy was compared with the process parameters normally used for the production of bulk material. The second paper [II.] is dedicated to answering the second question, whether the contour strategy leads to a relative material density of over 99.5% for lattice structures made of the magnesium alloy WE43. In the paper, the influence of the contour strategy on the production of BCCZ cells was investigated. The experiments were selected to identify the range of processing energy for high-density unit cell fabrication. The third paper [III.] focused on the third scientific question, how the contour strategy affects the mechanical performance of the lattice structures. To test the hypothesis, the hatch strategy and skywriting were used for comparison. A high relative material density was achieved and the BCC lattice structures were subjected to a quasi-static compression test. The results were also evaluated using simulation to obtain Young's modulus.

I. VRÁNA, R.; JAROŠ, J.; KOUTNÝ, D.; NOSEK, J.; ZIKMUND, T.; KAISER, J.; PALOUŠEK, D. Contour laser strategy and its benefits for lattice structure manufacturing by selective laser melting technology. *Journal of Manufacturing Processes*, 2022, vol. 74, no. 1, p. 640-657. ISSN: 1526-6125.

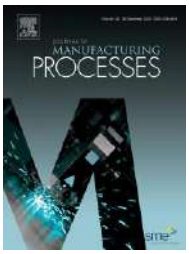

Journal impact factor = 6.1, Quartile Q1, CiteScore = 10.2
Author's contribution: 51%

II. JAROŠ, J.; VAVERKA, O.; SENCK, S.; KOUTNÝ, D. Influence of Process Energy on the Formation of Imperfections in Body-Centered Cubic Cells with Struts in the Vertical Orientation Produced by Laser Powder Bed Fusion from the Magnesium Alloy WE43. *Micromachines*, 2024, vol. 15, no. 2, p. 1-16. ISSN: 2072-666X.

micromachines
an Open Access Journal by MDPI

Journal impact factor = 3.0, Quartile Q2, CiteScore = 5.2
Author's contribution: 75%

III. JAROŠ, Jan; OŽVOLDÍK, Daniel; VAVERKA, Ondřej; NOPOVÁ, Klára; HURNÍK, Jakub. Influence of Laser Strategies on Performance of Lattice Structures from Magnesium Alloy WE43 Produced by Laser Beam Powder Bed Fusion. Online, *Advanced Engineering Materials*, 2025, ISSN 1438-1656.

Journal impact factor = 3.4, Quartile Q2, CiteScore = 5.7
Author's contribution: 55%

5 MATERIALS AND METHODS

Various experiments were conducted to test the hypotheses formulated from scientific questions. The experiments mainly focused on the quality improvement of lattice structures by setting process parameters. The experiments represent the structure of the dissertation, which consists of three research articles. The production of lattice structures was divided into three phases based on critical areas of the geometry (Fig. 5-1).

The first phase **(1)** focused on the geometry of the struts. The influence of the process parameters on the quality of the struts produced using the contour strategy was investigated. The quality was determined on the basis of the relative material density, pore distribution, surface roughness and dimensional accuracy. The results were compared with the hatch strategy, for which the process parameters were recommended by the powder manufacturer.

The second phase **(2)** involved the development of process parameters for the production of magnesium alloy cells. The relative material density, pore distribution, surface roughness and dimensional accuracy were taken into account when determining quality.

In the third phase of study **(3)**, the various laser strategies for the production of lattice structures were investigated. Based on the results of the second phase, the contour strategy led to production imperfections. Therefore, the complex analysis of five laser strategies was performed. Based on the relative material density, pore size, pore distribution, pore shape and microstructure, the most promising strategies were selected. The mechanical performance of these strategies was tested. Based on the results, the most suitable laser strategy for the production of magnesium alloy lattice structures was selected.

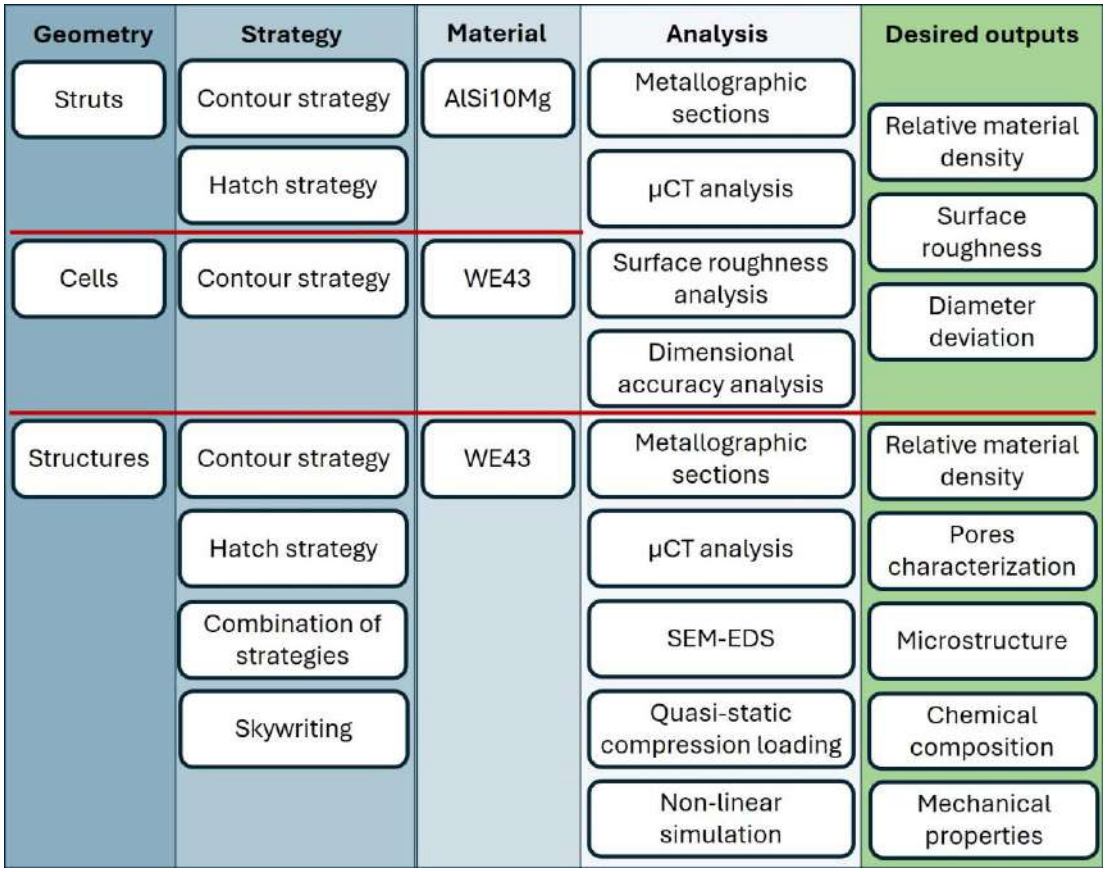

Fig. 5-1 Schema of thesis workflow

5.1 Laser beam powder bed fusion

5.1.1 Process parameters and powder material

All samples were produced using the SLM 280^{HL} machine (SLM Solutions Group AG, Lübeck, Germany). The machine is equipped with an ytterbium fiber laser with Gaussian distribution and a spot diameter of 82 µm. Two materials are used for production.

(1) The aluminum alloy AlSi10Mg (TLS Technik GmbH, Bitterfeld, Germany) was used. The powder was produced by gas atomization and the particle distribution was in the range of 15-60 µm. The platform was heated to 150°C and the layer thickness was 50 µm. A protective atmosphere of nitrogen gas was used. The oxygen content was kept below 0.2% during the production of the samples. A wide range of process parameters was used, i.e. a laser power of 175-400 W and a laser speed of 200-2000 mm/s.

(2), **(3)** The magnesium alloy WE43 was used (Luxfer MEL Technologies, Manchester, UK). The particle size distribution is in the range of 28-60 µm with an average particle size of 39.8 µm. The chemical composition is shown in Tab. 5-1. The temperature of the platform was 120°C and the layer thickness was 50 µm. A continuous supply of argon gas was used during the preparation of the samples. Therefore, the oxygen content was kept below 0.01%. The laser power was in the range of 50-250 W and the laser speed was in the range of 200-2000 mm/s.

Tab. 5-1 Chemical composition of WE43 powder

(wt %)	Mg	Y	Zr	Nd	Si	Cu
WE43 powder	Bal.	3.96	0.56	2.30	<0.01	<0.01

5.1.2 Laser strategies

Contour strategy

(1), **(2)**, **(3)** The contour strategy is a perspective for the production of cylindrical geometries. The laser trajectories have a circular shape and fit well into the geometry of lattice structures. The contour strategy is used in all three phases of the study. (Fig. 5-2a)

Hatch strategy

(1), **(3)** The hatch strategy is generally used for the production of parts in the PBF-LB process. Powder manufacturers usually have recommended process parameters for this strategy. In the first phase, the hatch strategy was used with the recommended process parameters to compare the effect of the contour strategy. In the third phase, the hatch strategy is used to investigate its effects on the production of entire lattice structures. (Fig. 5-2b)

Skywriting

(3) The influence of skywriting was analyzed. Skywriting refers to the optical system of the laser. The laser trajectories are extended behind the cross-section of the produced part. Therefore, the laser can use this extension for acceleration and deceleration. This ensures a constant speed in the cross-section of the sample. (Fig. 5-2c)

Combination of contour and hatch strategy

(3) The combination of the two strategies was also investigated. The contour strategy seems to be promising for the struts and hatch strategy for the node.

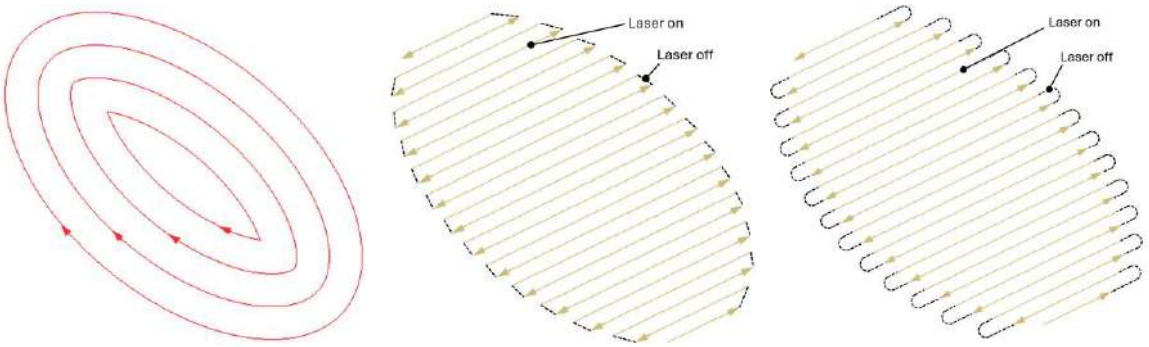

(a) **(b)** **(c)**

Fig. 5-2 Laser trajectories with direction of laser for: (a) contour strategy, (b) hatch strategy, (c) hatch strategy with skywriting

5.1.3 Samples

The aim of this work is to produce lattice structures with minimum imperfections. To achieve this goal, many samples were produced and analyzed. The process parameters for the production of lattice structures had to be determined. In the first phase, the geometry of the struts was used. The second phase focused on the unit cell. In the third phase, the geometry of the entire lattice structures was used.

Single weld tracks

(1), **(2)** The perspective window of the process parameters was defined based on the geometry of the single weld tracks. The continuity of the weld tracks was analyzed using images taken with an optical microscope. In the first phase of the study, the geometry of the weld tracks was also analyzed. For this purpose, the samples were ground and polished. The digital light microscope to record the images.

Thin walls

(1), **(2)** For the thin walls, the influence of the superposition of the welds was analyzed. The thickness of the walls was analyzed using the metallographic sections. The samples were ground and polished. The images were taken with a digital light microscope.

Hollow struts

(1), **(2)** The geometry of the hollow struts was chosen so that the welds were not only stacked on top of each other, but also had a rounded geometry. The diameter of the hollow struts ranged from 0.3 to 3 mm in the first phase and from 0.5 to 3 mm in the second phase. The vertical and inclined specimens were produced with an inclination of 35.26°, which corresponds to the BCC lattice structure. The specimens were metallographically ground and polished to the center of the struts. The images were taken with a digital light microscope. The thickness of the hollow struts was used to adjust the hatch distance to minimize the creation of lack of fusion pores.

Hollow struts consisted of two laser tracks

(1), **(3)** The samples were ground to the center of the struts and polished. The diameter in the first phase was 0.8, 1.2, 1.6 and 2 mm. The diameter for the second phase ranged from 0.5 to 3 mm with an increment of 0.5 mm. The digital light microscope was used to capture an images. The images were used to display the volume of porosity between two single welds. The porosity indicates if the overlap is appropriate.

Vertical and inclined struts

Vertical and inclined struts are part of the lattice structures. The geometry of the body-centered cubic cell (BCC) is used in the study. This geometry represents the most unfavorable inclination of 35.26° for production. Therefore, the effect of the process parameters can be described in the most unfavorable case.

(1) The struts were analyzed by µCT. The diameter of the struts ranged from 0.6 to 3 mm. The relative material density, pore size, pore shape and pore distribution were determined.

(2) In the second phase, the samples were prepared metallographically. The diameter of the struts was 0.5, 1, 2 and 3 mm. The digital light microscope was used to take an image of the samples. The relative material density was measured.

Body centered cubic cells with vertical struts

(2) The geometry of the whole unit cell was used to determine the influence of the process parameters on the node (center of the cell). The body-centered cubic cells with vertical struts (BCCZ) consist of vertical and inclined struts. The diameters of the struts were 0.5, 1, 2 and 3 mm. The cells were analyzed by µCT. The influence of the process parameters on the formation of pores in the connection between the struts was investigated.

BCC cells

(3) The geometry of BCC cells was used. The diameter of the struts was 1.5 mm. The metallographic sections were used to analyze the relative material density to obtain suitable process parameters. The µCT analysis was used to determine the distribution of pores, the number of pores, the size of pores, the shape of pores and the relative material density.

BCC lattice structures

(3) 3×3×3 BCC lattice structures with a diameter of 1.5 mm were used to show the influence of process parameters on mechanical performance. The lattice structures were loaded by quasi-static tests. The results were also used to determine the Young's modulus using finite element analysis (FEA).

5.2 Experiments

5.2.1 Single weld tracks continuity

(1), **(2)** The continuity of single welds was one of the parameters used to select suitable process parameters for PBF-LB production. The images of the samples were taken using the optical microscope (Olympus SZX7, Olympus, Tokyo, Japan). Each single weld was visually inspected.

5.2.2 Metallographic sections

The metallographic sections were used for many samples. Although they were taken in a section plane of the samples, the analysis was precise due to the image resolution. The specimens were ground and polished. In the case of strut or cell samples, the section plane was in the center. The digital light microscope (Keyence VHX-6000, objective Z250R, zoom 250×, Keyence, Mechelen, Belgium) was used to take the images.

(1) The dimensions of the welds were measured with the digital light microscope, i.e. weld width, weld height and weld depth. These dimensions were used to select the appropriate process parameters. In the case of thin walls and hollow struts, the thickness was also measured using the digital light microscope.

(1), **(2)** The metallographic cross sections were used to analyze the relative material density for the hollow strut samples consisting of two laser tracks, struts and cells. The images were captured using the digital light microscope and converted into binary images using the threshold method and the Otsu method [107]. The white color represented the material and the black color represented the pores. The percentage of white color determined the relative material density.

5.2.3 µCT analysis

(1) Micro-computed tomography (µCT) analysis was used to determine the distribution of pores throughout the volume of the sample. In the first phase of the study, the µCT device (GE phoenix v | tome | x L240, Waygate technologies, Hürth, Germany) was used with a microfocus X-ray tube with a voltage of 130 kV, a current of 100 µA and a 0.5 mm wide copper filter. The voxel resolution was 16 µm for all samples with a minimum pore volume of 2 voxels. The data was reconstructed using Datos reconstruction software and processed in VGStudio Max 3.1 software. The threshold value was automatically determined based on the scan of all samples. The relative material density and pore distribution were determined. The polygonized scans were also used for dimensional accuracy and surface roughness analysis.

(2) Nanofocus X-ray computed tomography (nanoCT, GE phoenix|x-ray Nanotom 180 NF, Waygate technologies, Hürth, Germany) was used to analyze the pores in BCCZ cells. The following setting was used: an X-ray tube voltage of 130 kV, a current of 80 µA, an integration time of 600, an average of 5 images, a total of 1500 projections and a 0.1 mm copper filter to reduce artifacts due to beam hardening. The data were processed in VGStudio Max 2023.1 using an ISO50 threshold and a minimum of eight voxels for a segmented pore [111]. The data were processed so that only the material of the BCCZ cells was included in the analysis. The relative material density and pore distribution in the BCCZ cells were determined.

(3) The µCT device (GE Phoenix V Tome X L240, GE Sensing and Inspection Technologies GmbH; Wunstorf, Germany) with a voxel resolution of 10 µm was used. A total of 2000 projections were performed. The 180 kV/15W nano-focus X-ray tube with a voltage of 110 kV, a current of 240 µA, an integration time of 334 ms, an average of 3 images per projection and a 0.2 mm copper filter were used. The data was processed in VGStudio Max 2023.4.1. The bound powder particles on the samples were not included in the analysis. The µCT analysis was used for BCC cells. The parameters evaluated were relative material density, pore distribution, pore shape and pore volume.

5.2.4 Surface roughness

(1) The surface roughness was measured on the downskin of the inclined struts, where the downskin area is most vulnerable to the influence of the PBF-LB high-energy process. In the first phase, the high-resolution polygonized data from the µCT analysis was used. The data was processed in the GOM Inspect software by comparing CAD data and polygonized data. The surface roughness Ra was calculated from the deviation.

(2) The digital microscope (Keyence VHX-6000, objective Z250R, zoom 250×, Keyence, Mechelen, Belgium) was used to analyze the surface roughness Ra. The surface roughness was measured on the downskin area of the struts in the 5 lines. The final value was determined as an average value.

5.2.5 Dimensional accuracy

(1) The GOM Inspect software was used to determine the dimensional accuracy of the struts. In the first phase, the polygonized samples from the μCT analysis were used. The Gaussian cylinder with an accuracy of 3 sigma was fitted to the data. The Gaussian cylinder was used to obtain the actual dimension of the struts.

(2), **(3)** The optical 3D scanner (Atos Triple Scan III, GOM GmbH, Braunschweig, Germany) was used to obtain the real surface of the struts. The maximum inscribed and minimum circumscribed cylinders were fitted to the polygonized data to obtain the bearing diameter of the struts and the diameter affected by the bonded powder particles on the surface of the struts.

5.2.6 Melt pool morphology and microstructure

(3) The morphology of the melt pool and the microstructure have an influence on the mechanical properties. Therefore, the cross-sections of BCC cells produced from the magnesium alloy WE43 were analyzed. The images were taken with an light microscope (Olympus GX51, Olympus, Tokyo, Japan).

(3) The microstructure and chemical composition of the samples were analyzed using a scanning electron microscope (SEM). The scanning electron microscope (Zeiss Ultra Plus, ZEISS, Oberkochen, Germany) was equipped with an energy dispersive X-ray spectrometer EDS (X-Max 20, Oxford Instruments, Abingdon, Oxfordshire, United Kingdom). An acceleration voltage of 10 kV was used.

5.2.7 Quasi-static compression testing

(3) The 3×3×3 BCC lattice structures were loaded under compression to determine the mechanical performance of the structures fabricated using different laser strategies. A universal testing machine (Shimadzu AGX-V 100kN, Shimadzu Corporation, Kyoto, Japan) equipped with a mechanical extensometer attached to the compression plates was used. The test speed was 1 mm/min and the sampling rate was 100 Hz. The deformation behavior was observed with a digital 3D image correlation system (DIC) from Dantec Dynamic (Dantec Dynamics a/s, Skovlunde, Denmark). The DIC was equipped with two 5 Mpx cameras with 50 mm objectives. A stereo base of approximately 150-175 mm and an angle of 20-25° was used. The facet size and grid spacing were set to 25 Px and 13 px, respectively. The rate of image acquisition was 1 Hz.

5.2.8 Simulation

(3) Finite element analysis was used to determine the Young's modulus of the material. The quarter geometry of 3×3×3 BCC lattice structures was used. To represent the real dimensions of the structures, the maximum inscribed diameter of the struts was used. This diameter represents the load-bearing diameter of the struts. The structure was placed between two 0.5 mm thick plates. The lower plate was fixed and a displacement of -2 mm was applied to the upper plate. A friction coefficient of 0.45 was applied between the plates and the specimens [113]. An element size of 0.6 mm was used. The material of the plates was stainless steel, which has a Young's modulus 50,000 times higher than the WE43 magnesium alloy. The magnesium alloy was defined based on the powder manufacturer's data, i.e. Poisson's ratio of 0.27, Yield strength of 220 MPa, Young's modulus of 45 GPa and tangent modulus of 920 MPa. The variable parameter was the Young's modulus which was changed in steps of 5 GPa until the deviation between the effective elastic modulus from the mechanical tests and the simulation was less than 5%. The final Young's modulus represented the material of the tested lattice structure.

6 RESULTS AND DISCUSSION

The following section summarizes the most important results, particularly in the field of the production of lattice structures from lightweight materials. The first part is divided into three subsections representing the research included in the study. The subsections focus on three topics, namely the production of struts using the aluminum alloy contour strategy, the production of BCCZ cells using the magnesium alloy contour strategy, and the production of magnesium alloy lattice structures using various laser strategies. Each subsection is dedicated to testing one of the above scientific hypotheses. The second part consists of a complete version of the research papers in which the results are discussed in detail.

6.1 Research paper I

The most important results of the *Research paper I* related to the influence of the contour strategy on the production of vertical and inclined struts. A new approach for the definition of the process parameters was presented, in which the geometry close to the lattice structure was used to adjust the process parameters. The production sequence of the contour strategy trajectories was also taken into account. The promising process parameters were determined based on the quality of the struts, taking into account the relative material density, surface roughness and dimensional accuracy.

The window of process parameters laser power and laser speed for the aluminum alloy AlSi10Mg was determined based on the quality of single welds, excluding non-continuous and high energy influenced combinations [5, 60, 61]. The promising window was as follows: Laser power 200-350 W, laser speed 500-1400 mm/s, corresponding to a linear energy of 0.25-0.4 J/mm.

The track width was determined from single welds, thin walls and hollow struts. The thickness of the thin walls and hollow struts increased by 28% and 34%, respectively, compared to the width of the single weld. The influence of the stacked laser trajectories thus had a significant effect, as did the influence of the geometry.

The hatch distance was determined using the value of the overlap. The overlap represents the percentage value of the track thickness that is overlapped by the neighboring laser track in the contour strategy. To determine the appropriate value of overlap, the relative material density between two laser tracks was measured using hollow struts consisting of two laser tracks. An overlap of 35% was considered sufficient.

The determined window for the laser power and laser speed as well as the overlap of 35% were used for the production of vertical and inclined struts. The overlap was determined using the equation from the response surface analysis of the thickness measured on the hollow struts. Different values were determined for vertical and inclined struts. This may be related to the different heat dissipation for both orientations [27]. The influence of the process parameters was determined using the relative material density from the µCT analysis. The order in which the laser trajectories were produced in the contour strategy had an effect on the formation of material porosity. The out-in direction led to the formation of irregular pores in the center of the struts. This was caused by the drag of the surrounding powder into the melt pool during the PBF-LB process [108]. The in-out direction reduced this effect. The fabricated struts resulted in a relative material density of over 99.9% for the vertical struts and 99.65% for the inclined struts.

Even though the relative material density was good, some struts showed pore formation in the center of the struts. This led to the assumption that the overlap at the center of the struts was not set to the appropriate value of 35%. Therefore, the equations from the response surface analysis for the thickness of the hollow struts were used to determine optimal combinations of process parameters with a constant overlap of 35% between all laser trajectories in the contour strategy. The produced struts achieved a relative material density of over 99.8% for all selected combinations of process parameters. The results were even more significant compared to the commonly used process parameters for AlSi10Mg, where the relative material density of the samples reached 98% in some cases. The specific selection of process parameters for strut diameter and inclination led to an improvement compared to a set of process parameters used in the studies by Dong et al. [29, 52].

The dimensional accuracy was compensated with the beam compensation parameter. The appropriate value of 34% of the thickness of hollow struts was found to be optimal. The dimensional deviation for the vertical struts was improved from the median value of -0.11 mm to 0.3 mm. For the inclined struts from -0.10 mm to 0.04 mm. The inclined struts still had an elliptical shape as there was more material in the downskin region [27, 42].

The process parameters also had a significant influence on the surface roughness Ra of the struts. The surface roughness Ra increased with the energy of the process parameters. As the strut diameter increased, the surface roughness Ra decreased. The vertical struts reached a maximum Ra of 16 µm and the inclined struts a maximum Ra of 80 µm, measured on the downskin of the inclined struts. The results are consistent with the study by Tian et al. [38], in which a smaller angle of inclination led to a higher surface roughness.

6.2 Research paper II

Research paper II focused on the PBF-LB quality production of BCCZ cells from the magnesium alloy WE43. Magnesium alloy is a special material that is difficult to process with PBF-LB technology [75, 76]. Therefore, the findings from the first research work were used for the production of BCCZ cells. The influence of the process parameters on the relative material density, surface roughness and dimensional accuracy was described.

A wide window of process parameters was used for all experiments, i.e. a laser power of 50-250 W and a laser speed of 200-1000 mm/s. The track width changed with the linear energy and the sample geometry. The single welds, thin walls and hollow struts showed the same linear increasing trend up to a linear energy of 0.4 J/mm. At a linear energy of more than 0.4 J/mm, the hollow struts lead to a higher track width, while single welds lead to a lower track width. In the case of the hollow struts, the increasing diameter led to a decreasing weld width.

For the overlap determination, the hollow struts were produced from two laser tracks. The highest relative material density was measured for the overlap between 45% and 80%, depending on the energy of the process parameters and the diameter of the struts. For vertical struts, it was also found that a lower energy of the process parameters required a higher overlap to achieve a high relative material density, which may be related to the heat dissipation during the fabrication of PBF-LB struts [27].

The relative material density 99.3-99.6% was achieved for vertical and inclined struts with diameters of 0.5-3 mm at an area energy between 1.15-3.69 J/mm^3. The area energy was determined from the laser power, the laser speed and the hatch distance. The production of the magnesium alloy WE43 using PBF-LB was more difficult when manufacturing struts low volume.

The process parameters for vertical and inclined struts, which achieved a relative material density of over 99.2%, were used for the production of BCCZ cells. BCCZ cells combine both vertical and inclined struts. The BCCZ cells with diameters of 0.5 mm and 1 mm achieved a relative material density of over 99.8%. Diameters of 2 mm and 3 mm achieved a relative material density of less than 99.7%, but open, irregular pores were present. Open pores could not be included in the µCT analysis, therefore the quality of these BCCZ cells was insufficient. This may be related to the higher volume of the material, which has a different heat dissipation compared to the struts [27, 29, 52].

The surface roughness Ra measured on the side of the struts reached 30-64 µm for vertical struts and 42-64 µm for inclined struts. The energy of the process parameters influenced the surface roughness Ra. Higher energy resulted in higher surface roughness, which contradicts the results of Han et al. [37]. On the downskin of the inclined struts, the amount of bound powder particles was high, so the surface roughness was not measured there. This effect was probably caused by the high-energy PBF-LB process and the low melting point of the magnesium alloy [1, 2, 76]

To measure the amount of bonded powder particles on the surface of the struts, the maximum inscribed diameter and the minimum circumscribed diameter were used [42]. Depending on the orientation of the strut, the maximum inscribed diameter deviated from the nominal diameter by 4-44%. The minimum circumscribed diameter reached 3.5 times the nominal diameter. This situation occurred with high energy process parameters and a diameter of 0.5 mm. The diameter was mainly influenced by the bound powder particles on the downskin of the struts [30, 39–42, 76].

6.3 Research paper III

Research paper III dealt with the influence of laser strategies on the quality of BCC lattice structures produced from a WE43 magnesium alloy processed with PBF-LB. The results of the previous study showed that the contour strategy might not be suitable for the production of BCCZ cells from a magnesium alloy. Therefore, the hatch strategy was considered. The combination of laser strategies and skywriting was also considered. The results described the influence of the laser strategies on the relative material density, pore distribution, pore volume, pore shape, microstructure, chemical composition, mechanical performance and material properties of the BCC lattice structures.

The BCC cells were fabricated using the contour strategy and the hatch strategy to determine sufficient process parameters based on metallographic cross-sections. For each laser strategy, a set of process parameters was selected based on relative material density (above 98.97%).

Selected process parameters were used for the fabrication of BCC cells for µCT analysis of relative material density, i.e., contour strategy, hatch strategy, combination of contour and hatch strategy, hatch strategy with skywriting, and combination of contour and hatch strategy with skywriting. The contour strategy achieved a relative material density of 99.13% with pores between the laser trajectories in the struts and more pores in the node. The results were in agreement with those of Pauly et al. [6]. The Hatch strategy achieved a relative material density of 98.87% with pores near the surface of the cell [43, 44]. The number of pores in the node was reduced. The combination of the botch strategies resulted in a relative material density of 99.11% using the contour strategy for the struts and the hatch strategy for the node. Skywriting for the combination of both strategies had no positive effect. On the other hand, skywriting for the hatch strategy led to a reduction in subsurface pores and achieved a relative material density of 99.55%. Skywriting resulted in a constant laser speed through the cross-section, which was crucial for the reduction of subsurface pores [45].

In addition, the hatch strategy with skywriting had a low number of dangerous pores defined for compactness in the range of 0-0.5 and sphericity of 0-0.55 [36]. The melt pools had visible boundaries typical of PBF-LB technology [101, 102]. The microstructure showed very fine areas rich in rare earths, which were not observed with the contour strategy. Due to the high energy of the process parameters, the contour strategy showed no visible boundaries of the melt pools that could affect the mechanical performance [103–105].

The mechanical performance of BCC lattice structures fabricated using the contour strategy, the hatch strategy with skywriting, and the combination of both strategies was quasi-statically tested. The effective elastic modulus of structures ranged between 130-152 MPa. However, the mechanical performance was affected by the actual diameters of the struts [29]. The contour strategy and the combination of both strategies had a strut diameter of 1.96 mm (nominally 1.5 mm). The hatch strategy with skywriting achieved a diameter of 1.65 mm. The measured diameter was the maximum inscribed diameter, which is the bearing diameter of the struts [42].

Therefore, simulation was used to determine the Young's modulus of the material [55]. Typically, the Young's modulus of material in the lattice structure is lower than that of bulk material [29, 52]. The hatch strategy with skywriting achieved Young's modulus of 40 GPa (the nominal value for the magnesium alloy WE43 is 44-45 GPa [109, 110]). The contour strategy achieved Young's modulus of 15 GPa and the combination of both strategies achieved 20 GPa.

6.4 Original research papers

Journal of Manufacturing Processes 74 (2022) 640–657

Contents lists available at ScienceDirect

Journal of Manufacturing Processes

journal homepage: www.elsevier.com/locate/manpro

Contour laser strategy and its benefits for lattice structure manufacturing by selective laser melting technology

Radek Vrána [a,*], Jan Jaroš [a], Daniel Koutný [a], Jakub Nosek [a], Tomáš Zikmund [b], Jozef Kaiser [b], David Paloušek [a]

[a] Brno University of Technology, Faculty of Mechanical Engineering, Institute of Machine and Industrial Design, Technická 2896/2, 616 69 Brno, Czech Republic
[b] CEITEC - Central European Institute of Technology, Brno University of Technology, Purkyňova 123, 61200 Brno, Czech Republic

ARTICLE INFO

Keywords:
Laser powder bed fusion (L-PBF)
Selective laser melting (SLM)
AlSi10Mg aluminium alloy
Contour laser strategy
Transient thermal simulation
Finite element method (FEM)
SLM process simulation, porosity
Surface roughness
Dimensional accuracy
Lattice structure

ABSTRACT

This paper deals with the research of the Selective Laser Melting (SLM) scanning strategy to produce lattice structures from AlSi10Mg powder material. Nowadays, most of the SLM end-users use the laser strategy and parameters recommended by powder or machine suppliers to produce different components. However, this setup can cause material and shape imperfection, especially in the case of low-volume lattice structures. In this study, the default meander scanning strategy for AlSi10Mg material was changed to contour strategy and its main SLM process parameters were developed. Commonly used experiments were modified to consider the lattice structure's shape and dimension. The results showed that by using developed parameters, i.e., recommended range of input linear energy of 0.25–0.4 J/mm; track width based on strut diameter, input linear energy and the orientation of strut; the overlap of the laser contour tracks of 35% and inside-out direction; it is possible to produce lattice structures with high material density (more than 99.8%) and low surface roughness in a wide range of strut diameters from 0.6 to 3 mm. The differences in lattice structure production of vertical and inclined struts are described and discussed in relation to the SLM process during powder melting with use of thermal transient simulation.

1. Introduction

Additive technologies have become increasingly used to manufacture unique parts, mainly due to the ability to produce components with complex shape from a wide range of materials. It allows us to be inspired by the shape diversity of nature during the product design phase and to produce components with very few limits compared to conventional production. One of these unique shapes is a lattice structure with the potential for application in the aerospace or space industry due to a great weight to load ratio [1–4].

Selective laser melting (SLM) is a part of laser powder bed fusion (L-PBF) technology which is an additive technology that produces the components layer-by-layer using a high-energy laser to melt the fine metal powder. This technology allows processing of a wide range of metal materials from aluminium alloys to high-strength titanium alloys; therefore, it is a promising technology for various advanced industries. The SLM process is controlled by many process parameters that directly influence the produced parts' quality and mechanical properties. The key parameters are those of the laser, i.e., laser power (LP), laser speed (LS), and the parameters of the scanning strategy, i.e., hatch distance (HD), overlap (OL), beam compensation (BC), and the type of used strategy (stripe, chessboard, contour etc.) [5–7]. The qualitative issues of the wrong setting of SLM process were examined mostly on the volumetric parts [8–10]. The results showed that the main imperfections arise not only on the surface of the parts (surface roughness, dimensional accuracy) but also inside of the material (porosity, unmelted areas, inappropriate material structure). In case of low-volume lattice structure, the same imperfections occur; however, they behave differently during SLM manufacturing process as was shown by Dong et al. [11]. They manufactured thin tensile samples with various diameters from 1 to 5 mm and examined the diameter's size effect on porosity and mechanical properties. The results showed that the porosity and mechanical properties were unstable for dimensions below 4 mm, i.e., the porosity increased, and mechanical properties decreased. It follows that

* Corresponding author.
E-mail addresses: Radek.Vrana@vut.cz (R. Vrána), Jan.Jaros2@vut.cz (J. Jaroš), Daniel.Koutny@vut.cz (D. Koutný), Jakub.Nosek2@vut.cz (J. Nosek), Tomas.Zikmund@vut.cz (T. Zikmund), Jozef.Kaiser@vut.cz (J. Kaiser), David.Palousek@vut.cz (D. Paloušek).

https://doi.org/10.1016/j.jmapro.2021.12.006
Received 10 October 2021; Received in revised form 28 November 2021; Accepted 7 December 2021
Available online 6 January 2022

for thin lattice structures, the default SLM process parameters led to worse results, and the parameters and laser strategy must be improved.

The results of the previous study could be closely associated with the lattice structure geometry usually composed of many thin inclined struts. The heat flow and dissipation of the thermal energy after laser melting are lower compared to full volumetric parts. It was shown by Delroisse et al. [12], who divided the inclined strut into the upper and bottom areas (above and below strut axis) due to the different quantity of an internal porosity observed by μCT. The upper area of the inclined strut contained a porosity of 0.1% compared to the bottom area with a porosity of 4%. The same situation was observed in the BCC cell node by Liu et al. [13].

This thermal behaviour also contributes to the increase of surface roughness, as was shown by other studies [14–16], which can result in a change in thin-struts shape, as was shown in studies [17–20]. Han et al. [14] described two possible explanations for high surface roughness in down-skin areas. First, the commonly known stair effect, which arises due to layer-by-layer production and orientation of strut. The second is the melt pool's flowability, which is in the liquid phase for a longer time due to the accumulation of thermal energy in the low-volume struts. Then, the melted material can flow deeper into the surrounding powder bed and the powder particles could be entrapped on the strut surface.

One way to reduce the consequences of the thermal accumulation is to reduce the input laser energy by modification of the SLM process parameters. However, it is also necessary to modify the SLM scanning strategy because they are strongly connected, as was described in many studies [10,15,21–27]. The authors [21,22] showed LP and LS's effect on the single-track width. As LP increased and LS decreased (i.e., the input laser energy increased), the single weld-track width increased. The authors [21,23] defined the key weld track parameters, i.e., depth and width of the track, which ensure the right connection between neighbouring tracks and previous layers as well as the height of the track, which must be close to the applied layer thickness. Tian et al. [15] measured the contact angle between single track's surface and base plate. A contact angle higher than 90° led to the formation of a balling effect, which could cause a higher porosity between neighbouring track welds due to unmelted powder particles. Other authors focused on the overlapping of the neighbouring tracks [10,25]. They found out that too low HD led to spherical porosity between weld tracks due to material overheating and following material evaporation. Due to the fast solidification of melted material, the vapours were trapped inside the material.

On the other hand, the large HD causes poor or no connection between the neighbouring single-tracks and trapping of the unmelted powder between them [28]. According to the melt pool behaviour, the composition of the powder is also related to the porosity between single tracks. Louvis et al. [26] described that the AlSi10Mg alloy formed an oxide film at the melt pool's edges. Oxide film limits the melt pool flowability and causes porosity due to nonmelted powder particles closed between the laser tracks.

The SLM process parameters setting's influence was also examined directly on the lattice structure geometry. Qiu et al. [27] dealt with the lattice structures with a diameter of 0.3 mm. Using a constant LS of 7000 mm/s and increasing LP (in the range of 150–400 W) the diameter of struts was increased in the range of 0.26–0.5 mm. By using a constant LP of 400 W and increasing LS (in the range of 1000–7000 mm/s), the struts' diameter was decreased in the range of 0.8 to 0.6 mm. It follows that the parameters setup directly influences the final dimensions of the lattice structure and thereby the mechanical properties. Vrana et al. [16] performed a complex study that described the influence of the main SLM process parameters (LS, LP, HD) directly on the lattice structure imperfections such as internal porosity and surface roughness. They also used special contour strategy to reach relative density of AlSi10Mg low-volume material of 99.83%. The results showed a clear dependence of porosity and surface roughness on the input energy. However, the study was performed only for the strut diameter of 2 mm, and the results for other sizes could differ, as was shown by Dong et al. [11]. The scanning strategy for lattice structure production was also dealt with Pauly et al. [7]. They used three different scanning strategies to produce a thin strut geometry - chessboard strategy (small pores; ρ_{rel} = 97.2%), stripe strategy (sharp pores; ρ_{rel} = 98.5%), contour strategy (small round pores; ρ_{rel} = 97.7%). The results showed that the strategy could significantly influence mechanical properties due to the shape of the pores and the porosity level.

Mechanical properties of low-volume lattice structures had higher susceptibility to material imperfections when the universal SLM process parameters were used [29,30]. These authors used recommended process parameters for lattice structures production and significant surface roughness and dimensional deviation (between −7.5% to −12.5%) were obtained. These deviations resulted in large differences in simulated mechanical properties using nominal dimensions of lattice structures and finally, the actually measured geometry had to be used to predict correct mechanical behaviour. The final results showed a strong correlation between computed and experimental mechanical properties. Kempen et al. [9] showed the influence of borderline porosity on mechanical properties. The porosity was generated by used scanning strategy and affected mechanical properties.

Based on the previous results, this study will focus on improving the lattice structure production using the contour laser strategy approach. The main goal is to find out a dependence of the main SLM process parameters on the lattice structure dimensions (dimensions up to 3 mm) and to reach stable and predictable lattice structure parameters such as porosity, surface roughness, and dimensions after SLM production.

2. Materials and methods

For better orientation in present study, a brief experiments workflow was created. The detailed description of the used materials and methods is further in the chapter.

To define the contour laser strategy (CS) parameters, the following workflow must be performed:

- Single weld tracks experiment - the perspective SLM process window was defined based on the visual and digital-light microscope results (Table 2).
- Thin wall/ hollow strut experiment - the single weld track sample was changed to 3D shapes of wall and hollow strut samples that includes the thermal conditions during lattice structure manufacturing. The larger dimensions were obtained compared to the single weld track experiment (Fig. 11).
- The key 3D dependence - diameter (d) vs. input linear energy (LE) vs. hollow strut thickness (HT) dependence was created that describe the change of the HT parameters and allows contour strategy parameters adjustment according to actual lattice structure geometry (diameter, orientation, Fig. 14).
- Overlap (OL) experiment - connection between two hollow strut walls was analysed. The optimum OL values were evaluated based on the porosity in the overlap area (Fig. 13).
- Porosity experiment (1st testing loop) - Based on the previous results, the contour strategy was designed. The porosity results showed imperfection (Table 5); therefore, the parameters were modified.
- Porosity experiment (2nd testing loop) - Significant improvement of porosity result was observed (Fig. 16); therefore, the dimensional and surface roughness analysis were performed.
- Porosity experiment (3rd testing loop) - The final fine tuning of a contour laser strategy was performed using d vs. LE vs. HT dependence. Various SLM parameter were defined as optimal for different strut diameter (Table 6).

2.1. Selective laser melting manufacturing

SLM machine (SLM 280^{HL}, Lübeck, Germany) equipped with a 400 W Ytterbium fibre laser has been used to manufacture all samples. The laser source had a Gaussian distribution and was focused on a spot diameter of 82 μm. The process conditions were constant for all produced batches of samples, i.e., the oxygen level was kept under 0.2% during the SLM process, the protective atmosphere of nitrogen was used, the platform was heated to 150 °C, the layer thickness of 50 μm was applied and the main SLM parameters were used based on the results of this study. All samples were produced from the gas atomised aluminium alloy AlSi10Mg (TLS Technik GmbH, Bitterfeld, Germany) with particle size distribution in the range of 15–60 μm (Fig. 1b).

2.2. The main contour laser strategy parameters

The basic SLM experiments described in the studies [13–15,21,23,24] were modified to consider the specific conditions during SLM manufacturing of low-volume lattice structures. The obtained parameters were used to define the parameters of the presented contour laser strategy shown in Fig. 1a, which are - laser power (LP), laser speed (LS), overlap (OL) and beam compensation (BC). Overlap (OL) defines sufficient connection between two laser tracks inside the strut and is determined by contour distance (CD). The exact value of OL can be found only for the known track width (HT). Beam compensation (BC) indicates the strut border's offset to achieve the required strut size.

2.2.1. Laser process parameters window

The single-track experiment aimed to describe the influence of the LP, LS laser parameters on the quality of the AlSi10Mg single track welds and thereby find a suitable process window include the consistent track welds with the known welds' width. Single track welds were produced on the top side of a 5 mm solid material block (Fig. 2b) and captured by a light microscope (Olympus SZX7, Olympus). The images were further used for track welds width measurement and visual evaluation of the single-track welds' continuity and uniformity. The track width (TW) was measured in twelve points along two single track welds (24 values) and the average value was evaluated (Table 2). During the experiment, the following parameters were changed - LP in the range of 175–400 W and LS in the range of 200–2000 mm/s.

2.2.2. Geometry of single-track welds

Based on the previous experiment, the second batch of single-track welds was focused on the track weld's geometry. The laser parameters were the same as in the previous test, but the ranges were narrowed according to the perspective process window, i.e., LP in the range of 200–350 W, LS in range of 500–1400 mm/s which corresponds to the input linear energy (LE) of 0.25–0.4 J/mm (expressed by Eq. (1). The track weld geometry was measured on metallographic cross-sections using a digital-light microscope (Keyence VHX-6000, Z250R lens, zoom 250×). The evaluated parameters were track weld width (1), height (2), and depth (3), as is shown in Fig. 2a.

$$LE = \frac{LP}{LS}\ (J/mm) \tag{1}$$

2.2.3. Influence of the samples geometry

As was already mentioned in the introduction, the porosity and surface roughness are affected by a base material's thermal conductivity. The total thermal conductivity of the whole component then further depends on it's shape and orientation. Therefore, the basic single-track experiment was modified in two steps to investigate their influence on the samples's shape. First, the geometry was changed into thin-wall geometry (3D single track) and then into the shape of the hollow strut, representing the geometry of lattice structure. Both modified geometries consist of one single track in each layer (Fig. 3b) that allows observing the changes caused by modified samples heat dissipation. The resulting thickness of the walls and hollow struts were compared with the single-track welds' width. The thin walls had a rectangular geometry of 10 × 2 mm and were produced in two orientations, i.e., vertical and inclined (35.26°), that corresponds with BCC and BCC-Z lattice unit cells' basic geometry. The hollow struts samples were produced in the same two orientations with the diameters range of 0.3 to 3 mm. Various dimensions and two orientations of the samles were used to describe the influence of size and orientation effects on the hollow strut thickness. The laser parameters were used within the perspective process window of LP and LS (LP 200-350 W; LS 500–1400 mm/s). The geometry was measured on metallographic cross-sections using a digital-light microscope (Keyence VHX-6000, Z250R lens, zoom 250×). The thickness values were measured as the average values between the two lines, each was made by interpolation of five border points (Fig. 3a).

2.2.4. Overlap parameter

The overlap experiment was performed to ensure sufficient connection between neighbouring single-track welds and avoid excessive remelting of material in their connection that can initiate the inter-weld porosity. The sample's shape was a hollow strut composed of two laser tracks (Fig. 4b). The OL parameter was chosen in the range of 0–55% of the hollow strut thicknesses. The nominal diameters of the two tracks hollow strut were 0.8; 1.2; 1.6; 2 mm. The track OL was evaluated based on the internal porosity (image analyses, ImageJ, threshold 100) measured in connection to the two tracks (Fig. 4a). The results were evaluated from metallographic cross-sections captured by a digital-light microscope (Keyence VHX-6000, Z250R lens, zoom 250×).

2.3. Analysis of porosity, surface roughness and dimensional accuracy

The shape and dimensions of the component can significantly affect the formation of the SLM manufacturing imperfection [11]. Therefore, to obtain meaningful results, the sample's shape must be as close as

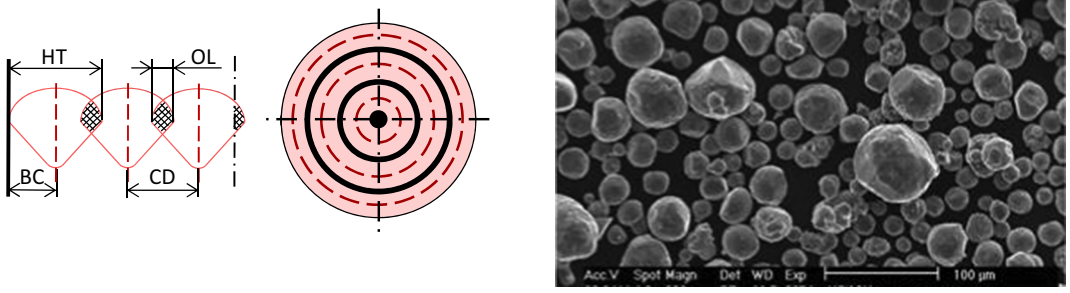

Fig. 1. (a) The parameters of the contour strategy: hollow strut thickness (HT), overlap (OL), contour distance (CD) and beam compensation (BC); (b) the shape of powder particles (scanned by SEM).

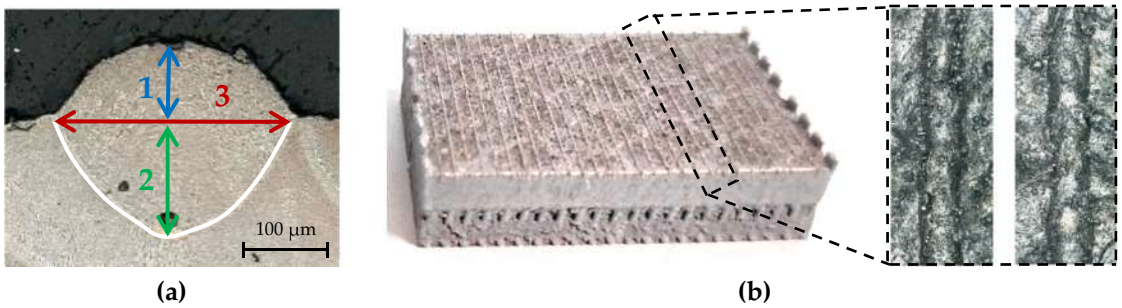

Fig. 2. (a) Measured geometrical parameters of the single-track welds; (b) the single-track sample.

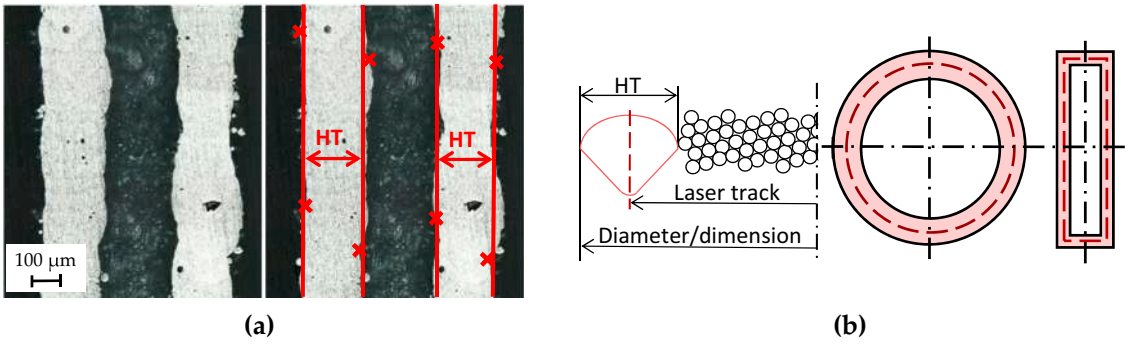

Fig. 3. (a) Methodology of the thin-wall and hollow strut thickness evaluation; (b) geometry of hollow strut and thin-wall.

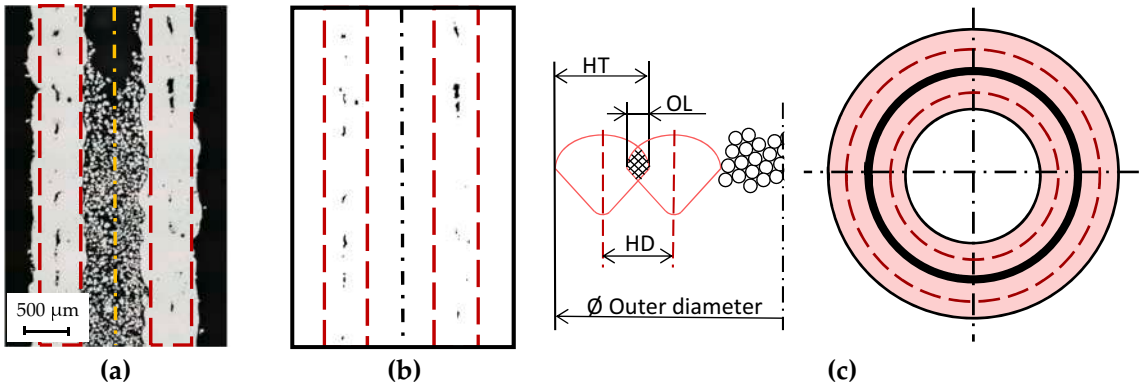

Fig. 4. Porosity measured in the connection of neighbouring laser tracks (a) metallographic cross-section of two track hollow strut, (b) the final monochrome image analysed by ImageJ software, (c) geometry of hollow strut consists of two laser tracks.

Table 1
The list of the applied SLM parameters in the study.

Parameters	1st loop	2nd loop	3rd loop
Laser process param.	Values from previous hollow strut experiment		**LP** and **LS** according to **RSA**
Dir. of contour production	Outside-in	Inside-out	
Track width	Previous hollow struts results	Response Surface Analysis (**RSA**)	
Beam Compensation	1/2 of the thickness of the hollow strut samples	1/3 of the thickness of the hollow strut samples	
Overlap	30 %	35 %	

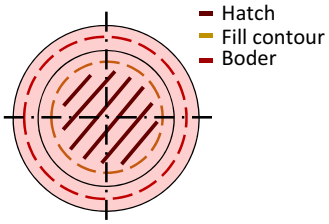

Fig. 5. The default SLM process parameters (a) schema of the meander strategy (b) table of the process parameters.

possible to the final part. In the case of the lattice structure, the strut geometry was chosen. The experiments were further focused on obtaining the porosity distribution, pores size, surface roughness and dimensional accuracy of the strut samples.

The struts were produced in two orientations, i.e., vertical and inclined (35.26°), that corresponds with BCC and BCC-Z lattice unit cells' basic geometry. The struts' diameters were used in the range of 0.6–3.0 mm, and the thickness of the track (HT) was set differently for each diameter according to the previous results. Other parameters were constant and were applied according to the testing loop, as is shown in Table 1.

Based on the first testing loop results, the influence of the contour track production order was evaluated on the level of porosity; therefore, the inside-out direction of production was applied in the second and third loops to reduce material imperfection for strut diameters over 1.0 mm. Moreover, finally, the OL was changed to 35% according to porosity results (Figs. 15b, 13) and the BC of 1/3 hollow strut thickness was used after the first results of dimensional analysis. All results were compared to the default SLM process parameters i.e., meander hatch strategy (Fig. 5a).

X	Hatch	Fill cont.	Border
LP (W)	350	250	300
LS (mm/s)	1150	555	600
LE (J/mm)	0.3	0.45	0.5
OL (%)	50	50	50
Laser focus	0	−4	0

2.4. Porosity analysis

The porosity was analysed in two ways. First, the porosity was evaluated in the connection of the two laser tracks by digital-light microscope. In this case, the cross-section images of the two tracks hollow strut were captured by the digital-light microscope (Keyence VHX-6000, Z250R lens, zoom 250×) and analysed using ImageJ software. Then the porosity value was evaluated as the percentage of black in the monochrome images. The second, a micro-computed tomography approach (μCT, GE phoenix v | tome | x L240, Waygate technologies, Hürth, Germany) was used for porosity analysis in the whole volume of the strut samples and evaluation of the influence of contour strategy parameters on the occurrence of material imperfections (Fig. 6a). The following adjustment of the measurement was used i.e., a micro-focus X-ray tube with a voltage of 130 kV, a current of 100 μA and a 0.5 mm wide copper filter. The achieved linear voxel resolution was 16 μm for all samples with a minimal pore volume of 2 voxels. The scanned data were further reconstructed in the Datos reconstruction software and processed in VGStudio MAX 3.1 software (Fig. 6b,c,d,e). The threshold value was obtained automatically from common scan of all samples (Fig. 6a) and applied to segmented samples This was performed to ensure the comparability of the results of struts porosity [31]. The main outputs from the μCT analysis were 3D images of the material porosity for all produced struts (more than 232 samples), i.e., its level and distribution for each strut. The μCT was also used to digitize a struts shape to STL format which was used for dimensional accuracy and surface roughness analysis. These outputs enabled to find the dependences of porosity and surface roughness on the strut diameter and LE.

2.5. Shape and surface roughness analysis

$$R_a = \frac{1}{N}\sum_{i=1}^{N}|y_i| \ (\mu m) \tag{2}$$

The surface roughness and shape of struts were investigated using the digitised STL data from μCT even though relatively high voxel size resolution of 16μm. The main purpose of this analysis was to use large data set from μCT analysis and find out dependences of these parameters according to the strut diameter and LE, not exact values.

The evaluation was performed in the GOM Inspect software by the following procedure. First, the digitalised data was aligned to CAD data using the Best fit method. The surface roughness was measured as dimensional deviation from CAD in 200 points of line selection on the down-skin surface of the inclined strut (Fig. 7a). The deviations were converted to Ra surface roughness according to Eq. (2). Then, the strut's actual diameter was measured by fitting an ideal Gauss cylinder (used selected point: 3 sigma) to the largest possible area of the digitalised data (Fig. 7b).

2.6. Numerical simulation

The transient thermal simulation was performed in Ansys Workbench software to clarify the observed effects in porosity and surface

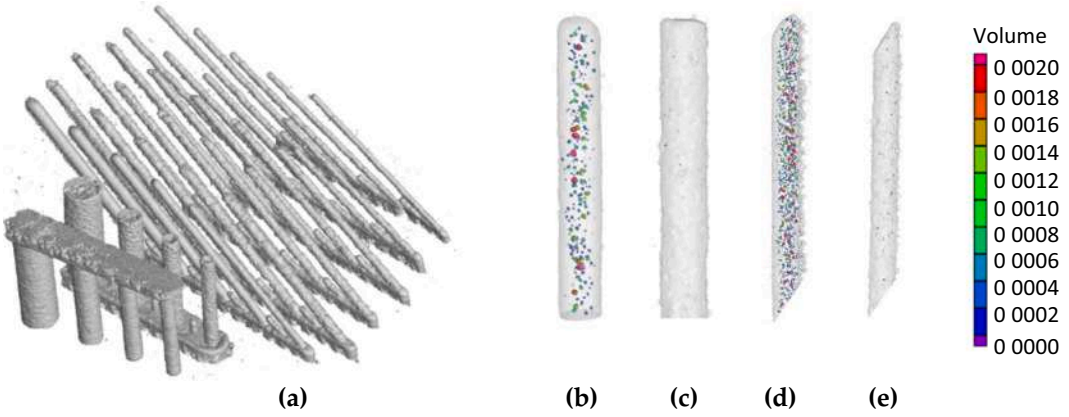

Fig. 6. Porosity analysis (a) group of samples scanned together, (b), (c) internal porosity of vertical struts, (d), (e) inclined struts.

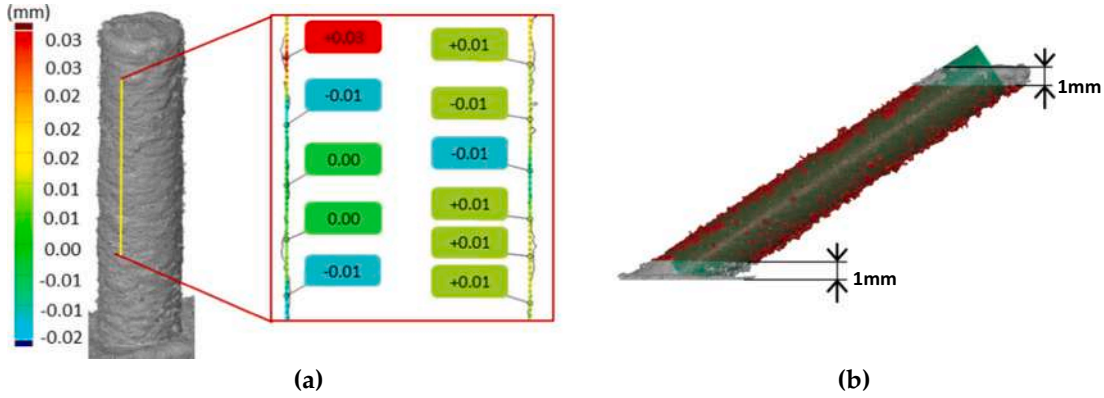

Fig. 7. (a) Surface roughness analysis on a vertical strut, (b) the inclined strut with fitted Gauss cylinder and red marked area of selection. (For interpretation of the references to colour in this figure legend, the reader is referred to the web version of this article.)

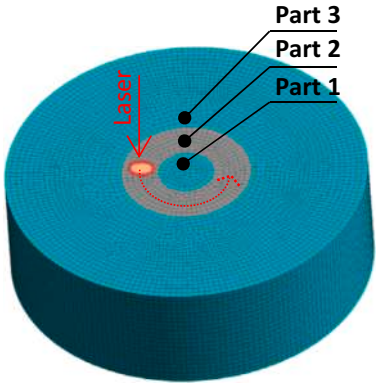

Fig. 8. The numerical model of the transient thermal simulation.

Table 2
The results of the first evaluation of the single-track weld's width. The marked samples are shown in the figure above.

TW (μm)	Laser Speed (mm/s)																			
Laser Power (W)	200	300	400	500	600	700	800	900	1000	1100	1200	1300	1400	1500	1600	1700	1800	1900	2000
175	353	310	261	290	246	221	214	199	223										
200	401	343	303	286	317	271	240	210	201	210									
225		374	309	271	255	214	203	199	174	163	145								
250		344	314	270	253	233	223	201	180	161	163	159							
275			380	346	332	289	262	277	235	227	221	201	149						
300			305	325	308	267	260	232	223	202	211	193	183	192	186				
325				333	316	275	274	262	258	207	199	200	196	189	176	168			
350				358	336	328	317	300	261	259	259	205	200	199	209	205	352		
375					317	308	201	372	370	272	267	250	287	230	237	239	223	217	
400					357	332	358	301	273	234	236	223	214	206	223	216	212	201	210

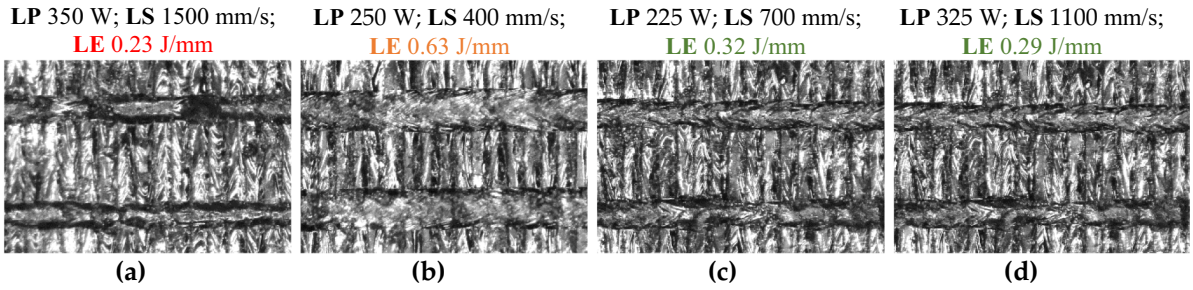

Fig. 9. The images of single-track welds captured by a digital-light microscope - (a) LE = 0.23 J/mm; (b) LE = 0.63 J/mm; (c) LE = 0.32 J/mm; (d) LE = 0.29 J/mm.

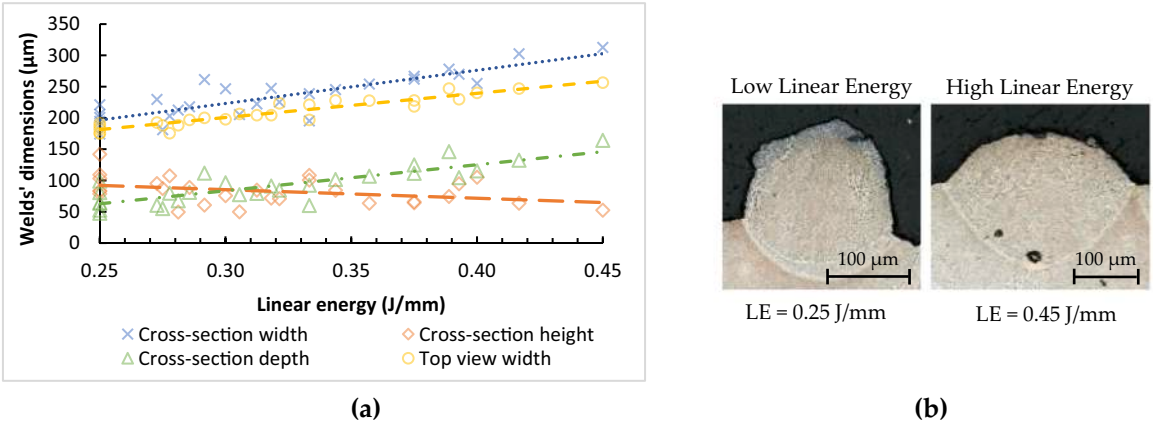

Fig. 10. (a) The geometrical parameters of the single-track welds vs. linear energy, (b) the examples of the typical shapes of the single-track welds.

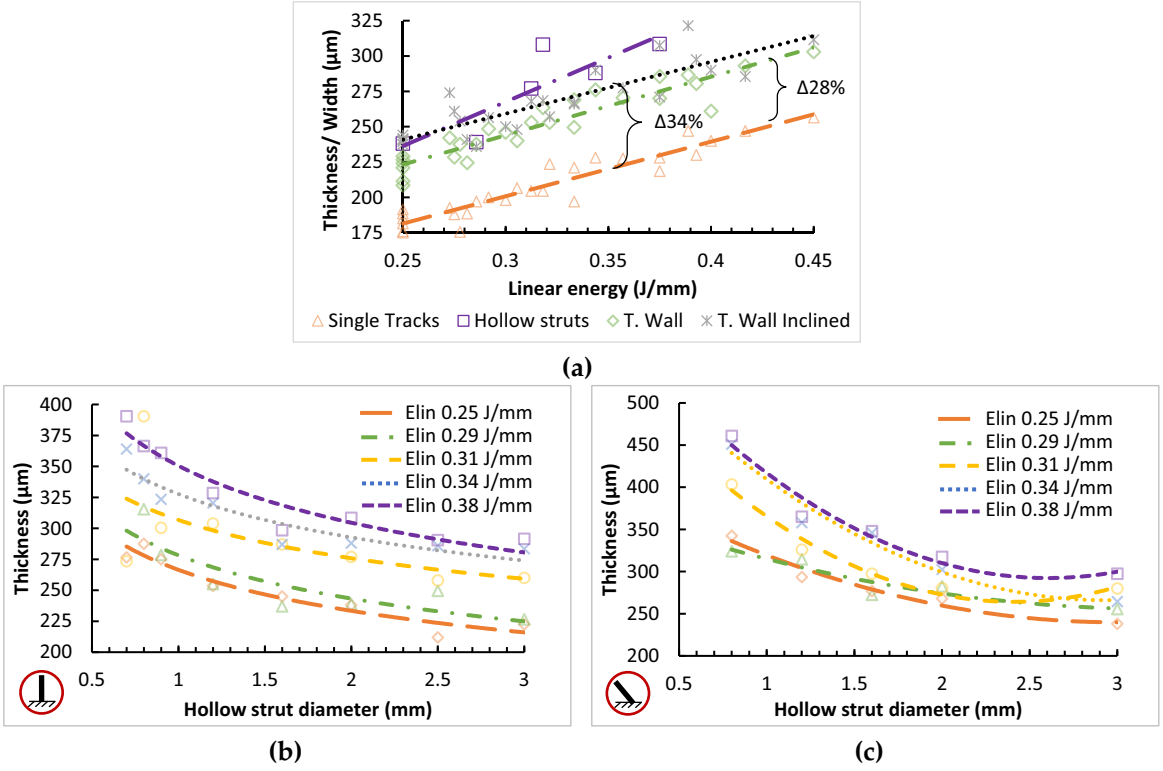

Fig. 11. (a) The comparison of the single tracks width, hollow struts, and thin walls thickness, (b) the chart of the HT parameters vs. LE for vertical hollow struts (c) inclined hollow strut.

roughness. The numerical model represents the situation during the SLM production of the strut when a part of the strut was already produced, and the next layer is producing. The height of the model is 1 mm and consists of three parts for simulation of hollow strut experiment (Fig. 8). The Part 1 and Part 3 represent surroundings powder bed, and the Part 2 is solidified AlSi10Mg material. The mesh of all parts was created by the hex dominate Solid 90 elements with size of 0.05 mm (used layer thickness). Material parameters were used from Ansys Additive Manufacturing materials library and modified according to studies [25,32–34]. On the upper surface of all three parts the air convection was applied. The heat source (laser) was applied using the Moving Heat Source extension where the laser's circular trajectory was defined. The input energy was defined using LP and LS parameters. For simulation of full strut, the model was modified to consist only of Parts 2 and Parts 3. There is no powder in the centre part of the strut; therefore, Part 1 was removed, and Parts 2 was extended and filled the centre area of the strut.

3. Results

3.1. Laser process parameters window

Table 2 shows the results of the track width parameter (TW) measured by a digital-light microscope and the area of fine continuous track welds evaluated by a visual check (green area of the table). All samples were sorted according to the track weld's shape and quality into three types of colours. Fig. 9a shows the balling effect, which is typical for low input energy production (red colour). In Fig. 9b, the track weld's width is large and the height too low (orange colour). It was caused by the high input energy of the laser. In Fig. 9c,d, there is shown ideal situation when the single-track welds were continuous without any interruptions (green clolour). The final perspective window is in the range of LP 200-350 W; LS 500–1400 mm/s; linear energy LE 0.25–0.4 J/mm.

The previous experiment was performed again for a deeper evaluation of the track welds' geometry using fine cross-sections images. The results are presented in Fig. 10a, where the strong dependence of the track welds' geometry on the LE is shown. The results show that due to the liquid melt pool's surface tension at a low energy level, the track weld's height is high, but the width and depth are low (Fig. 10b-low liner energy). With increasing LE, the track weld width and depth are growing, but the height is decreasing (Fig. 10b-high linear energy). The comparison of the track welds' width evaluated from the cross-sections and the digital-light microscope shows the same trend with deviation caused by different evaluation approaches. In the cross-section case, the value of the width was measured accurately but only in one section of the track weld. It could cause small deviations compared to the average values measured by a digital-light microscope which are more representative for the whole track. Based on that, the microscope measurement's average values were further used. According to the study [21], the depth to width ratio was used to analyse the suitability of process parameters. This parameter was lower than 0.5 (−) for all tested process parameters, particularly in the range of 0.26–0.49. It means that those process parameters are suitable to produce components from AlSi10Mg material by SLM [16]. The obtained values will be used for comparison with modified experiments focused on lattice structure production.

3.2. Influence of samples geometry on track width

This experiment aimed to compare a walls thickness measured on the specific geometry of thin-wall and hollow strut with the single-track weld's width. The vertical walls' results were in the range of 209–303μm and showed a significant dependence on input linear energy (LE) as was the same in the case of single-track welds. The obtained values of the thickness were in average about 28% larger than TW values in the whole range of tested process parameters (Fig. 11a). In the case of inclined walls, the deviation was in average even 34% higher. The main reason is the lower heat transfer which decreases with the wall's inclination. Due to the low thermal conductivity of the surrounding powder bed, the energy is accumulated in the material and causes an increase in the wall thickness.

The results of the vertical hollow strut thickness (HT, diameter of 2 mm) had a similar trend as thin walls; however, the thickness was increasing at higher linear energies in comparison to thin walls. The cross-section images of inclined hollow struts showed the different thickness in the up-skin and down-skin areas (Fig. 12b). This deviation was probably caused by the thermal energy accumulation described above and in studies [12,16]. As is shown in Fig. 11c,d, the various nominal diameters of the hollow struts were produced using five levels of input linear energy (LE) in the range of 0.25–0.38 J/mm. The results showed that the HT parameter measured on a small diameter is larger compared to the HT parameter measured on a larger diameter, even if the same process parameters were used. The biggest differences were shown in the highest LE of 0.38 J/mm, where the HT parameter measured on the nominal diameter of 0.8 mm was 391μm and for the diameter of 3.0 mm was 292μm i.e., it is difference of 34%. In the case of

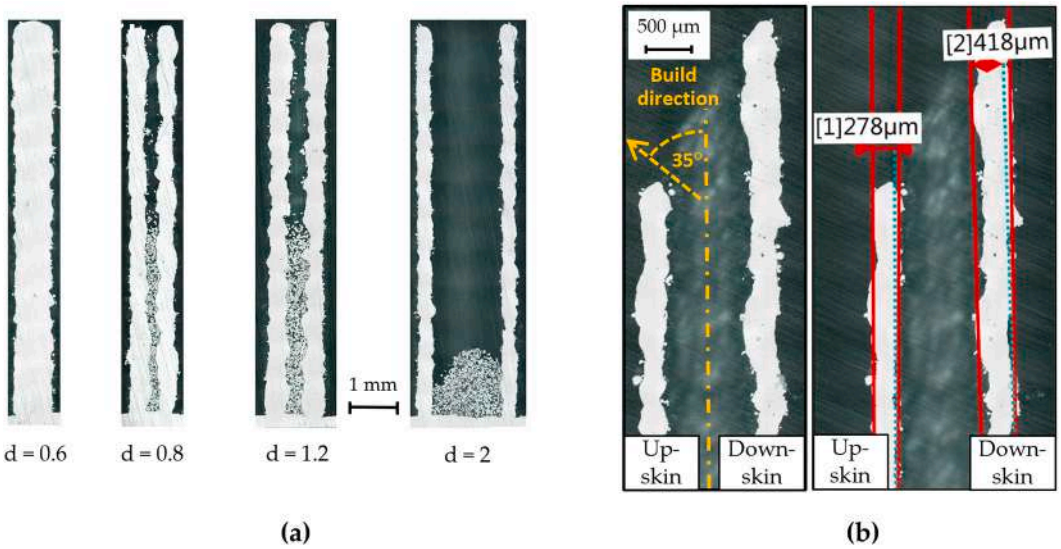

Fig. 12. (a) The digital-light microscope images of the vertical hollow strut cross-sections, (b) different up-skin and down-skin thickness measured on the metallographic cross-section of inclined hollow struts.

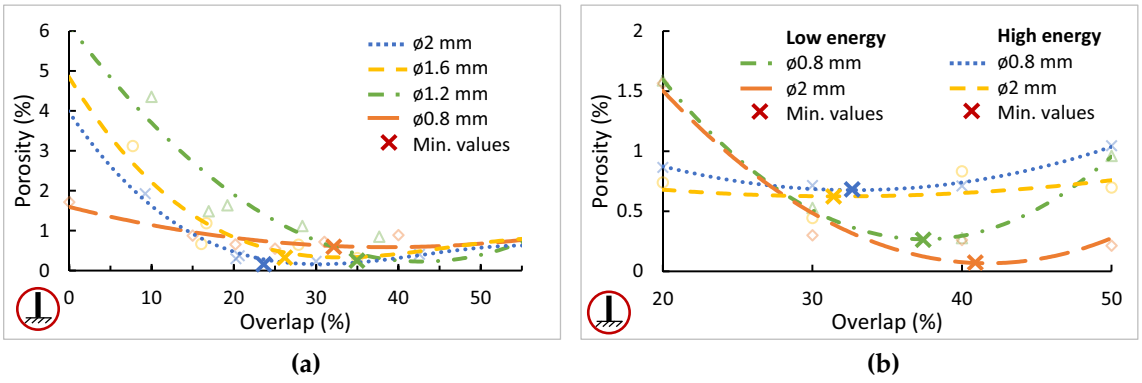

Fig. 13. The chart of porosity vs. overlap (a) OL in the range of 0–55%, (b) OL in range of 20–50%.

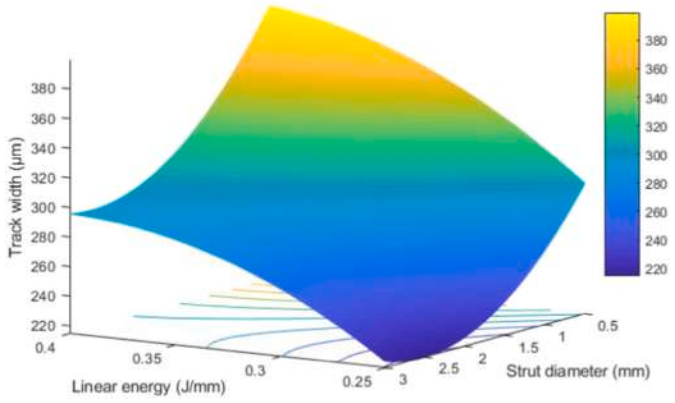

Fig. 14. Hollow strut's thickness vs. linear energy and strut diameter from Response surface analysis for vertical struts.

the diameters of 0.3–0.6 mm, both sides of the hollow strut were even connected, and a fully volumetric strut was created. These results are in line with the results presented by Dong et al. [11] where internal porosity and mechanical properties depend on the sample's diameter (up to 4 mm). The actual results clearly show that the deviation in the hollow strut's thickness and single tracks welds is significant. Therefore, it is necessary to implement HT parameter into the SLM laser strategy for lattice structure production to avoid internal defects.

3.3. Single-track weld overlap parameter

As it was mentioned above, the overlap (OL) parameter is expressed as percentage value of the hollow strut thickness (HT) and mainly affects the porosity in connection of two neighbouring tracks. Due to the small dimensions of lattice structures, the internal porosity influences their mechanical properties more than in case of bulk material; and therefore, the overlap is more important. The OL's correct setting is based on the HT parameter, which depends on dimensions of the lattice structure and the liner input energy (LE) of the SLM process.

The porosity values were measured in the transverse cross-section of hollow struts composed of two laser tracks. In Fig. 13a, the first loop of the experiment results is present. As it is shown, the porosity decreased with increasing OL parameter, and the minimum value was reached in the range of 20–50% for all tested dimensions. The second loop was focused on the perspective range of 20–50%, and only limit values of previously tested parameters were used, i.e., diameters of 0.8, 2 mm (thin and large diameter representant) and LE of 0.25, 0.38 J/mm (low and high energy representant). The results showed that OL parameter is not dependent on the lattice structure's dimension but on LE (Fig. 13b). Therefore, the optimal OL values are in the range of 30–40% for all tested parameters (thin, large diameter; low, high energy).

3.4. Strut thickness prediction based on response surface analysis

As it is clear from previous results, the definition of the SLM process parameters for lattice structure manufacturing is complex task affected by input linear energy, size, and orientation of the lattice structure. To include the effects to the contour strategy parameters, the response surface analysis (RSA; part of the Design of Experiments) of the hollow strut thickness (HT) parameter was prepared. The RSA allowed determining the exact value of HT for specific input linear energy (LE) and the strut's nominal diameter (SD). The HT values were interpolated by the quadratic surface described by Eq. (3) with the reliability of R2 = 78% for vertical struts (Fig. 14) and by Eq. (4) with the reliability of R2 = 86% for inclined struts. Thus, it is possible to predict the values also for the parameters that were not tested exclusively.

The comparison of the RSA prediction and the measured data for the specific parameters are shown in Table 3 (vertical hollow struts, linear energy of 0.34 J/mm). The average deviation was 2.18%, and the largest deviation was 6.72% in the case of 0.9 mm strut diameter.

$$\mathbf{TH}_{\mathbf{ver}} = -134 + 2736\bullet\mathrm{LE} - 94.3\bullet\mathrm{SD} - 3177\bullet\mathrm{LE}^2 + 21.25\bullet\mathrm{SD}^2 - 54\bullet\mathrm{LE}\bullet\mathrm{SD}\ (\mu\mathrm{m}) \quad (3)$$

$$\mathbf{TH}_{\mathbf{inc}} = -31 + 2450\bullet\mathrm{LE} - 101\bullet\mathrm{SD} - 2025\bullet\mathrm{LE}^2 + 35.8\bullet\mathrm{SD}^2 - 301\bullet\mathrm{LE}\bullet\mathrm{SD}\ (\mu\mathrm{m}) \quad (4)$$

3.5. Full strut verification

In the following chapter, the previous results were used for the definition of the SLM contour strategy for lattice structure manufacturing and their influence was observed on the material porosity, surface roughness and the dimensional accuracy.

Table 3
The comparison of the response surface analysis data and measured values.

Strut Ø (mm)	0.7	0.8	0.9	1.2	1.6	2	2.5	3
Predicted HT (µm)	362.5	354.4	346.8	326.3	304.9	290.4	281.8	283.8
Measured HT (µm)	364	340	323.5	320.5	287	288	286	283.5
Deviation (%)	−0.4%	4.1%	6.7%	1.8%	5.9%	0.8%	−1.5%	0.1%

Table 4
The comparison of the vertical struts produced by the default SLM process parameters and the contour strategy (LP = 200 W, LS = 700 mm/s, LE = 0.29 J/mm).

D_{nom} (mm)	0.6	0.7	0.8	0.9	1.0	1.25	1.5	2.0	3.0
Por. (%)	1.74	1.79	1.97	1.92	1.9	0.97	0.78	0.24	0.06
Default	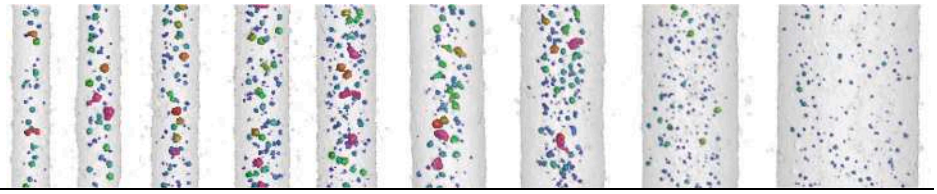								
Por. (%)	0.02	0.23	0.36	0.64	0.69	0.32	0.05	0.04	0.09
CS 1st loop	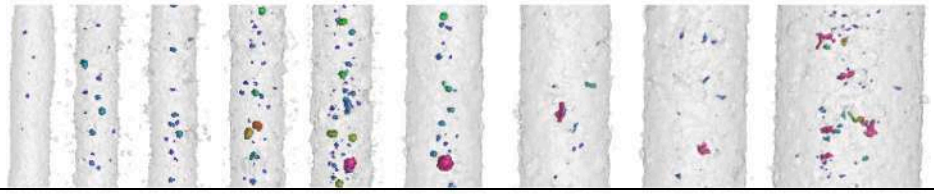								
Por. (%)	0.01	0.01	0.09	0.07	0.02	0.01	0.01	0.01	0.04
CS 2nd loop	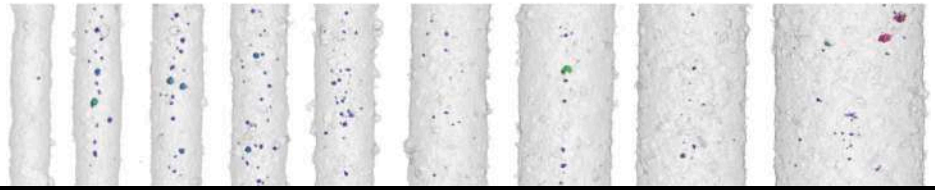								

Table 5
The comparison of the inclined struts produced by the default SLM process parameters and the contour strategy (LP = 200 W, LS = 700 mm/s, LE = 0.29 J/mm).

D_{nom} (mm)	0.6	0.7	0.8	0.9	1.0	1.25	1.5	2.0	3.0
Por. (%)	0.11	0.13	1.11	1.44	1.16	2.04	1.64	0.88	0.25
Default	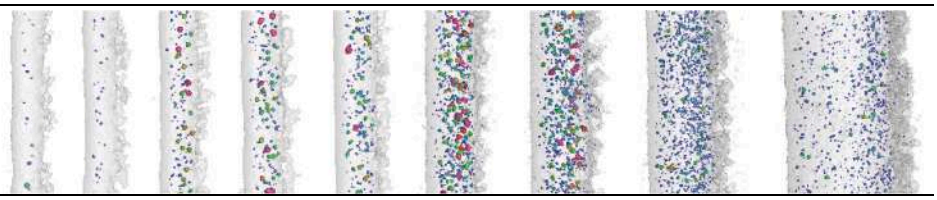								
Por. (%)	0.24	0.25	0.54	0.38	0.09	0.62	0.58	0.64	0.47
CS 1st test loop	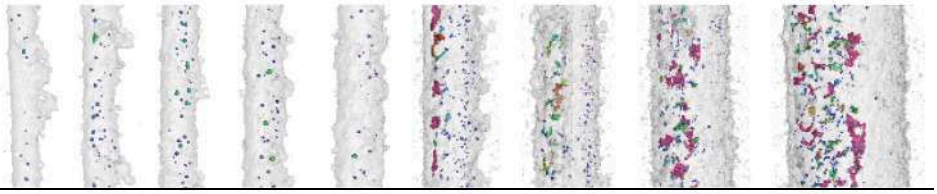								
Por. (%)	0.11	0.21	0.08	0.12	0.33	0.03	0.02	0.01	0.04
CS 2nd test loop	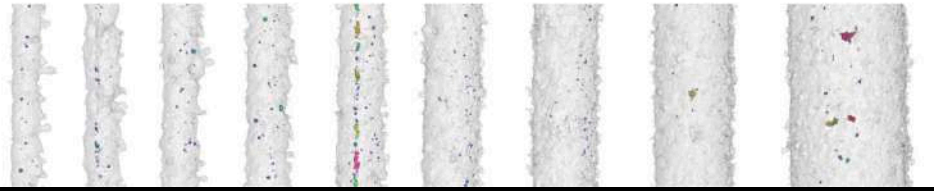								

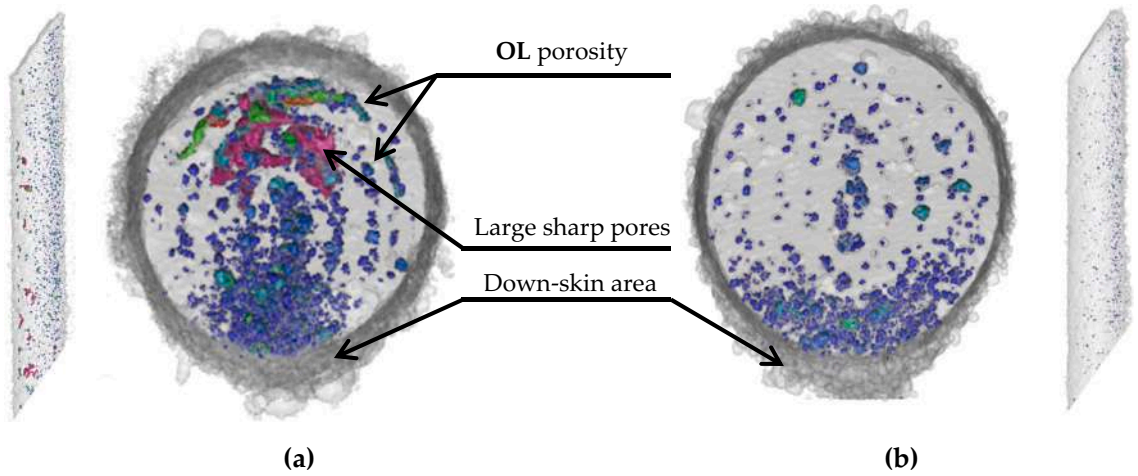

Fig. 15. (a) The top view of the inclined strut (d = 2 mm, LP = 300 W, LS = 800 mm/s, LE = 0.38 J/mm) (a) the first testing loop (b) the second testing loop.

3.5.1. Material porosity

The material porosity experiment was divided into two steps. In the first testing loop, the same parameters were used as in case of hollow struts experiment, i.e., the strut diameters and specific hollow strut thickness (HT) values (Fig. 11c). The reason was to minimise unexpected circumstances which could influence the results. The other contour strategy parameters were derived from the HT parameter, i.e., the distance of the contour trajectories CD = HT - OL, the contour overlap between the neighbouring track of 30% (OL = 0.3 x HT), and the beam compensation BC = 0.5 x HT. The material porosity measured by μCT was chosen as the main response parameter.

The results of the first testing loop showed a relatively high level of porosity in thin vertical struts for all tested input linear energies (LE) (Fig. 16a,b). The default SLM process parameters with meander hatch strategy reached the porosity level of 2%; the contour strategy (CS) approach reached an interval between 0.16% and 1.35% based on the used LE. The porosity decreases according to LE and the strut nominal diameter. Tables 4 and 5 show the graphical comparison of the level and distribution of porosity obtained using meander hatch and the CS strategy. The meander hatch strategy led to a high porosity level with spherical and equally distributed pores in the whole volume. An exception was the large vertical struts (d = 2 and 3 mm), where the

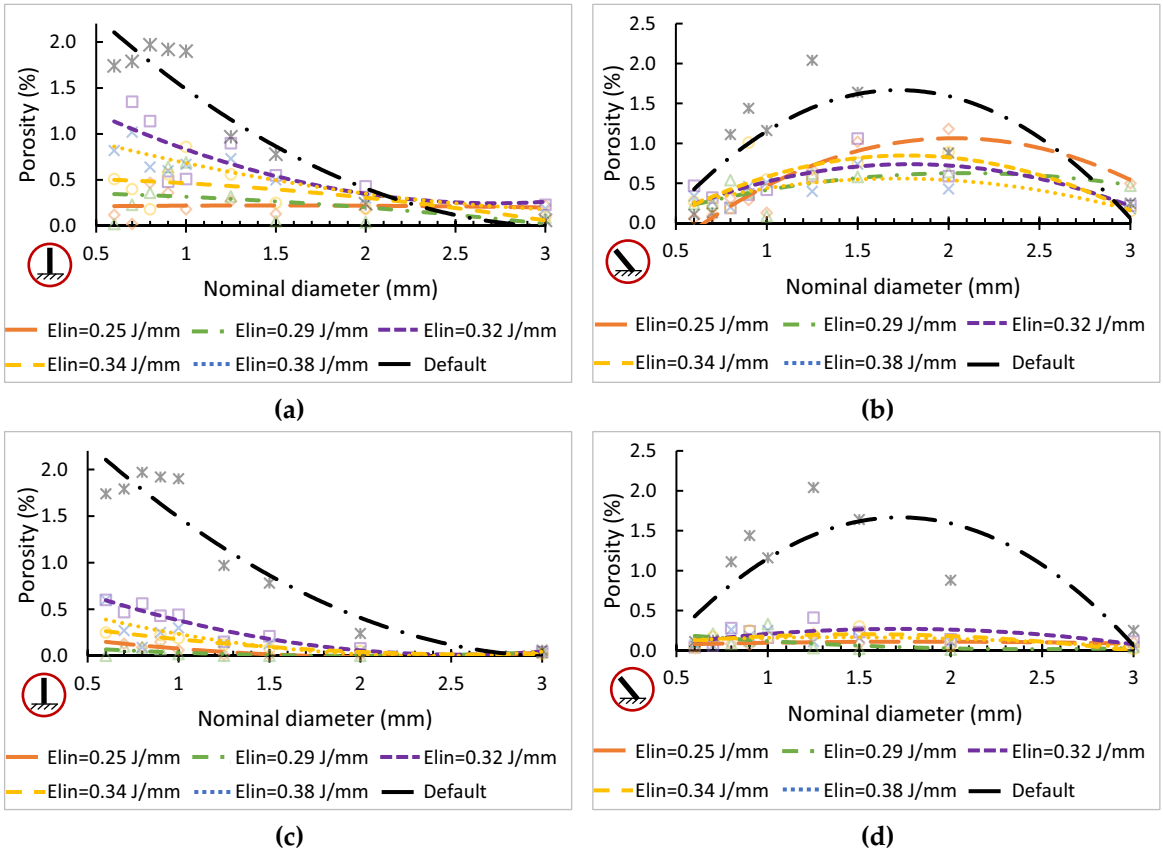

Fig. 16. Comparison of the meander and contour strategy (a) the level of porosity for the vertical struts (b) the level of porosity for the inclined struts in the first loop; (c), (d) second loop.

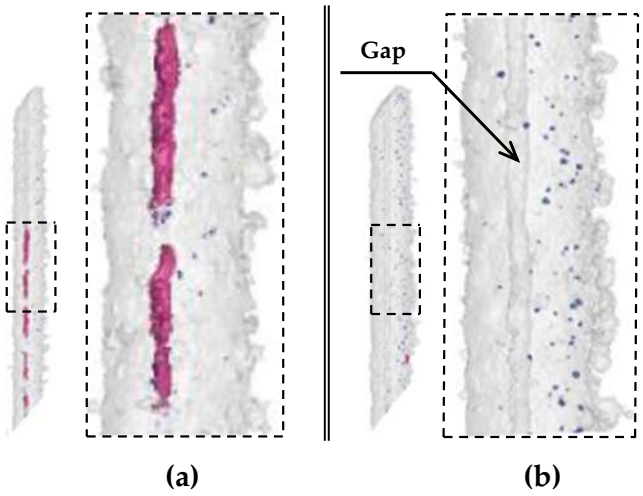

Fig. 17. The struts with non-melted pores in the middle axis area (a) LP = 225 W, LS = 900 mm/s, LE = 0.25 J/mm, OL of −10.65%; (b) LP = 300 W, LS = 800 mm/s, LE = 0.38 J/mm, OL of −11.28% (un-melted area in the strut axis).

porosity was low. It was caused by high thermal conductivity in larger struts that could be considered as bulk material for which the default process parameters are mostly optimised. A similar conclusion was reached by Dong et al. [11] for dimensions over 4 mm.

The CS porosity results were presented by the μCT images of the struts produced with input linear energy LE = 0.29 J/mm (middle value from tested range). The CS approach showed a lower porosity level for both vertical and inclined thin struts (up to 1 mm). The porosity was equally distributed; however, its level grew with the increasing diameter of the strut, and large sharp pores occurred over the diameter of 1 mm. It relates to the direction of the contour track production and the number of tracks. The large struts (the diameter over 1 mm) consisted of 3 and more laser tracks (depends on used LE). It led to the lack of powder inside the strut if outside-in direction of the contour strategy was used. This was caused by drag of the surrounding powder into the melt pool during powder melting [35]. This effect relates to the change of the material state because the density of powder is much lower than melted material and therefore, larger volume of the powder is consumed for the melt pool. To minimise the effect, the inside-out direction will be used for the next test loops. Moreover, the sharp overlap porosity was found in the top view images (Fig. 15a). It could be created due to insufficient overlapping of neighbouring contour tracks in the up-skin area where the thickness of the track is thinner than in the down-skin area above the powder bed. Based on that, the OL parameter was increased about 5% to 35% which stabilise the situation in up-skin area. But on the other hand, it can increase a porosity in the down-skin area.

The second testing loop showed significant improvement in all observed parameters. A change of laser scanning direction eliminated the sharp pores. The porosity level was significantly decreased using the hollow strut thickness (HT) obtained from Response Surface Analysis (RSA) and changing the OL to 35%. The results are shown in Figs. 16c, d and 15b. where the porosity level reached values in the interval of 0.01% (LE = 0.29 J/mm) to 0.6% (LE = 0.32 J/mm) for vertical struts and even in the interval of 0.07% (LE = 0.25 J/mm) to 0.4% (LE = 0.32 J/mm) for inclined struts. Tables 4 and 5 show the gradual evolution of the results and the clear positive effect of the CS strategy on all observed struts' parameters. The results also showed the issue with unmeted centre areas of some struts. If the non-compatible combination of the HT and strut diameter is used, the gap could occur in the strut centre (Table 5 - 1st loop d = 1.5 mm; 2nd loop d = 0.7 and 1.0 mm).

The last testing loop mainly aimed to reduce the unmelted area in the struts' centre (Fig. 17). Using RSA prediction, the optimal combination of the process parameter was found for each strut diameter. Thereby, the constant OL parameter was reached in the whole cross-section of the vertical and inclined struts (Table 6). The porosity results generally showed very low level of spherical porosity without unmelted areas, i.e., in case of inclined struts max. 0.16%; in case of vertical struts max. 0.19%. It confirms that the results of RSA analysis and OL parameter of 35% allow achieving very low values of porosity level for various diameters of the struts using different SLM parameters within the defined perspective process window.

Based on the results, the contour strategy and customisation of the process parameters for various dimensions of the lattice structure seem to be an effective approach to eliminate the material imperfections.

3.5.2. Dimensional accuracy

The results of the first testing loop are shown in Fig. 18a,b, where the dimensions of the struts are generally smaller than the nominal diameters. This issue could relate to the circular trajectory of the laser which means the higher laser speeds along the outer part of the trajectory due to its curvature (Fig. 20) and therefore HT parameter is thinner. It affects beam compensation parameter (BC; Fig. 1) which was too high and caused the dimensional deviations. Eq. (5) was created to reach the optimal dimensional accuracy based on the evaluation. Then, the BC parameter was changed to BC = BCcoef x TH. The resulting BCcoef = 0.34 was further used in the next testing loops, which expressed the average value used for all strut diameters. BCcoef was evaluated based on the nominal strut diameter (SD) and diameter of the first peripheral

Table 6
The chosen results from the third validation testing loop.

	Vertical					Inclined				
D_{nom} (mm)	**0.6**	**0.8**	**1.25**	**2.0**	**3.0**	**0.6**	**0.8**	**1.25**	**2.0**	**3.0**
LP (W)	214	325	243	263	263	171	251	263	263	263
LS (mm/s)	950	950	950	864	861	950	950	833	665	928
LE (J/mm)	0.23	0.34	0.26	0.30	0.31	0.18	0.26	0.32	0.40	0.28
Por. (%)	0.02	0.19	0.09	0.04	0.02	0.02	0.07	0.12	0.07	0.01
CS 3th loop										

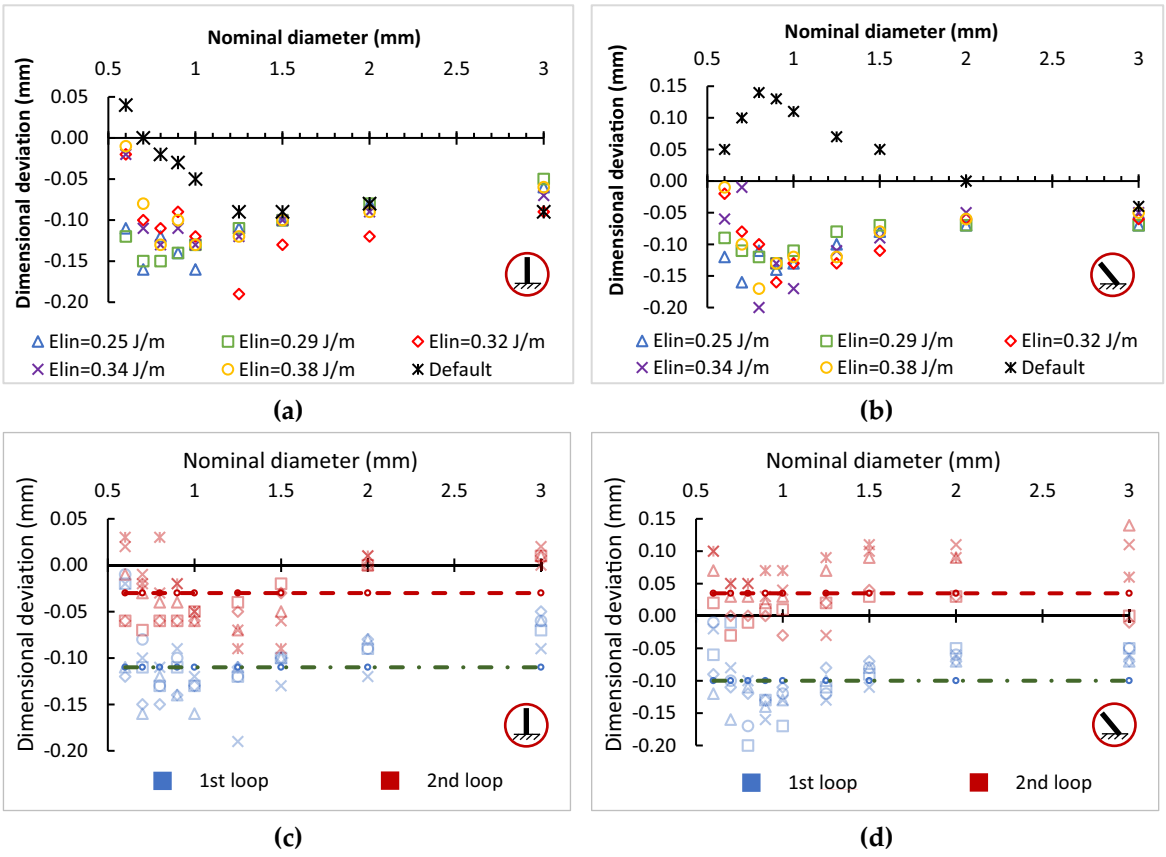

Fig. 18. The charts of the dimensional deviations from the nominal diameter of the first loop (a) vertical strut, (b) inclined strut; comparison between the first and second loop with marked median values for (c) vertical strut, (d) inclined strut.

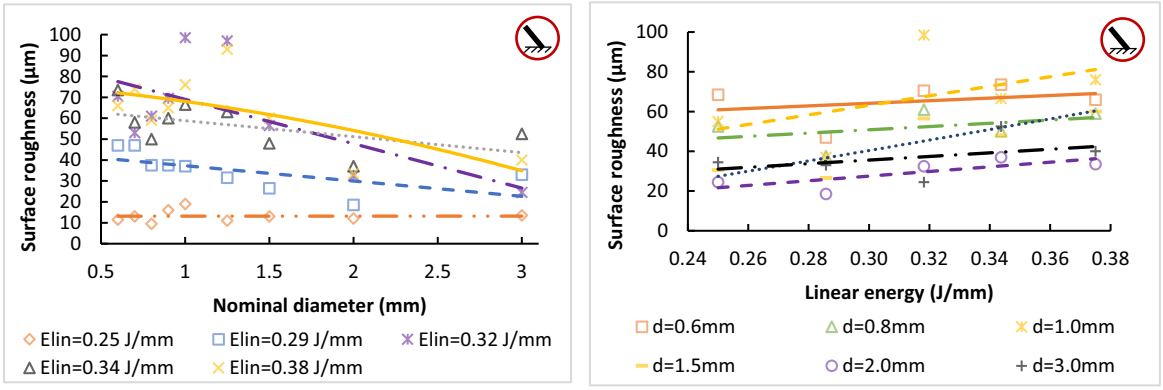

Fig. 19. The surface roughness (a) dependence on the dimensions of the strut (b) dependence on the linear energy.

contour track (PCD).

$$\mathbf{BC_{coef}} = \left(\frac{\mathrm{SD} - \mathrm{PCD}}{2}\right) \Big/ \mathrm{HT}\ (-) \tag{5}$$

The modified BC parameter's influence is presented in Fig. 18c,d. As the comparative parameter between the first and second testing loop, the median value of the dimensional deviation was used. In the case of the vertical struts, the median value was changed from −0.11 mm to −0.03 mm. In the case of inclined struts, the median value changed from −0.10 mm to 0.04 mm. In both charts, two areas of results could be found. The dimensional deviations of the larger vertical struts are low. However, in the case of thin struts, the deviations are higher, and the values are unstable. The inclination of the struts' leads to better accuracy in the case of thin struts, but on the other hand, the deviation of the larger struts is higher than in the first testing loop. In general, the change of the BC_{coef} parameter from 0.5 to 0.34 helped significantly reduce the dimensional deviations; however, to reach even better accuracy, the BC parameter must be evaluated individually according to the struts' size, the orientation of the struts and used LE.

3.5.3. *Surface roughness*

Surface roughness (Ra) was measured on the inclined struts' down skin surface where the Ra values are the highest [14]. The contour strategy approach shows the same trend for all levels of the tested LE, i.

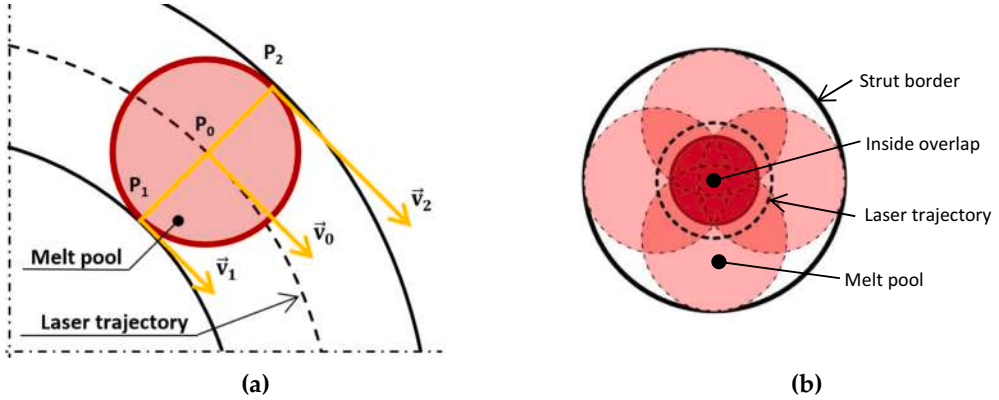

Fig. 20. (a) Schema of the circular trajectory influence on the change of the actual velocity of the melt pool, (b) Schema of the possible remelting in the thin struts [36].

e., the small diameters have relatively high Ra values, which decrease with the increasing size of the strut (Fig. 19). In higher linear energies, the differences between the small and large struts are more significant. This effect is related to the dissipation of thermal energy from the melt pool area and the size of the struts. With increasing LE, the surface roughness Ra increases linearly across all tested diameters (Fig. 19b). This conclusion matches with the study [16] where they focused on a wide range of LE and the strut diameter of 2 mm.

Surface roughness partially affects also dimensional deviations which can be seen by comparing the charts of Figs. 18 and 19a. The charts show that the struts with a small diameter have a larger deviation of the dimensions and higher surface roughness than larger struts.

4. Discussion

The presented results aimed to describe the SLM process's specific behaviour during the manufacturing of thin-strut lattice structure. Due to low volume of material, the lattice structures are highly affected by thermal behaviour of SLM melting process; therefore, the geometry and size of produced lattice structures must be considered. For this purpose, the Contour Strategy (CS) parameters was developed which led to elimination of typical imperfections of lattice structure, such as dimensional inaccuracy, high surface roughness and porosity.

4.1. The process of the contour strategy optimisation

4.1.1. Comparison of the single tracks, thin wall, and hollow struts results

The first differences have already appeared in the basic SLM experiment, respectively, in comparison of the single-track welds and thin-walls, and hollow struts thickness results. The thin perpendicular walls' thickness was about 28% wider than the single-track welds' width, and the inclined walls was even 34% (Fig. 11a). The hollow strut's thickness showed a similar deviation as the inclined walls (Fig. 11b); however, more significant dependence on the input energy (LE) was observed. In previous studies [11,17], the need for similarity of the samples shape and final components was mentioned. Therefore, the hollow strut's geometry was finally used to design the CS parameters.

Based on the wider thickness of hollow strut samples, the hypothesis was created that the circular shape of the laser CS trajectory and their small diameter causes the changes in the melt pool's thermal behaviour. Due to a circular shape of laser trajectory with a very small diameter, the inner part of the melt pool moves slower than the outer part (Fig. 20). This locally increases the input energy Eqs. (8), (9) because the laser exposes the inner part of the strut longer and the melt pool expands. Then, the hollow strut's thickness increases faster than the walls with increasing input linear energy (LE; Fig. 11b). The example could be the set of the process parameters LP = 325 W, LS = 1100 mm/s Ein = 0.295 J/mm and the strut diameter d = 0.8 mm; due to the speed distortion on circular trajectory, the LE is distributed from $E_{in,1}$ = 0.535 J/mm to $E_{in,2}$ = 0.204 J/mm depend on the position.

$$v_1 = \frac{v_0 \bullet (d_0 - TH)}{d_0} = v_0 \bullet \frac{d_1}{d_0} \tag{6}$$

$$v_2 = \frac{v_0 \bullet (d + TH)}{d} = v_0 \bullet \frac{d_2}{d_0} \tag{7}$$

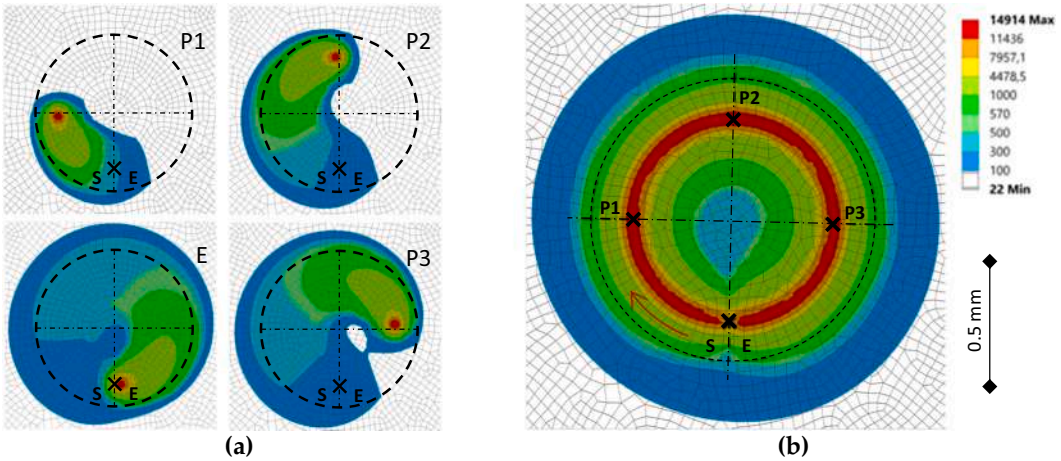

Fig. 21. (a) Laser heat affection of vertical strut geometry in four points of laser trajectory; (b) heat affection of whole strut.

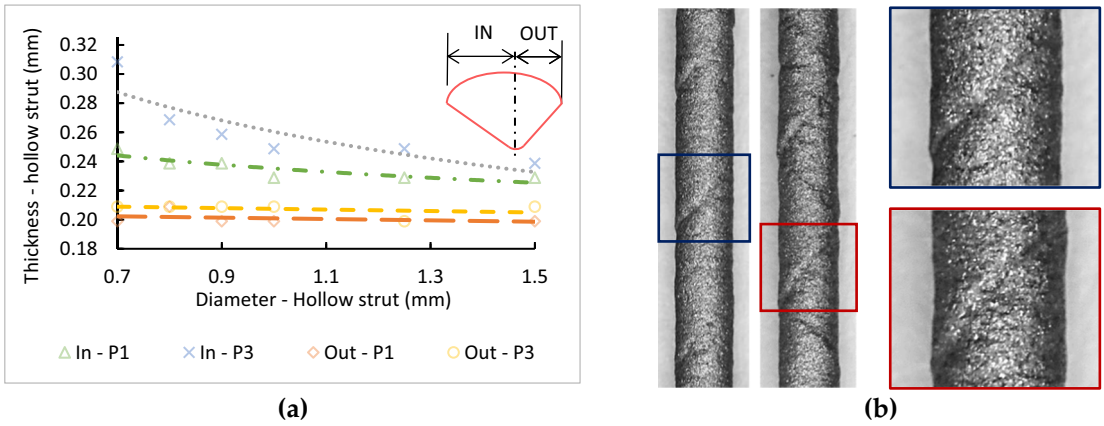

Fig. 22. (a) Strut thickness of the vertical struts with different strut diameter in three points of trajectory based on simulation; (b) spiral groove on surface of vertical struts.

$$E_{in,1} = \frac{P}{v_1} \tag{8}$$

$$E_{in,2} = \frac{P}{v_2} \tag{9}$$

The hypothesis was verified using the vertical struts' transient thermal simulation (d = 0.8 mm) in Ansys Workbench software. The described phenomenon is associated with the strut diameter (Fig. 22a), input linear energy (Fig. 11c,d) and also the position on the laser trajectory (Fig. 21a,b). Close to the starting point (S), the laser started exposition and the melt pool is the narrowest. In the middle of the trajectory (point P2, P3), the track thickness (HT) is growing as the melt pool is larger and longer. In the last part of the trajectory, the melt pool meets the pre-heated area of the powder (around 300 °C) and includes the biggest amount of melted material; the HT is the largest.

The magnifying of the melt pool is also visible on the strut surface where the spiral groove was formed (Fig. 22b). The groove is caused by the deviation of the HT parameter in the start/end point and the spiral shape was created due to moving of this point in each layer by 67° (default setup in post-processing software). Also, the asymmetricity of the HT was observed especially in the centre of strut as was described above (Fig. 20).

Obtained results supported the hypothesis because the values of the LE and d dependence have the same trend as the numerical results. This phenomenon also affected the possibility of the small strut production The smallest struts to produce are those with the diameter d = 0.6 mm.

4.1.2. Overlap parameter and inter-weld porosity

The overlap (OL) is one of the key parameters that contribute for SLM manufacturing process stabilisation. The OL parameter defines the overlapping and connection of the neighbouring track welds. If the OL parameter is too high, the gas porosity occurs by vaporising the AlSi10Mg chemical components. Otherwise, if the OL parameter is too low, the lack of fusion porosity occurs because the gap between neighbouring track is filled by unmelted powder. Therefore, the inter-weld porosity was chosen as the main response parameter during OL optimisation and the aim was to minimise it.

The results showed that the minimum porosity value was achieved in the OL range of 30–40% of the hollow strut thickness (HT; Fig. 13b). According to the further results of the volumetric porosity, the optimal OL value of 35% was finally found. The reason was the lack of fusion porosity which was observed in the inclined strut. After modifying the OL parameter, this issue disappeared (Fig. 15a).

4.1.3. Design of the contour strategy parameters

The main design parameter for minimising the lattice structure imperfections is the hollow strut thickness (HT) that depending on the required strut's diameter, structure topology and the input linear energy (LE). The necessary condition is the constant overlap of 35% (OL) in the whole strut cross-section; therefore, the combination of the strut diameter and compatible HT parameter must be chosen to achieve the integer number of the laser contour even in the strut's centre. Otherwise, two typical issues appear. If the OL parameter is higher than 35%, the remelting of the material and gas porosity occurs in the strut centre. If the strut is unmelted in the centre (negative value of OL), the lack of fusion porosity occurs (Fig. 17b,c). Both issues significantly decrease the

Table 7
Different setup of contour strategy for inclined strut with a diameter of 1.25 mm; three sets of process parameters.

State	Optimal	Remelted	Unmelted
D_{nom} (mm)	1.25	1.25	1.25
LP (W)	350	275	300
LS (mm/s)	1100	800	800
LE (J/mm)	0.32	0.34	0.38
TH (μm)	354	272	392
OL $_{in\ centre}$ (%)	+36.5	+48.8	-11.3
	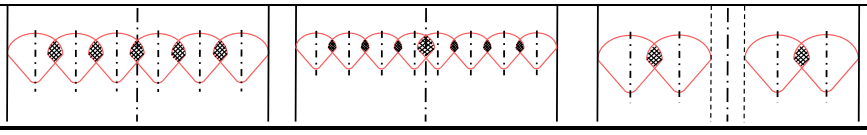		

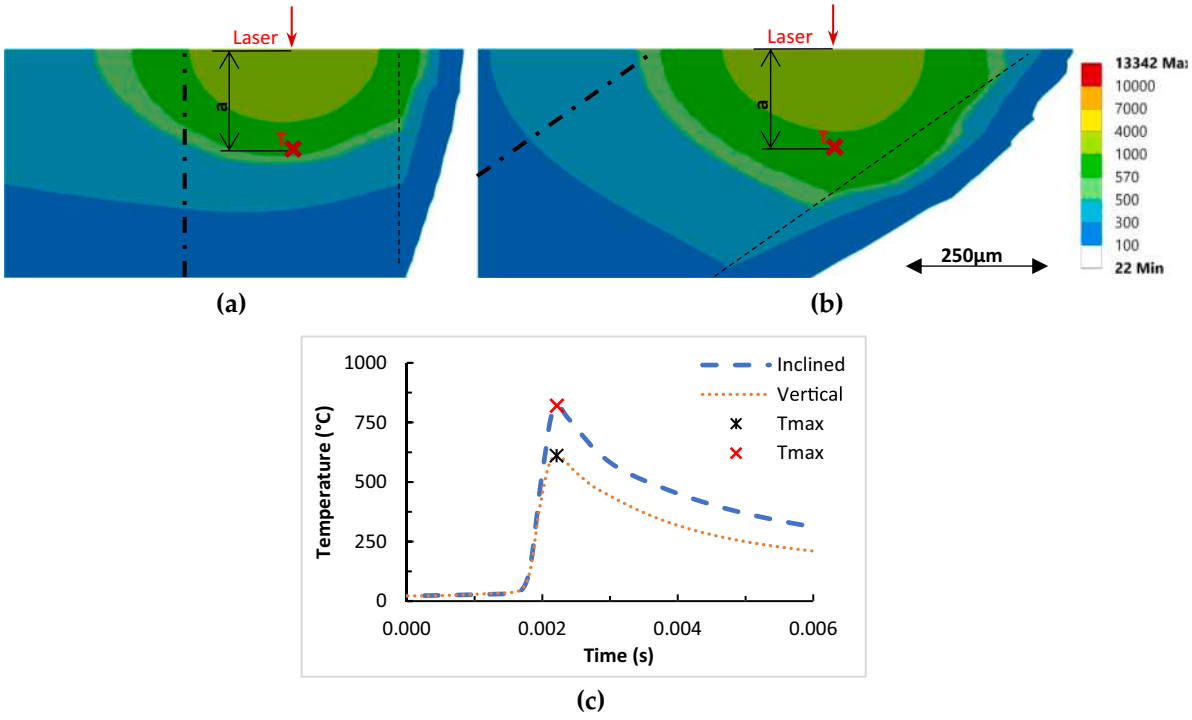

Fig. 23. The numerical simulation of the thermal distribution during powder melting (a) vertical strut; (b) inclined strut; (c) The chart of the temperature T in the distance a below laser exposing point in vertical and inclined strut (d = 0.4 mm).

mechanical properties of the lattice structures.

The results of the HT parameters were analysed using Response Surface Analysis (RSA). It allows finding a smooth approximation of the HT results in the whole perspective SLM process window, definition of their equations (Eqs. (3), (4)), and finally describe the dependence of LE-d-TH parameters for both perpendicular and inclined struts. These predictions make it possible to effectively find the optimal parameters depending on the produced strut diameter (0.6 - 3 mm), input energy (LE 0.25–0.38 J/mm) and orientation. Using the specific values of the HT parameter for each combination of the SLM process parameters and strut diameter enables to obtain the best possible quality of produced lattice structures and implement all previous results into the CS (Table 7).

4.2. The higher level of porosity and surface roughness in inclined struts

The SLM process is based on the selective melting of the metal powder by a high-power laser. The layer-by-layer production causes a cyclic thermal loading of the manufactured part that must be dissipated from the melting point through the component. The crucial moment of the SLM process is the melting of the powder. During the solidification of a liquid phase, the material microstructure is created. If the temperature is too high or low in the met pool, the internal porosity is formed. However, the situation is different in the inclined and vertical struts due to their orientation.

During the vertical struts production, the laser points in the direction of the strut's axis, and there is the volumetric material below the melt pool. Surrounding powder material is not significantly influenced by thermal energy (Fig. 23a). Another situation is in the case of the inclined strut. The laser does not point in the direction of the axis but in the *Z*-direction. This causes the root of the melt pool also points in the Z- direction and thermally influence the down-skin area of the strut where high surface roughness is formed (Fig. 23b). The surrounding powder has low thermal conductivity therefore, it prevents heat dissipation to the surroundings. Thermal energy is longer trapped in the melt pool and then dissipated to the volumetric material with higher thermal conductivity. It follows that the down-skin area of the strut is more thermally influenced than the up-skin area of the strut. Moreover, due to layer-by-layer production, this situation is repeated many times and the changes of microstructures, and material porosity occur [12].

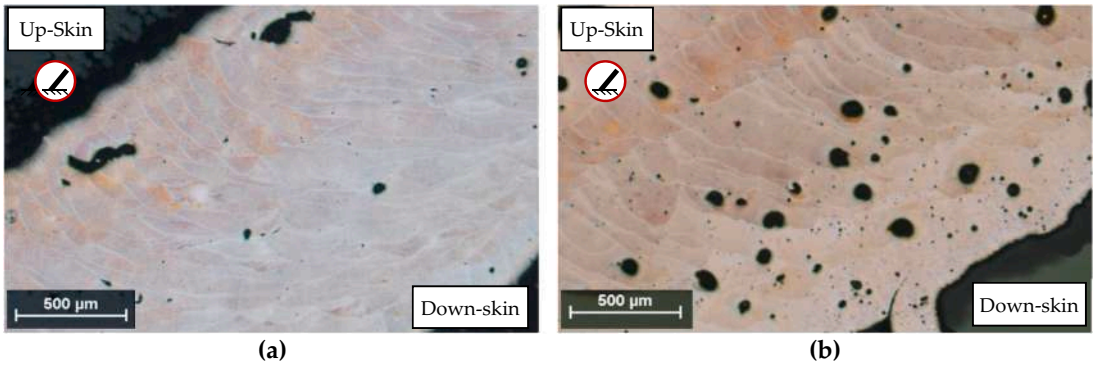

Fig. 24. Microstructure of the struts [16] (a) LP 250 W, LS 1400 mm/s, Ein 0.18 J/mm; (b) LP 300 W, LS 500 mm/s, Ein 0.6 J/mm.

The porosity results in Fig. 15 confirmed this hypothesis. In Fig. 15a, there are many small gas pores placed in the down-skin area even the lack of fusion porosity has appeared in the up-skin area. As was explained above, the down-skin area is repeatedly remelted; therefore, the negative effect of low input energy disappeared and is observable only in the up-skin area. A similar situation is presented in metallographic cross-sections of the previous study [16]. Even the strut was produced by the process parameter out of the recommended process window, the metallographic pores are placed in the down-skin area especially when the high input energy is used (Fig. 24b). In the up-skin area, the lack of fusion porosity appears as was expected (Fig. 24a).

4.3. Influence of contour strategy on mechanical properties

As described above, the contour laser strategy has a positive effect on reducing porosity, surface roughness, and dimensional accuracy. These imperfections mainly cause the initialization of cracks during the mechanical loading of produced parts. Especially, porosity situated near the surface is very susceptible to the initialization of crack. In the case of lattice structure with struts diameter of 0.5–3 mm, the porosity highly affects the strut's cross-section and has a high impact on mechanical properties [9,12,27]. Surface roughness has a similar effect as subsurface porosity. A highly rough surface can cause crack initiation, especially in the bottom area of the inclined strut [14,15]. Dimensional accuracy can affect the mechanical properties of lattice structures because produced struts do not reach the designed dimension (Fig. 18). The designed part could have a different mechanical property than were expected.

However, the microstructure can also be affected by scanning strategy and process parameters [37,38]. The scanning strategy can affect the mechanical properties of produced parts due to grain structure and orientation. Simultaneously, the energy of input parameters has an impact on microstructure. The contour strategy allows the setup of process parameters with different input energy. The contour strategy effect on lattice structures material microstructure and mechanical properties should be further explored.

5. Conclusions

The complex study about manufacturing of the SLM lattice structures was conducted to investigate the influence of the contour laser strategy (CS) on the material porosity, surface roughness, and dimensional accuracy of the lattice structures. Based on the investigation, the following conclusions can be listed below:

- The strong dependence of single-track welds parameters was observed on the specific geometry of the samples; therefore, it is necessary to use the results of the hollow struts thickness (HT) to design the CS parameters.
- The hollow struts thickness (HT) is a variable parameter that depends on the lattice structure's geometry, i.e., orientation and diameter of the struts, and the input linear energy (LE). The equations (Eqs. (3), (4)) were found that consider the relationship between the parameters.
- The overlap parameter of OL = 35% was evaluated for AlSi10Mg material as optimal to achieve the material porosity's best results for two struts orientations (vertical; inclined 35.26°). The constant OL must be reached in the whole volume of the struts, especially in the centre of the struts.
- The inside-out contour strategy significantly reduced the sharp pores caused by the lack of powder effect in the struts' centre.
- Using the found equations (Eqs. (3), (4)) of the hollow struts thickness dependence allows to find the optimal SLM process parameters for the required strut diameter and to minimises the material porosity under the level of 0.2% in the range of d = 0.6–3.0 mm.
- The inclined struts' surface roughness has a linear dependence on the input linear energy, and the values increased with higher energy. The contour strategy approach allows decreasing the surface roughness compared to default parameters. The maximum obtained values were Ra up to 16 μm for vertical struts and up to 80 μm for inclined struts.
- The contour strategy improves the diameter accuracy and the median value of dimensional deviations of 0.03 mm was reached for inclined struts and 0.04 mm for vertical struts.

Declaration of competing interest

The authors declare that they have no known competing financial interests or personal relationships that could have appeared to influence the work reported in this paper.

Acknowledgement

This work is a result of the research project Architectured materials designed for additive manufacturing (ArMAdit) CZ.02.1.01/0.0/0.0/16_025/0007304, specific research project FSI-S-20-6296, the project CEITEC 2020 (LQ1601) with financial support from the Ministry of Education, Youth and Sports of the Czech Republic under the National Sustainability Programme II and CzechNanoLab Research Infrastructure supported by MEYS CR (LM2018110).

References

[1] Vrána R, Koutný D, Paloušek D, Zikmund T. Impact resistance of lattice structure made by selective laser melting from AlSi12 alloy. MM Science Journal 2015: 852–5. https://doi.org/10.17973/MMSJ.2015_12_201547.
[2] Meng G, Ji B, Han H, Gu C, Lin R, Peng F. Design and simulation of an innovative cylinder fabricated by selective laser melting. Chinese Journal of Aeronautics 2019; 32(1):133–42. https://doi.org/10.1016/j.cja.2018.10.011.
[3] Stolt R, Elgh F. Introducing design for selective laser melting in aerospace industry. Journal of Computational Design and Engineering 2020;7(4):489–97. https://doi.org/10.1093/jcde/qwaa042.
[4] Strecker Z, Kubik M, Vitek P, Roupec J, Paloušek D, Šreibr V. Structured magnetic circuit for magnetorheological damper made by selective laser melting technology. Smart Materials and Structures 2019;28. https://doi.org/10.1088/1361-665X/ab0b8e.
[5] Maamoun AH, Xue YF, Elbestawi MA, Veldhuis SC. Effect of selective laser melting process parameters on the quality of al alloy parts: powder characterization, density, surface roughness, and dimensional accuracy. Materials 2018;11. https://doi.org/10.3390/ma11122343.
[6] Galy C, Le Guen E, Lacoste E, Arvieu C. Main defects observed in aluminum alloy parts produced by SLM: from causes to consequences. Additive Manufacturing 2018;22:165–75. https://doi.org/10.1016/j.addma.2018.05.005.
[7] Pauly S, Schricker C, Scudino S, Deng L, Kühn U. Processing a glass-forming zr-based alloy by selective laser melting. Materials and Design 2017;135:133–41. https://doi.org/10.1016/j.matdes.2017.08.070.
[8] Thijs L, Kempen K, Kruth JP, Van Humbeeck J. Fine-structured aluminium products with controllable texture by selective laser melting of pre-alloyed AlSi10Mg powder. Acta Materialia 2013;61:1809–19. https://doi.org/10.1016/j.actamat.2012.11.052.
[9] Kempen K, Thijs L, Van Humbeeck J, Kruth JP. Mechanical properties of AlSi10Mg produced by selective laser melting. Physics Procedia 2012;39:439–46. https://doi.org/10.1016/j.phpro.2012.10.059.
[10] Aboulkhair NT, Everitt NM, Ashcroft I, Tuck C. Reducing porosity in AlSi10Mg parts processed by selective laser melting. Additive Manufacturing 2014;1:77–86. https://doi.org/10.1016/j.addma.2014.08.001.
[11] Dong Z, Zhang X, Shi W, Zhou H, Lei H, Liang J. Study of size effect on microstructure and mechanical properties of AlSi10Mg samples made by selective laser melting. Materials 2018;11. https://doi.org/10.3390/ma11122463.
[12] Delroisse P, Jacques PJ, Maire E, Rigo O, Simar A. Effect of strut orientation on the microstructure heterogeneities in AlSi10Mg lattices processed by selective laser melting. Scripta Materialia 2017;141:32–5. https://doi.org/10.1016/j.scriptamat.2017.07.020.
[13] Liu M, Takata N, Suzuki A, Kobashi M. Microstructural characterization of cellular AlSi10Mg alloy fabricated by selective laser melting. Materials & Design 2018;157: 478–91. https://doi.org/10.1016/j.matdes.2018.08.005.
[14] Han X, Zhu H, Nie X, Wang G, Zeng X. Investigation on selective laser melting AlSi10Mg cellular lattice strut: molten pool morphology, surface roughness and dimensional accuracy. Materials 2018;11. https://doi.org/10.3390/ma11030392.
[15] Tian Y, Tomus D, Rometsch P, Wu X. Influences of processing parameters on surface roughness of hastelloy X produced by selective laser melting. Additive Manufacturing 2017;13:103–12. https://doi.org/10.1016/j.addma.2016.10.010.

[16] Vrána R, Koutný D, Paloušek D, Pantělejev L, Jaroš J, Zikmund T, et al. Selective laser melting strategy for fabrication of thin struts usable in lattice structures. Materials 2018;11. https://doi.org/10.3390/ma11091763.
[17] Vrána R, Červinek O, Mañas P, Koutny D, Paloušek D. Dynamic loading of lattice structure made by selective laser melting-numerical model with substitution of geometrical imperfections. Materials 2018;11. https://doi.org/10.3390/ma11112129.
[18] Vrána R, Koutný D, Paloušek D, Zikmund T. Influence of selective laser melting process parameters on impact resistance of lattice structure made from AlSi10Mg. In: Vol. 1. European Congress and Exhibition on Powder Metallurgy. European PM Conference Proceedings;; 2016. p. 6.
[19] Vrana R, Vaverka O, Koutny D, Docekalova K, Palousek D. Shape and dimensional analysis of lattice structures produced by selective laser melting. MM Science Journal 2020;2020:3938–42. https://doi.org/10.17973/MMSJ.2020_06_2020013.
[20] Großmann A, Gosmann J, Mittelstedt C. Lightweight lattice structures in selective laser melting: design, fabrication and mechanical properties. Materials Science and Engineering: A 2019;766:138356. https://doi.org/10.1016/j.msea.2019.138356.
[21] Aboulkhair NT, Maskery I, Tuck C, Ashcroft I, Everitt NM. On the formation of AlSi10Mg single tracks and layers in selective laser melting: microstructure and nano-mechanical properties. Journal of Materials Processing Technology 2016;230:88–98. https://doi.org/10.1016/j.jmatprotec.2015.11.016.
[22] Yu G, Gu D, Dai D, Xia M, Ma C, Shi Q. On the role of processing parameters in thermal behavior, surface morphology and accuracy during laser 3D printing of aluminum alloy. Journal Of Physics D-Applied Physics 2016;49:135501. https://doi.org/10.1088/0022-3727/49/13/135501.
[23] Zhang J, Song B, Wei Q, Bourell D, Shi Y. A review of selective laser melting of aluminum alloys: Processing, microstructure, property and developing trends. Journal of Materials Science & Technology 2019;35(2):270–84. https://doi.org/10.1016/j.jmst.2018.09.004.
[24] Kempen K, Thijs L, Van Humbeeck J, Kruth J-P. Processing AlSi10Mg by selective laser melting: parameter optimisation and material characterisation. Materials Science and Technology 2015;31(8):917–23. https://doi.org/10.1179/1743284714Y.0000000702.
[25] Pei W, Zhengying W, Zhen C, Junfeng L, Shuzhe Z, Jun D. Numerical simulation and parametric analysis of selective laser melting process of AlSi10Mg powder. Applied Physics A 2017;123:1–15. https://doi.org/10.1007/s00339-017-1143-7.
[26] Louvis E, Fox P, Sutcliffe CJ. Selective laser melting of aluminium components. Journal of Materials Processing Technology 2011;211(2):275–84. https://doi.org/10.1016/j.jmatprotec.2010.09.019.
[27] Qiu C, Yue S, Adkins NJE, Ward M, Hassanin H, Lee PD, et al. Influence of processing conditions on strut structure and compressive properties of cellular lattice structures fabricated by selective laser melting. Materials Science and Engineering: A 2015;628:188–97. https://doi.org/10.1016/j.msea.2015.01.031.
[28] Großmann A, Mölleney J, Frölich T, Merschroth H, Felger J, Weigold M, et al. Dimensionless process development for lattice structure design in laser powder bed fusion. Materials & Design 2020;194:1–16. https://doi.org/10.1016/j.matdes.2020.108952.
[29] Lei H, Li C, Meng J, Zhou H, Liu Y, Zhang X, et al. Evaluation of compressive properties of SLM-fabricated multi-layer lattice structures by experimental test and μ-CT-based finite element analysis. Materials & Design 2019;169:107685. https://doi.org/10.1016/j.matdes.2019.107685.
[30] Li C, Lei H, Zhang Z, Zhang X, Zhou H, Wang P, et al. Architecture design of periodic truss-lattice cells for additive manufacturing. Additive Manufacturing 2020;34:101172. https://doi.org/10.1016/j.addma.2020.101172.
[31] Zikmund T, Šalplachta J, Zatočilová A, Břínek A, Pantělejev L, Štěpánek R, et al. Computed tomography based procedure for reproducible porosity measurement of additive manufactured samples. NDT & E INTERNATIONAL 2019;103:111–8. https://doi.org/10.1016/j.ndteint.2019.02.008.
[32] Letenneur M, Kreitcberg A, Brailovski V. Optimization of laser powder bed fusion processing using a combination of melt pool modeling and design of experiment approaches: density control. Journal of Manufacturing and Materials Processing 2019;3. https://doi.org/10.3390/jmmp3010021.
[33] Liu S, Zhu H, Peng G, Yin J, Zeng X. Microstructure prediction of selective laser melting AlSi10Mg using finite element analysis. Materials & Design 2018;142:319–28. https://doi.org/10.1016/j.matdes.2018.01.022.
[34] Du Y, You X, Qiao F, Guo L, Liu Z. A model for predicting the temperature field during selective laser melting. Results in Physics 2019;12:52–60. https://doi.org/10.1016/j.rinp.2018.11.031.
[35] Metel A, Stebulyanin M, Fedorov S, Okunkova A. Power density distribution for laser additive manufacturing (SLM): potential, fundamentals and advanced applications. Technologies 2019;7. https://doi.org/10.3390/technologies7010005.
[36] Großmann A, Felger J, Frölich T, Gosmann J, Mittelstedt C. Melt pool controlled laser powder bed fusion for customised low-density lattice structures. Materials & Design 2019;181:108054. https://doi.org/10.1016/j.matdes.2019.108054.
[37] Liu X, Zhao C, Zhou X, Shen Z, Liu W. Microstructure of selective laser melted AlSi10Mg alloy. Materials & Design 2019;168:107677. https://doi.org/10.1016/j.matdes.2019.107677.
[38] Wang YC, Lei LM, Shi L, Wan HY, Liang F, Zhang GP. Scanning strategy dependent tensile properties of selective laser melted GH4169. Materials Science and Engineering A 2020;788:139616. https://doi.org/10.1016/j.msea.2020.139616.

micromachines

Article

Influence of Process Energy on the Formation of Imperfections in Body-Centered Cubic Cells with Struts in the Vertical Orientation Produced by Laser Powder Bed Fusion from the Magnesium Alloy WE43

Jan Jaroš [1,*], Ondřej Vaverka [1], Sascha Senck [2] and Daniel Koutný [1,*]

[1] Faculty of Mechanical Engineering, Institute of Machine and Industrial Design, Brno University of Technology, Technicka 2896/2, 616 69 Brno, Czech Republic
[2] Research Group Computed Tomography, University of Applied Sciences Upper Austria, Stelzhamerstraße 23, 4600 Wels, Austria
* Correspondence: jan.jaros2@vut.cz (J.J.); daniel.koutny@vut.cz (D.K.)

Abstract: The low specific density and good strength-to-weight ratio make magnesium alloys a promising material for lightweight applications. The combination of the properties of magnesium alloys and Additive Manufacturing by the Laser Powder Bed Fusion (LPBF) process enables the production of complex geometries such as lattice or bionic structures. Magnesium structures are intended to drastically reduce the weight of components and enable a reduction in fuel consumption, particularly in the aerospace and automotive industries. However, the LPBF processing of magnesium structures is a challenge. In order to produce high-quality structures, the process parameters must be developed in such a way that imperfections such as porosity, high surface roughness and dimensional inaccuracy are suppressed. In this study, the contour scanning strategy is used to produce vertical and inclined struts with diameters ranging from 0.5 to 3 mm. The combination of process parameters such as laser power, laser speed and overlap depend on the inclination and diameter of the strut. The process parameters with an area energy of 1.15–1.46 J/mm^2 for struts with a diameter of 0.5 mm and an area energy of 1.62–3.69 J/mm^2 for diameters of 1, 2 and 3 mm achieve a relative material density of 99.2 to 99.6%, measured on the metallographic sections. The results are verified by CT analyses of BCCZ cells, which achieve a relative material density of over 99.3%. The influence of the process parameters on the quality of struts is described and discussed.

Keywords: laser powder bed fusion; magnesium alloy WE43; scanning strategy; lattice structure; relative density

Citation: Jaroš, J.; Vaverka, O.; Senck, S.; Koutný, D. Influence of Process Energy on the Formation of Imperfections in Body-Centered Cubic Cells with Struts in the Vertical Orientation Produced by Laser Powder Bed Fusion from the Magnesium Alloy WE43. *Micromachines* **2024**, *15*, 278. https://doi.org/10.3390/mi15020278

Academic Editors: Chanho Lee and Sumit Suresh

Received: 15 January 2024
Revised: 8 February 2024
Accepted: 13 February 2024
Published: 15 February 2024

1. Introduction

Laser powder bed fusion (LPBF) [1] is a method of additive processing of metal alloys, which is based on the principle of melting the powder particles layer by layer with a high-power laser. This enables the production of components with complex geometries from a variety of materials such as aluminum and titanium [2]. The development of materials for specific applications also takes place at LPBF, particularly in the field of alloys, which offer new possibilities [3,4].

One of these alloys is magnesium alloys, which have a low specific density and a good strength-to-weight ratio [5]. These properties are crucial for the use of magnesium alloys in the aerospace and automotive industries to reduce weight and improve fuel efficiency [6,7]. In addition, complex geometries such as lattice and bionic structures produced from magnesium alloys can enhance weight reduction [8,9]. Magnesium alloys such as WE43 are also biocompatible and biodegradable [10,11], making them suitable for biomedical applications such as implants due to their mechanical properties that are close to those of human bone [3,5,12].

In order to use magnesium alloy structures in industrial or medical applications, the imperfections associated with their manufacture must be minimized [13,14]. When manufacturing parts by LPBF, the thermal energy generated by the melting of the powder particles must be dissipated through the solid material in the preceding layers, as the surrounding powder has a lower thermal conductivity. Small volumes of material as lattice structures cannot dissipate the thermal energy quickly enough [15]. Therefore, the thermal energy is accumulated in the material [16] and causes the material to overheat, leading to the occurrence of imperfections such as porosity, high surface roughness and dimensional inaccuracy [17,18]. In order to minimize the occurrence of imperfections, process parameters must be used that lead to sufficient melting of the material and, at the same time, to sufficient dissipation of thermal energy [19,20].

The production of magnesium alloy lattice structures using LPBF technology is a particular challenge due to the narrow range of melting (650 °C) and boiling temperatures (1107 °C) [21]. The volume energy of process parameters of more than 214 J/mm^3 (area energy of 8.56 J/mm^2) leads to the vaporization of Mg in the magnesium alloy AZ61D [22]. The vaporization of alloying elements should also lead to a reduction in their mass ratio in alloys [23]. High energy input leads to an expansion of meltpool, which blasts away the surrounding powder. In contrast, cooling of the material reduces the volume and leads to the formation of pores due to the absence of powder particles [21]. Vapors also defocus the laser beam, which affects the quality of the manufactured parts [24]. Vaporization of the material can be prevented by using process parameters with lower thermal impact on the meltpool, which reduces the formation of vapors [22].

The processing of magnesium alloys should be divided into three stages depending on the energy of the process parameters [22,25]. As already mentioned, high-input energy leads to vaporization of the alloying elements. Low input energy may not always guarantee a sufficient temperature for melting the powder. Therefore, there is insufficient bonding between the molten material, resulting in low relative material density and poor mechanical properties [25]. Sufficient energy input leads to a reduction in the viscosity of the meltpool, which improves the effectiveness of the process [26,27]. The meltpool is stable, resulting in sufficient bonding between neighboring welds, which is necessary for the production of components with high relative material density and good mechanical properties. Hyer et al. [28] developed the process parameters for bulk samples of magnesium alloy WE43, leading to a high relative material density of 99.7%, i.e., laser power 200 W, scanning speed 1100 mm/s, hatch distance 0.13 mm, and layer thickness 0.04 mm.

For the production of small series components in the form of lattice structures, not only must process parameters be developed, but a specific scanning strategy should also be used [29]. The meander scanning strategy, which is mainly used for bulk samples, leads to the formation of porosity in the subsurface area due to the deceleration of the laser at the end of the trajectories [30]. The meander strategy also leads to high porosity in small-volume samples, as the trajectories of the laser cause the meltpool to overheat [20]. The contour scanning strategy is more efficient for lattice structures. Concentric welding trajectories allow for an effective energy distribution over the entire diameter of the strut. In addition, the contour scanning strategy has been successfully used to produce high-relative-material-density lattice structures [20].

Thus, the effective production of magnesium alloy lattice structures with minimal defects depends on the process parameters, scanning strategy, strut diameter and inclination. In this study, the production of vertical struts and inclined struts with an inclination of 35.26°, corresponding to Body-Centered Cubic (BCC) cells, is investigated. The most promising process parameters are evaluated on Body-Centered Cubic cells with struts in the vertical orientation (BCCZ), which are a combination of vertical and inclined struts. The magnesium alloy WE43 is used.

2. Materials and Methods

2.1. Laser Powder Bed Fusion

The samples are produced using the LPBF with the SLM 280HL machine (SLM Solutions Group AG, Lübeck, Germany). The machine is equipped with an ytterbium laser with a spot diameter of 82 µm and Gaussian distribution. A gas-atomized magnesium alloy WE43 (Luxfer MEL Technologies, Manchester, UK) with a particle size distribution of 28–60 µm with an average size of 39.8 µm is used. The chemical composition of the powder is listed in Table 1. Therefore, inert argon gas is used to prevent oxidation of the magnesium alloy during processing. The oxygen concentration is kept below a concentration of 0.1% during production. A laser power of 50–250 W and laser speed of 200–1200 mm/s are used for all experiments. The layer thickness is 50 µm and the temperature of the platform is set to 120 °C.

Table 1. Chemical composition of WE43 powder.

	Mg (wt %)	Y (wt %)	Zr (wt %)	Nd (wt %)	Si (wt %)	Cu (wt %)
WE43 powder	Bal.	3.96	0.56	2.30	<0.01	<0.01

2.2. Contour Scanning Strategy

Based on previous research [20], the contour scanning strategy seems to be suitable for the production of lattice structures. The contour scanning strategy is formed by concentric welds that allow for better control of the input energy into the process, which is particularly important for low-volume samples (Figure 1). The most important parameters of the contour scanning strategy are the laser power and laser speed, which result in weld formations with an exact width. The next important parameter is the overlap of the neighboring welds, which is represented by the hatch distance. The optimal value of these parameters is the key to reducing imperfections in the material of lattice structures. Therefore, four experiments are conducted. The first experiment deals with the influence of the sample geometry and process parameters on the width of the weld. The second experiment deals with the hatch distance of hollow strut specimens formed by two welds. The output parameter of the experiment is the appropriate value of overlap for the production of specimens with high relative material density. Based on the parameters from the first two experiments, the contour scanning strategy is used in the third experiment to produce vertical and inclined struts with an inclination angle of 35.26% corresponding to BCC cell inclination. The last experiment is used to verify the best results of the third experiment. Therefore, the BCCZ cells representing both studied strut orientations are produced with different process parameters for vertical and inclined struts. In addition, three different laser trajectories of the contour strategy are identified in the BCCZ cells, which can influence the quality of the produced sample.

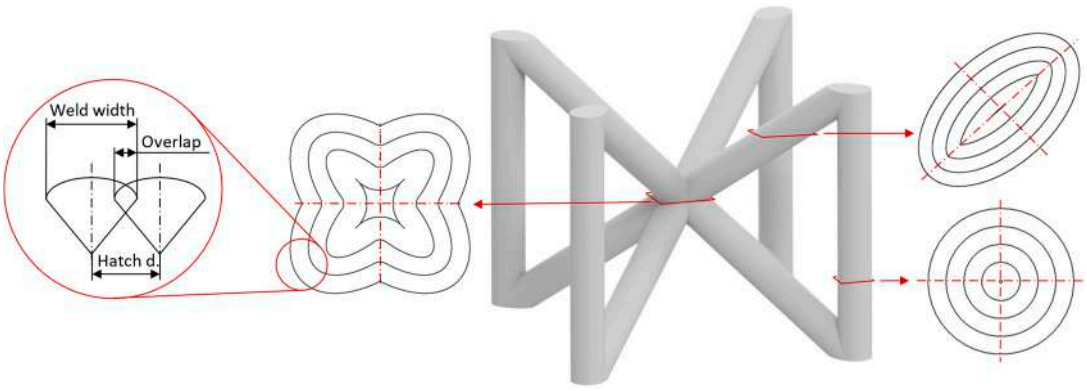

Figure 1. Parameters of contour scanning strategy and three different trajectories in BCCZ cell.

2.3. Weld Width

The weld width depends on the process parameters, i.e., the laser power (LP) and the laser speed (LS) or their combination (Equation (1)), which is referred to as linear energy (LE). The linear energy of the process parameters in these experiments is in the range of 0.05–1.25 J/mm. Basically, the weld width is measured on single-track samples (Figure 2a), but the geometry of a single-track specimen does not correspond to the struts in the lattice structure. Therefore, samples with a thin-walled and hollow strut geometry (Figure 2b) are used to obtain more precise results, which are required for the contour scanning strategy. The weld width is included in the overlap of the neighboring welds (Equation (2)) as it changes with the geometry and diameter of the samples [20].

$$\mathrm{LE} = \frac{\mathrm{LP}}{\mathrm{LS}}\ (\mathrm{J/mm}) \tag{1}$$

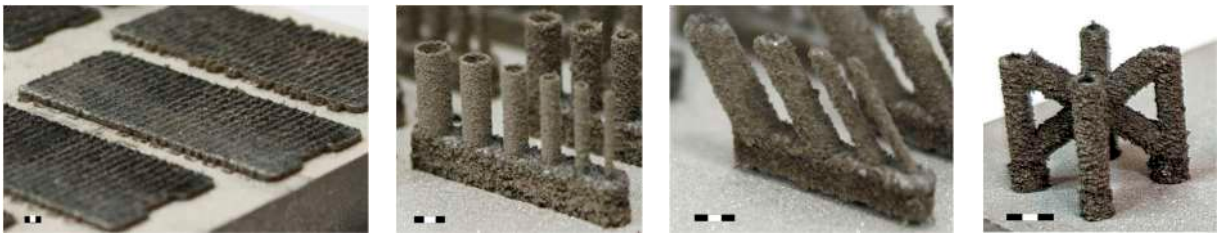

(**a**) (**b**) (**c**) (**d**)

Figure 2. (**a**) Single-weld samples produced on the top of 1 mm thick WE43 material; (**b**) hollow struts; (**c**) inclined struts; (**d**) BCCZ cell (scale 3 mm).

2.3.1. Single-Weld Samples

The width of the weld depends on the combination of laser power, laser speed and, in the case of single tracks, specifically on the substrate material. The weld width is also influenced by preheating the platform. Therefore, the single-track samples are produced on a 1 mm thick WE43 material (Figure 2a), which ensures adequate heat dissipation. The 1 mm thick material is fabricated with process parameters, i.e., laser power of 250 W, laser speed of 450 mm/s and hatch distance of 80 µm, based on the study [31]. The width of each weld is measured on the top images taken with an optical microscope (Olympus SZX7, Olympus, Tokyo, Japan). The width of single welds is the average value calculated from five measurements (Figure 3a).

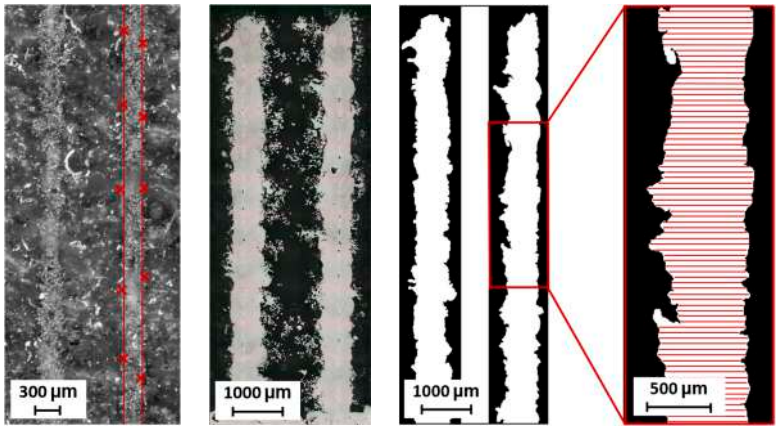

(**a**) (**b**) (**c**)

Figure 3. Measurement of sample width: (**a**) single weld sample; (**b**) metallographic section of hollow strut; (**c**) measurement of hollow strut width.

2.3.2. Thin Wall Samples

However, the geometry of the single-weld samples does not match the geometry of the struts in the lattice structure. Therefore, thin wall specimens are used to investigate the effects of the superposition of single welds. The upper weld partially melts the previous weld, increasing the width of the thin wall. The thin wall width is measured on the metallographic sections in the same way as the hollow strut specimens. The methodology is described below.

2.3.3. Hollow Strut Samples

To obtain the most accurate weld width, the geometry of vertical hollow struts is used, created by a single weld with diameters from 0.5 to 3 mm with a step of 0.5 mm (Figure 2b). The width of hollow struts is influenced by heat dissipation, whereby the heat is mainly dissipated through the material of the specimen. However, due to the small volume of the specimen, the material is heated at higher temperatures, causing more powder particles to melt and increase in volume. Some of the heat is also dissipated through the surrounding powder particles and affects the surface of the samples, where the powder particles are partially melted and adhered.

The width of the thin walls and hollow struts is measured using metallographic sections that have been ground and polished (Figure 3b). The images of the cross-sections were taken with a digital microscope (Keyence VHX-6000, objective Z250R, zoom 250×, Keyence, Mechelen, Belgium). The width is the average value from both sides of the sample measured in each pixel of the image—approximately 8000 values are obtained (Figure 3c).

2.4. Overlap

The overlap of the neighboring weld together with the process parameters determines the energy density in the strut. The overlap (OL) depends on the weld width (WW) and hatch distance (HD) and represents the joint between two welds created by remelting the material (Equation (2), Figure 4). In the case of this study, the overlap is calculated from the width of the hollow struts. Therefore, it changes with the strut diameter. Lower overlap and laser power at a higher laser speed result in lower energy density. Low energy can result in areas of unmelted material being trapped in sharp-edged pores. High energy leads to overheated material, which supports the formation of spherical pores [16]. Therefore, the optimum value of overlap that suppresses pore formation and results in a sufficient bond between adjacent welds should be determined. For this purpose, the geometry of vertical hollow struts with two welds is used (Figure 4a). The hollow struts with two welds (2W) are produced with diameters from 0.5 to 3 mm with a step of 0.5 mm. Three values for laser power (100, 150 and 200 W) and laser speed (400, 600 and 800 mm/s) are chosen to cover the range of selected process parameters. The hatch distances are 0.06, 0.1 and 0.14 mm for each combination of laser power and laser speed, corresponding to an overlap of 20 to 80%. A total of 162 samples are produced. The optimum overlap is determined based on the porosity between two welds in the 2W hollow strut.

$$\mathrm{OL} = \left(\frac{\mathrm{WW} - \mathrm{HD}}{\mathrm{WW}}\right) \cdot 100\ (\%) \tag{2}$$

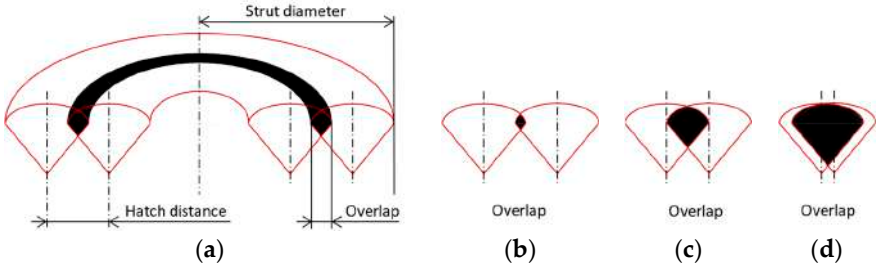

Figure 4. (**a**) Parameters in 2W hollow strut; visualization of overlap: (**b**) 10%; (**c**) 50%; (**d**) 90%.

2.5. Vertical and Inclined Struts

The vertical and inclined (35.26°) struts (Figure 2c) are fabricated to determine the combinations of process parameters, i.e., laser power, laser speed and overlap, that result in high relative material density. Inclination of 35.26° corresponds to BCC cells, which are the worst case of inclination in the cubic crystal system and the most challenging to fabricate using LPBF technology. To categorize the influence of these parameters on the relative material density, the area energy (AE) is used (Equation (3)), where LP is the laser power, LS is the laser speed and HD is the hatch distance calculated according to Equation (2). Surface roughness and diameter deviation are also measured to capture the complex strut geometry. The experiment is designed by DOE with the following boundary conditions: laser power of 50–250 W; laser speed of 200–1000 mm/s, corresponding to a linear energy of 0.08–0.75 J/mm; and strut diameters of 0.5, 1, 2, and 3 mm. The overlap is between 45 and 85%, based on the results of the overlap experiment. These process parameters correspond to an area energy of 0.96–4.37 J/mm^2. The DOE parameters for the vertical struts are 48 cube points, 12 center points in the cube, 48 axis points, and 12 center points in the axis. The inclined struts are designed with half of the DOE setup. A total of 120 vertical and 60 inclined struts are produced.

$$\mathrm{AE} = \frac{\mathrm{LP}}{\mathrm{LS}\cdot\mathrm{HD}}(\mathrm{J/mm^2}) \tag{3}$$

2.6. BCCZ Cells

The BCCZ cells (Figure 2d) are produced to evaluate the best results of the vertical and inclined struts. The BCCZ cell is divided into vertical and inclined struts, which are produced with different process parameters depending on the result. The BCCZ cells are produced in 3 samples for each diameter (0.5, 1, 2 and 3 mm). CT analysis is used to evaluate the relative material density.

2.7. Relative Material Density

2.7.1. Metallographic Sections

Metallographic sections are used for two types of samples, i.e., 2W hollow struts and struts. The samples are metallographically processed and imaged with a Keyence digital microscope. The images are converted into binary monochrome images. Porosity is represented by the percentage of black areas in the sample section. For 2W hollow struts, the porosity is measured between the two adjacent welds according to the design of specimens (Figure 5a,b). The porosity of the struts is measured on metallographic sections (Figure 5c,d). In the contour scanning strategy, the center of the vertical and inclined struts as well as the lower part of the inclined struts is a critical point for porosity formation, as previous research has shown [19,20]. Therefore, the struts are polished towards the center and the relative material density values are used as a relative value for the comparison of the strut porosity.

2.7.2. CT Analysis

Nanofocus X-ray computed tomography (nanoCT, GE phoenix | x-ray Nanotom 180 NF, Waygate technologies, Hürth, Germany) is used to analyze the relative material density in BCCZ cells. The following scanning parameters are used: an X-ray tube voltage of 130 kV, current of 80 µm, integration time of 600, average of 5 images, a total of 1500 projections, and a 0.1 mm copper filter to reduce beam-hardening artefacts. The final isovoxel resolution is 10 µm. Porosity analyses were carried out in VGStudioMax 2023.1 (Volume Graphics), using an ISO50 threshold and a minimum of eight voxels for a segmented pore, which is a typical threshold for the segmentation of pores [32].

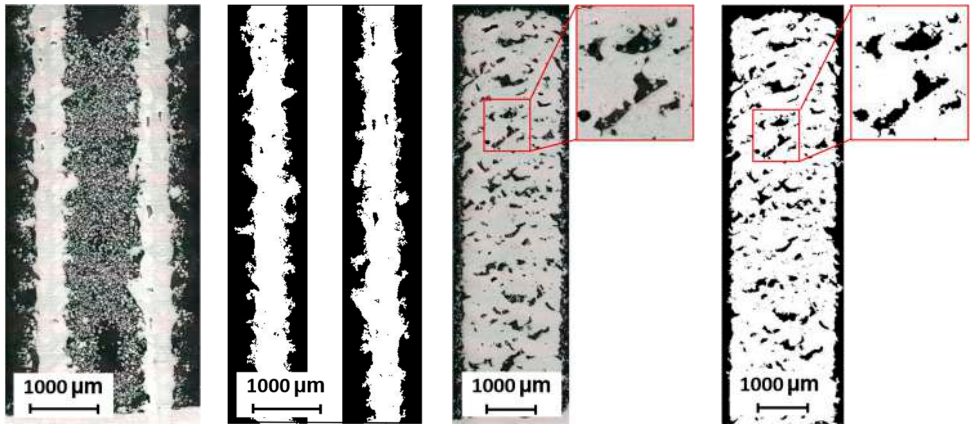

Figure 5. Relative material density measurement of: (**a**) 2W hollow strut; (**b**) 2W hollow strut monochrome image; (**c**) vertical strut with detail of pore; (**d**) vertical strut monochrome image.

2.8. Surface Roughness

The surface roughness of the struts is mainly influenced by partially melted powder particles that adhere to the surface of the specimen. In the case of magnesium alloys, this effect is exacerbated by the low melting temperature. In the case of inclined struts, two effects occur. The first effect is the staircase effect, which is typical for additive manufacturing technologies and is mainly observed on the top side of the inclined samples. The second effect is related to heat dissipation, where heat is mainly transferred through the material towards the platform. The accumulation of heat causes the powder particles to melt and stick to the underside of the specimen. Therefore, the surface roughness Ra is measured on the side of the struts that is not affected by these two effects; moreover, it is also possible to compare the measured values between vertical and inclined struts, which are only affected by the process parameters. The surface roughness Ra is measured with a Keyence digital microscope. The surface of the struts is digitized, and the surface roughness Ra is measured in five lines parallel to the strut axis (Figure 6a). The final surface roughness Ra is the average of five measurements. The measured values are used to compare the influence of the process parameters and the orientation of the struts.

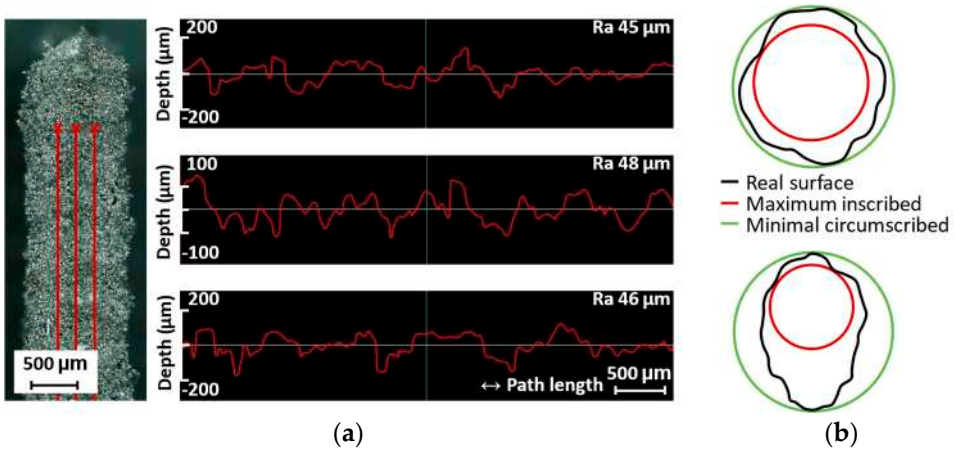

Figure 6. (**a**) Example of measurement of the surface roughness Ra on the side of the strut in three lines; (**b**) measurement of the dimensional deviation by fitting maximum inscribed and minimum circumscribed cylinders.

2.9. Diameter Deviation

The combinations of process parameters lead to different weld widths, which affect the dimensions of the manufactured samples. To evaluate this effect, the center of the

outer laser track is set exactly to the diameter of the strut. Two parameters are measured, namely the maximum inscribed diameter and the minimum circumscribed diameter of the cylinders attached to the digitized struts (Figure 6b). The maximum inscribed cylinder represents the load-bearing diameter of the strut. The minimum circumscribed cylinder represents the amount of material melted on the surface of the struts. Figure 6b shows the differences between vertical and inclined struts, which differ in the lower part of the inclined struts. The diameters are measured with an optical 3D scanner (Atos Triple Scan III, GOM GmbH, Braunschweig, Germany). The scanned data are polygonised and the GOM Inspect software is used to fit the cylinders into the digitized surface of the struts using the best-fit method.

3. Results and Discussion

3.1. Effect of Specimen Geometry on Weld Width

The width of the welds depends on the sample geometry, the process parameters and spot diameter size of the laser source. The width of the single welds, thin walls or hollow struts increases with the linear energy (Figure 7a). At a low linear energy of up to 0.4 J/mm, the widths show the same trend. At a linear energy of more than 0.4 J/mm, the geometry of the specimens leads to an increase in width for thin walls and hollow struts. For single welds, the width remains in a narrow interval between 0.23 and 0.32 mm. The width of all samples shows a dependence on the laser speed and laser power, which is illustrated by the results of the hollow struts in Figure 7b. The larger width is measured at a high laser power and low laser speed, corresponding to the influence of linear energy (Equation (1)). The width of the hollow strut (Figure 7c) also shows a slight dependence on the strut diameter, which is represented by the average values of the mean width.

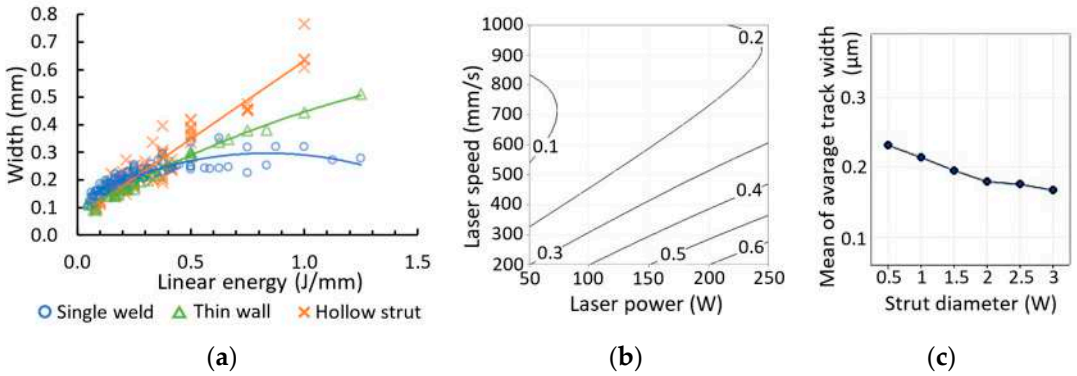

Figure 7. (**a**) Dependence of the width of single welds, thin walls, and hollow struts on linear energy; (**b**) width of hollow struts with a diameter of 1.5 mm based on the laser power and laser speed; (**c**) mean of average width dependent on strut diameter.

In the contour scanning strategy, the weld width is an important parameter that determines the overlap between two concentric welds [29,33]. In many cases, the hatch distance is set as a fixed value and the influence of the process parameters is observed [13]. Therefore, the pores between two welds are formed as a function of the width of the weld. A small weld width leads to insufficient overlap and thus to a lack of fusion pores. A large weld width leads to a large overlap, which is typical for keyhole pores [34,35]. To reduce the formation of pores between two welds, the hatch distance must be different for different linear energies to ensure a constant overlap.

3.2. Overlap

For the 2W hollow struts, the hatch distance, which determines the overlap of welds (Equation (2)), shows a strong dependence on the strut diameter (Figure 8a) and linear energy (Figure 8b). The hatch distance in three batches for a linear energy of 0.25 J/mm shows a similar trend of relative material density in the range of 0.5–3 mm (Figure 8a).

The maximum relative material density is measured at a hatch distance of 0.1 mm, which corresponds to an overlap of 60–68% according to the weld width and Equation (2). The overlap as a function of linear energy for the maximum relative material density for all combinations of process parameters and a diameter of 1 mm is shown in Figure 8b. The plotted values show that a high linear energy requires higher overlap values to achieve a high relative material density between two welds of 2W hollow struts. The overlap values are between 45 and 85% for all diameters; therefore, this range is used for the design of the strut experiment.

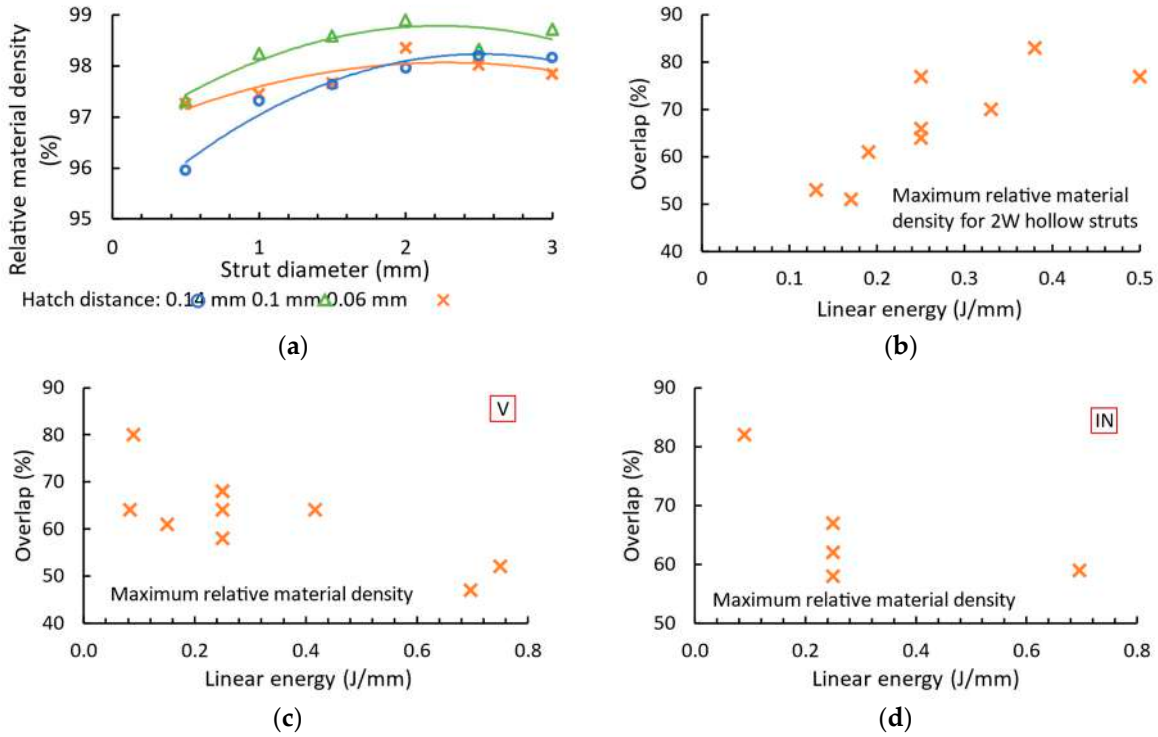

Figure 8. Dependence of (**a**) relative material density of 2W hollow strut on strut diameter for three batches of hatch distance produced with a laser power of 200W and laser speed of 800 mm/s; overlap on linear energy for the maximum measured relative material density of samples with diameter of 1 mm for (**b**) 2W hollow struts, (**c**) vertical struts, and (**d**) inclined struts.

For the vertical and inclined struts with a diameter of 1 mm (Figure 8c,d), the dependence of the overlap for the maximum relative material density on the linear energy shows an increasing trend. An overlap of more than 80% leads to a relative material density of more than 99.3% for both vertical and inclined struts produced with a linear energy of less than 0.1 J/mm. An overlap of less than 60% results in a relative material density of over 98.4% at a linear energy of over 0.6 J/mm.

The overlap is the key parameter for the contour scanning strategy that influences the formation of pores between the welds [15,22]. The geometry of the samples influences the overlap required to obtain a high relative material density. The low-volume 2W hollow struts show an opposite trend than vertical and inclined struts (Figure 8b–d). A low linear energy of 2W hollow struts leads to a small weld width, which requires a smaller overlap. High energy leads to the opposite situation. This phenomenon can be related to heat dissipation when the material volume is able to dissipate a certain amount of heat [15].

In the case of the struts, the low linear energy requires a higher overlap in order to melt the material completely. For the high linear energy, a lower overlap is required. This is probably due to heat dissipation through the material of the entire strut [16]. The three situations occur for struts with a diameter of 2 mm (Table 2) based on the area considering the overlap (Equation (3)). The insufficient area energy of 1.34 J/mm^2 for vertical strut (V)

and 1.57 J/mm^2 for inclined strut (IN) leads to irregular pores. The circular pores occur in the struts with an area energy of 3.99 (V) and 2.88 J/mm^2 (IN). Area energies of 3.26 (V) and 2.46 J/mm^2 (IN) lead to a high relative material density.

Table 2. Comparison of the area energies of process parameters on vertical and inclined struts with a diameter of 2 mm.

LP (W)	250	50	150	221	79	79
LS (mm/s)	600	600	600	883	883	317
AE (J/mm^2)	3.99	1.34	3.26	2.88	1.57	2.46
OL (%)	71	41	67	76	78	69
Vertical struts / Inclined struts	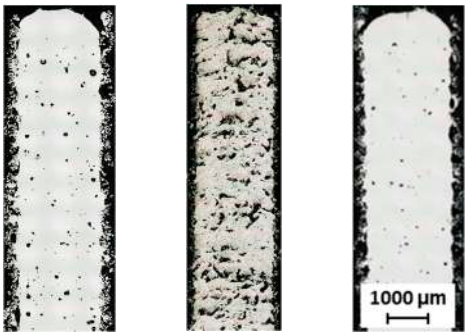			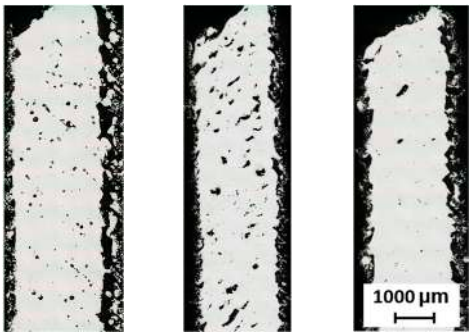		
RD (%)	97.9	86.7	99.2	97.9	95.9	99.2

LP is laser power (W); LS is laser speed (mm/s); AE is area energy (J/mm^2); OL is overlap (%); RD is relative material density (%); vertical and inclined orientation of struts.

3.3. Relative Material Density

The area energy (Equation (3)) is used to describe the effects of laser power, laser speed and overlap on the relative material density in the struts (Figure 9). The relative material density of the vertical struts (Figure 9a) increases with the area energy. An area energy of up to 2.6 J/mm^2 leads to a relative material density of less than 95% for some of the vertical struts with a diameter of 1, 2 and 3 mm. In contrast, struts with a diameter of 0.5 mm are produced with a relative material density of over 97.6%. The area energy of over 2.6 J/mm^2 leads to a relative material density of over 96.4% for diameters of 1, 2 and 3 mm. In the case of diameters of 0.5 mm, the relative material density is less than 95%. The relative material density of the inclined struts (Figure 9b) shows no clear dependency. The area energy of up to 2 J/mm^2 appears to be promising for struts with a diameter of 0.5 mm. An area energy of more than 2 J/mm^2 is more suitable for struts with a diameter of 2 mm.

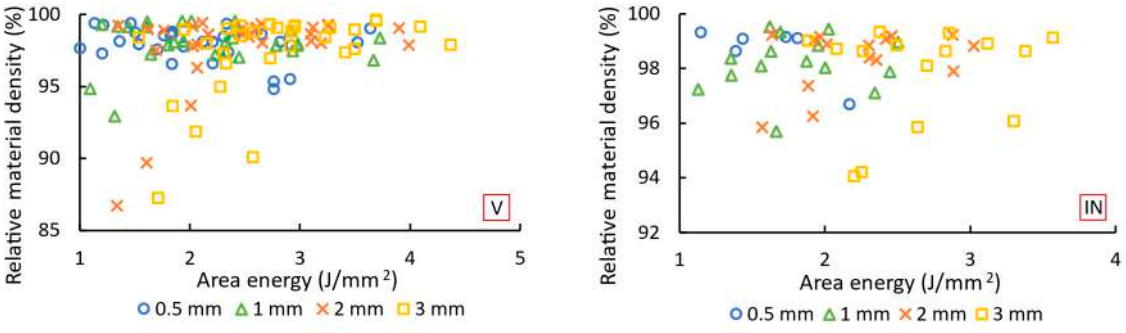

(**a**) (**b**)

Figure 9. Relative material density depending on area energy for (**a**) vertical and (**b**) inclined struts with diameters of 0.5, 1, 2, and 3 mm.

The best results are shown in Table 3. The vertical and inclined struts achieved a relative material density of 99.2–99.6%. The optimal process parameters depend on the

strut diameter. The inclination of the strut only affects the overlap. The vertical struts achieved a high relative material density with a higher area energy than the inclined struts (21–36% higher area energy). For the struts with a diameter of 0.5 mm, the area energy of 1.15–1.46 J/mm^2 leads to a relative material density of over 99.3%. The struts with diameters of 1 mm, 2 mm and 3 mm achieve a relative material density of over 99.2% at an area energy of 1.62–3.69 J/mm^2. The struts with diameters of 0.5 and 1 mm have small circular pores. The struts with diameters of 2 and 3 mm contain larger pores with an irregular shape.

Table 3. The best results obtained from the strut experiment.

LP (W)	79		79		79		150	
LS (mm/s)	883		317		317		600	
AE (J/mm^2)	1.46	1.15	2.41	1.62	2.12	1.64	3.69	2.38
D (mm)	0.5		1		2		3	
OL (%)	75	75	64	58	54	54	69	64
Orient.	V	IN	V	IN	V	IN	V	IN
								
RD (%)	99.4	99.3	99.6	99.5	99.4	99.2	99.6	99.3

The amount of area energy required to produce struts with a high relative material density depends on the diameter of the struts. The diameter of the struts influences the heat dissipation rate [15,16]. With a diameter of 3 mm, the heat dissipation rate is higher, which requires a higher area energy. For struts with diameters of 2 and 3 mm, the higher heat dissipation rate also leads to irregular pores in some parts of the strut. This type of pore is typical of insufficient energy [36].

For the production of BCCZ cells, the process parameters that lead to the best results in terms of relative material density are used. The CT scans are shown in Table 4. BCCZ cells with a diameter of 0.5 contain small spherical pores and an average relative material density of 99.96%. The BCCZ with a diameter of 1 mm achieves an average relative material density of 99.83% with a maximum pore volume of 0.011 mm^3. BCCZ cells with diameters of 2 and 3 mm have irregular pores with a volume of more than 0.04 mm^3.

In the BCCZ cells with a diameter of 2 mm, irregular pores appear between the welds (Figure 10a), which are typical for low energy. The low energy of the process parameters means that only part of the material is melted, leaving unmelted areas between the tracks in which unmelted particles are trapped [19]. The BCCZ cells (Figure 10b) with a diameter of 3 mm have irregular pores with a volume of more than 0.05 mm^3 in the inclined struts, but the node of the cell is without large pores. This could be due to the laser trajectories, which are different for the cell node than for the struts (Figure 1). Due to the sharp edges in the center, the material is heated at a higher temperature, which supports the melting of the powder particles [35]. Vertical struts of 3 mm BCCZ cells showed deformations (holes) on the surface that go through the material of the struts and are not recognized as pores by the CT scan (Figure 10b).

Table 4. CT scans of BCCZ cells.

D (mm)	0.5	1	2	3
	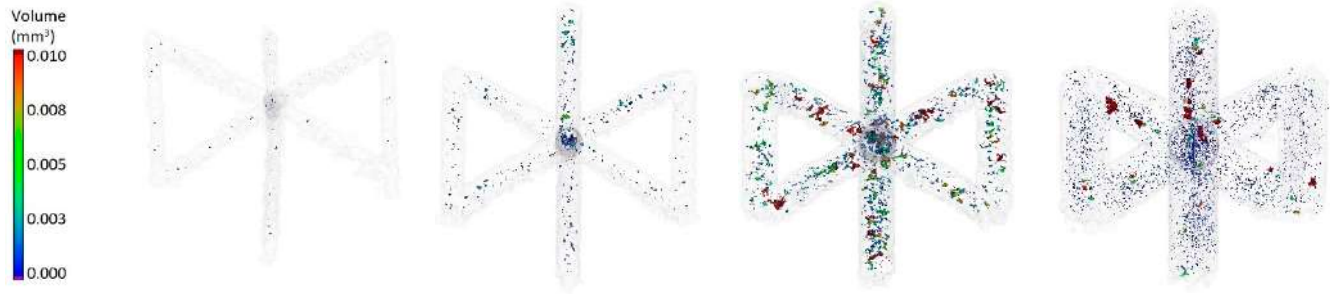			
RD (%)	99.96	99.83	99.32	99.72

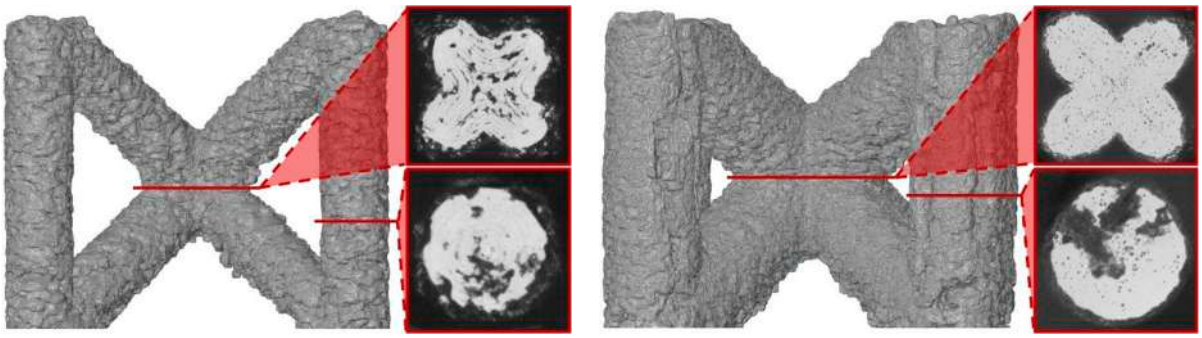

(**a**) (**b**)

Figure 10. Polygonised surface of BCCZ cells and images of cross-sections of node and strut for diameters of (**a**,**b**).

These holes (Figure 11a–c) are related to the contour scanning strategy and are generated at the beginning on the outer laser trajectory [20]. These phenomena occur in the vertical struts with area energies of 2.3 J/mm^2 for the vertical strut and 3.69 J/mm^2 for the vertical strut of BCCZ cells, and a strut diameter of 3 mm. Therefore, the holes can be caused by LPBF melting of the powder particles in the contour strategy. The powder particles are drawn into the meltpool during melting [37], which is also favored by the low melting temperature of the magnesium alloy [21]. At the beginning of the outer laser trajectory, the meltpool draws all surrounded particles, resulting in the powder particles not forming a sufficient bond at the end of the laser trajectory. These holes can significantly affect the load-bearing part of the struts and serve as an initiator of crack during loading [38].

(**a**) (**b**) (**c**) (**d**)

Figure 11. The holes on the surface of (**a**) vertical strut; (**b**) polygonised vertical strut; (**c**) BCCZ cell; (**d**) polygonised BCCZ cell (scale 3 mm).

3.4. Surface Roughness

The surface roughness Ra measured on the side of the struts is shown in Figure 12. Vertical (Figure 12a) and inclined (Figure 12b) struts are mainly influenced by the linear energy (laser power and laser speed), and the overlap parameters have no influence on the surface roughness. For vertical struts, the best results are measured at a linear energy of 0.08 J/mm, with a surface roughness Ra in the range of 30–42 µm. Inclined struts achieve an Ra of 42–50 µm at a linear energy of 0.09 J/mm (diameter of 0.5 mm) and a linear energy of 0.25 J/mm (diameter of 1, 2, 3 mm). A high linear energy (0.7 J/mm) leads to a surface roughness Ra of 48–64 µm for vertical struts and 51–62 µm for inclined struts.

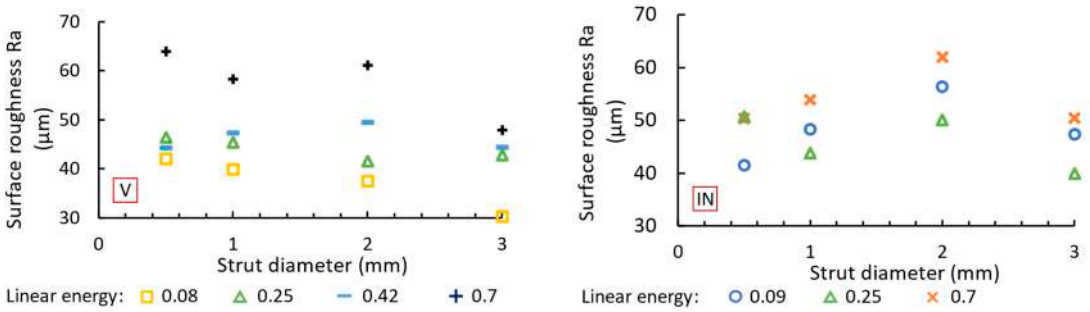

Figure 12. Surface roughness Ra for (**a**) vertical and (**b**) inclined struts.

The high surface roughness Ra is related to the low melting point of the magnesium alloy [21]. The heat from the meltpool is primarily dissipated via the material of the strut, but the small volume of the strut leads to overheating of the material. Therefore, part of the heat is dissipated via the surrounding powder particles, which have a lower heat dissipation rate [16]. The powder particles are partially melted and bonded to the surface, leading to an increase in the surface roughness Ra.

3.5. Diameters of Vertical and Inclined Struts

The diameter deviations of the produced struts from the nominal diameters are listed in Figure 13, based on the maximum inscribed and minimum circumscribed cylinders. The maximum inscribed cylinder, which represents the load-bearing cross-section of the strut [39], reaches a larger diameter than required for both vertical (Figure 13a) and inclined (Figure 13b) struts. The deviation from the diameter increases with the linear energy and strut diameter. For vertical struts, a linear energy of 0.08 J/mm leads to a diameter deviation in the range of 0.12–0.15 mm. A linear energy of 0.7 J/mm leads to a diameter deviation of 0.22–0.46 mm. Inclined struts achieve a diameter deviation of 0.12–0.24 mm with a linear energy of 0.09 J/mm and 0.12–0.44 mm with a linear energy of 0.7 J/mm.

The minimum circumscribed cylinder means an increase in the strut diameter due to the high energy of the process parameters, which leads to the melting of more powder particles [20]. In addition, the partially melted powder particles are bound to the surface of the strut. With the inclined struts (Figure 13d), there is a lot of material on the underside as the heat is dissipated towards the platform. The deviation increases with the linear energy and strut diameter. Vertical struts (Figure 13c) show a minimum deviation of 0.52–0.68 mm at a linear energy of 0.08 J/mm and a maximum deviation of 1.07–1.93 mm at a linear energy of 0.7 J/mm. The inclined struts achieve a deviation of 0.8–1.79 mm (diameter of 0.5 mm) and 0.92–2.19 mm (diameter of 3 mm). The maximum diameter increases by 358% with a diameter of 0.5 mm and linear energy of 0.7 J/mm.

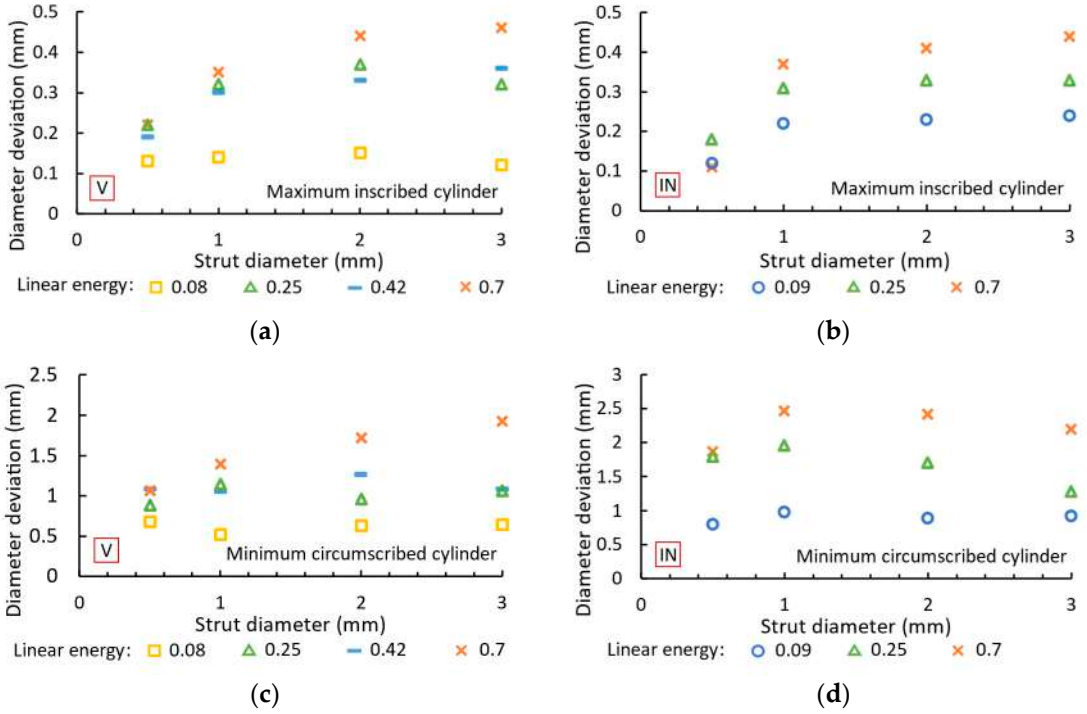

Figure 13. Diameter deviation of maximum inscribed cylinder and minimum circumscribed cylinder from required diameter for (**a**,**c**) vertical and (**b**,**d**) inclined struts.

4. Conclusions

The study described the influence of the process parameters of contour strategy on the relative material density, surface roughness Ra and dimensional accuracy in the production of lattice structures from the magnesium alloy WE43. First, the experiments to determine the process parameters for the contour scanning strategy were evaluated. Then, the vertical and inclined struts were produced and the relative material density, surface roughness and dimensional deviation were analyzed. The best vertical and inclined struts with higher relative material density were used to fabricate BCCZ cells to verify the results. Based on the experiments, the following conclusions were drawn:

- The vertical and inclined struts achieved a relative material density of 99.3–99.6% with an area energy of the process parameters between 1.15 and 3.69 J/mm^2 depending on the strut diameter and inclination.
- BCCZ cells with a diameter of 0.5 mm and 1 mm achieved a relative material density of 99.83–99.96% with small round pores. The BCCZ cells with a diameter of 2 mm and 3 mm achieved a relative material density of 99.32–99.72%.
- Holes were observed in the vertical struts of the 3 mm diameter BCCZ cells, which can be related to contour scanning strategy and large strut diameter.
- The overlap of the welds had a major influence on the porosity formation in the contour scanning strategy. The overlap value was determined based on the width of the weld of hollow strut specimens.
- The low melting point of the magnesium alloy WE43 led to an increase in the diameter of the struts. The load-bearing diameter deviated from the nominal diameter by 4–44% depending on the orientation and diameter of the strut.

Author Contributions: Conceptualization, J.J.; methodology, J.J. and S.S.; validation, J.J.; formal analysis, J.J. and O.V.; investigation, J.J.; resources, J.J.; data curation, J.J.; writing—original draft preparation, J.J.; writing—review and editing, J.J. and O.V.; visualization, J.J.; supervision, D.K. and S.S.; project administration, J.J. and D.K.; funding acquisition, J.J. and D.K. All authors have read and agreed to the published version of the manuscript.

Funding: This research was funded by the project No. FV 22-08 funded by The Ministry of Education, Youth and Sports (MEYS, MŠMT in Czech) institutional support and by faculty-specific research project FSI-S-23-8340.

Data Availability Statement: Supporting data used for the publication are freely available at 10.5281/zenodo.10154211.

Acknowledgments: Special thanks to Martin Malý for providing the Matlab script for the evaluation of thickness and porosity.

Conflicts of Interest: The authors declare no conflicts of interest. The funders had no role in the design of the study; in the collection, analyses, or interpretation of data; in the writing of the manuscript; or in the decision to publish the results.

References

1. Wong, K.V.; Hernandez, A. A Review of Additive Manufacturing. *ISRN Mech. Eng.* **2012**, *2012*, 208760. [CrossRef]
2. Bhuvanesh Kumar, M.; Sathiya, P. Methods and Materials for Additive Manufacturing: A Critical Review on Advancements and Challenges. *Thin-Walled Struct.* **2021**, *159*, 107228. [CrossRef]
3. Wang, X.; Xu, S.; Zhou, S.; Xu, W.; Leary, M.; Choong, P.; Qian, M.; Brandt, M.; Xie, Y.M. Topological Design and Additive Manufacturing of Porous Metals for Bone Scaffolds and Orthopaedic Implants: A Review. *Biomaterials* **2016**, *83*, 127–141. [CrossRef] [PubMed]
4. Zhang, W.-N.; Wang, L.-Z.; Feng, Z.-X.; Chen, Y.-M. Research Progress on Selective Laser Melting (SLM) of Magnesium Alloys: A Review. *Optik* **2020**, *207*, 163842. [CrossRef]
5. Staiger, M.P.; Pietak, A.M.; Huadmai, J.; Dias, G. Magnesium and Its Alloys as Orthopedic Biomaterials: A Review. *Biomaterials* **2006**, *27*, 1728–1734. [CrossRef] [PubMed]
6. Kulekci, M.K. Magnesium and its alloys applications in automotive industry. *Int. J. Adv. Manuf. Technol.* **2008**, *39*, 851–865. [CrossRef]
7. Bai, J.; Yang, Y.; Wen, C.; Chen, J.; Zhou, G.; Jiang, B.; Peng, X.; Pan, F. Applications of Magnesium Alloys for Aerospace: A Review. *J. Magnes. Alloys* **2023**, *11*, 3609–3619. [CrossRef]
8. Zhu, L.; Li, N.; Childs, P.R.N. Light-Weighting in Aerospace Component and System Design. *Propuls. Power Res.* **2018**, *7*, 103–119. [CrossRef]
9. Budholiya, S.; Bhat, A.; Raj, S.A.; Sultan, M.T.H.; Shah, A.U.M.; Basri, A.A. State of the Art Review about Bio-Inspired Design and Applications: An Aerospace Perspective. *Appl. Sci.* **2021**, *11*, 5054. [CrossRef]
10. Ge, S.; Wang, Y.; Tian, J.; Lei, D.; Yu, Q.; Wang, G. An in Vitro Study on the Biocompatibility of WE Magnesium Alloys. *J. Biomed. Mater. Res. Part B Appl. Biomater.* **2016**, *104*, 482–487. [CrossRef]
11. Li, Y.; Zhou, J.; Pavanram, P.; Leeflang, M.A.; Fockaert, L.I.; Pouran, B.; Tümer, N.; Schröder, K.U.; Mol, J.M.C.; Weinans, H.; et al. Additively Manufactured Biodegradable Porous Magnesium. *Acta Biomater.* **2018**, *67*, 378–392. [CrossRef]
12. Levorova, J.; Duskova, J.; Drahos, M.; Vrbova, R.; Vojtech, D.; Kubasek, J.; Bartos, M.; Dugova, L.; Ulmann, D.; Foltan, R. In Vivo Study on Biodegradable Magnesium Alloys: Bone Healing around WE43 Screws. *J. Biomater. Appl.* **2018**, *32*, 886–895. [CrossRef]
13. Aboulkhair, N.T.; Everitt, N.M.; Ashcroft, I.; Tuck, C. Reducing Porosity in AlSi10Mg Parts Processed by Selective Laser Melting. *Addit. Manuf.* **2014**, *1–4*, 77–86. [CrossRef]
14. Galy, C.; Le Guen, E.; Lacoste, E.; Arvieu, C. Main Defects Observed in Aluminum Alloy Parts Produced by SLM: From Causes to Consequences. *Addit. Manuf.* **2018**, *22*, 165–175. [CrossRef]
15. Dong, Z.; Zhang, X.; Shi, W.; Zhou, H.; Lei, H.; Liang, J. Study of Size Effect on Microstructure and Mechanical Properties of AlSi10Mg Samples Made by Selective Laser Melting. *Materials* **2018**, *11*, 2463. [CrossRef]
16. Delroisse, P.; Jacques, P.J.; Maire, E.; Rigo, O.; Simar, A. Effect of Strut Orientation on the Microstructure Heterogeneities in AlSi10Mg Lattices Processed by Selective Laser Melting. *Scr. Mater.* **2017**, *141*, 32–35. [CrossRef]
17. Qiu, C.; Yue, S.; Adkins, N.J.E.; Ward, M.; Hassanin, H.; Lee, P.D.; Withers, P.J.; Attallah, M.M. Influence of Processing Conditions on Strut Structure and Compressive Properties of Cellular Lattice Structures Fabricated by Selective Laser Melting. *Mater. Sci. Eng. A* **2015**, *628*, 188–197. [CrossRef]
18. Han, X.; Zhu, H.; Nie, X.; Wang, G.; Zeng, X. Investigation on Selective Laser Melting AlSi10Mg Cellular Lattice Strut: Molten Pool Morphology, Surface Roughness and Dimensional Accuracy. *Materials* **2018**, *11*, 392. [CrossRef]
19. Vrána, R.; Koutný, D.; Paloušek, D.; Pantělejev, L.; Jaroš, J.; Zikmund, T.; Kaiser, J. Selective Laser Melting Strategy for Fabrication of Thin Struts Usable in Lattice Structures. *Materials* **2018**, *11*, 1763. [CrossRef] [PubMed]
20. Vrána, R.; Jaroš, J.; Koutný, D.; Nosek, J.; Zikmund, T.; Kaiser, J.; Paloušek, D. Contour Laser Strategy and Its Benefits for Lattice Structure Manufacturing by Selective Laser Melting Technology. *J. Manuf. Process.* **2022**, *74*, 640–657. [CrossRef]
21. Pawlak, A.; Rosienkiewicz, M.; Chlebus, E. Design of Experiments Approach in AZ31 Powder Selective Laser Melting Process Optimization. *Arch. Civ. Mech. Eng.* **2017**, *17*, 9–18. [CrossRef]
22. Wei, K.; Gao, M.; Wang, Z.; Zeng, X. Effect of Energy Input on Formability, Microstructure and Mechanical Properties of Selective Laser Melted AZ91D Magnesium Alloy. *Mater. Sci. Eng. A* **2014**, *611*, 212–222. [CrossRef]

23. Wei, K.; Wang, Z.; Zeng, X. Influence of Element Vaporization on Formability, Composition, Microstructure, and Mechanical Performance of the Selective Laser Melted Mg–Zn–Zr Components. *Mater. Lett.* **2015**, *156*, 187–190. [CrossRef]
24. Chen, H.; Zhang, Y.; Giam, A.; Yan, W. Experimental and Computational Study on Thermal and Fluid Behaviours of Powder Layer during Selective Laser Melting Additive Manufacturing. *Addit. Manuf.* **2022**, *52*, 102645. [CrossRef]
25. Song, B.; Dong, S.; Deng, S.; Liao, H.; Coddet, C. Microstructure and Tensile Properties of Iron Parts Fabricated by Selective Laser Melting. *Opt. Laser Technol.* **2014**, *56*, 451–460. [CrossRef]
26. Attar, H.; Calin, M.; Zhang, L.C.; Scudino, S.; Eckert, J. Manufacture by Selective Laser Melting and Mechanical Behavior of Commercially Pure Titanium. *Mater. Sci. Eng. A* **2014**, *593*, 170–177. [CrossRef]
27. Attar, H.; Bönisch, M.; Calin, M.; Zhang, L.-C.; Scudino, S.; Eckert, J. Selective Laser Melting of in Situ Titanium–Titanium Boride Composites: Processing, Microstructure and Mechanical Properties. *Acta Mater.* **2014**, *76*, 13–22. [CrossRef]
28. Hyer, H.; Zhou, L.; Benson, G.; McWilliams, B.; Cho, K.; Sohn, Y. Additive Manufacturing of Dense WE43 Mg Alloy by Laser Powder Bed Fusion. *Addit. Manuf.* **2020**, *33*, 101123. [CrossRef]
29. Pauly, S.; Schricker, C.; Scudino, S.; Deng, L.; Kühn, U. Processing a Glass-Forming Zr-Based Alloy by Selective Laser Melting. *Mater. Des.* **2017**, *135*, 133–141. [CrossRef]
30. Kempen, K.; Thijs, L.; Van Humbeeck, J.; Kruth, J.-P. Mechanical Properties of AlSi10Mg Produced by Selective Laser Melting. *Phys. Procedia* **2012**, *39*, 439–446. [CrossRef]
31. Krištofová, P.; Roudnická, M.; Kubásek, J.; Paloušek, D.; Suchý, J.; Vojtěch, D. Influence of Production Parameters on the Properties of 3D Printed Magnesium Alloy Mg-4Y-3RE-Zr (WE43). *Manuf. Technol.* **2019**, *19*, 613–618. [CrossRef]
32. Tammas-Williams, S.; Zhao, H.; Léonard, F.; Derguti, F.; Todd, I.; Prangnell, P.B. XCT Analysis of the Influence of Melt Strategies on Defect Population in Ti–6Al–4V Components Manufactured by Selective Electron Beam Melting. *Mater. Charact.* **2015**, *102*, 47–61. [CrossRef]
33. Abele, E.; Stoffregen, H.A.; Kniepkamp, M.; Lang, S.; Hampe, M. Selective Laser Melting for Manufacturing of Thin-Walled Porous Elements. *J. Mater. Process. Technol.* **2015**, *215*, 114–122. [CrossRef]
34. King, W.E.; Barth, H.D.; Castillo, V.M.; Gallegos, G.F.; Gibbs, J.W.; Hahn, D.E.; Kamath, C.; Rubenchik, A.M. Observation of Keyhole-Mode Laser Melting in Laser Powder-Bed Fusion Additive Manufacturing. *J. Mater. Process. Technol.* **2014**, *214*, 2915–2925. [CrossRef]
35. Zhang, C.; Liao, Q.; Zhang, X.; Ma, F.; Wu, M.; Xu, Q. Characterization of Porosity in Lack of Fusion Pores in Selective Laser Melting Using the Wavefunction. *Mater. Res. Express* **2023**, *10*, 016501. [CrossRef]
36. Véle, F.; Ackermann, M.; Bittner, V.; Šafka, J. Influence of Selective Laser Melting Technology Process Parameters on Porosity and Hardness of Aisi H13 Tool Steel: Statistical Approach. *Materials* **2021**, *14*, 6052. [CrossRef] [PubMed]
37. Metel, A.S.; Stebulyanin, M.M.; Fedorov, S.V.; Okunkova, A.A. Power Density Distribution for Laser Additive Manufacturing (SLM): Potential, Fundamentals and Advanced Applications. *Technologies* **2018**, *7*, 5. [CrossRef]
38. Nudelis, N.; Mayr, P. A Novel Classification Method for Pores in Laser Powder Bed Fusion. *Metals* **2021**, *11*, 1912. [CrossRef]
39. Vrána, R.; Koutecký, T.; Červinek, O.; Zikmund, T.; Pantělejev, L.; Kaiser, J.; Koutný, D. Deviations of the SLM Produced Lattice Structures and Their Influence on Mechanical Properties. *Materials* **2022**, *15*, 3144. [CrossRef]

ADVANCED ENGINEERING MATERIALS
www.aem-journal.com

Influence of Laser Strategies on Performance of Lattice Structures from Magnesium Alloy WE43 Produced by Laser Beam Powder Bed Fusion

Jan Jaroš, Daniel Ožvoldík, Ondřej Vaverka, Klára Nopová, Jakub Hurník, Tomáš Zikmund, Jozef Kaiser, and Daniel Koutný*

Lattice structures made of magnesium alloys are perspective for lightweight and biomedical applications. The processing of magnesium alloys and the production of complex geometries is possible with laser beam powder bed fusion. However, the small material volume of the lattice structures and the magnesium alloy require specific process parameters in order to achieve a high quality of the material. Therefore, the influence of two perspective laser strategies (contour strategy and hatch strategy), their combination, and skywriting is investigated. The geometry of the body-centered-cubic (BCC) lattice structure is used, representing the most difficult lattice structure to produce due to the struts inclination. A relative material density of over 99% is achieved with three laser strategies. The laser strategies have a direct influence on the pore distribution, pore shape, and microstructure. All these parameters can influence the mechanical performance of the BCC structures. The best performance is achieved with the hatch strategy with skywriting, which results in a low number of dangerous pores and a fine microstructure. The Young's modulus of material of 40 GPa and the effective elastic modulus of BCC structure of 136 MPa are achieved.

1. Introduction

The laser beam powder bed fusion (PBF-LB) process can be used to produce complex geometries from magnesium alloys that are difficult to process using conventional methods.[1,2] One of these geometries is lattice structures that can replace the main material of components to reduce weight or improve heat dissipation.[3,4] However, the production of complex geometries requires process parameters that are optimized for small volume and a specific material.

One of the specific materials processed by PBF-LB is magnesium alloys. They are already used in the automotive and aerospace industries due to their good strength-to-weight ratio, damping characteristics, and thermal conductivity.[5–8] As a lightweight material, magnesium alloys help reduce component weight, which contributes to fuel savings in the automotive and aerospace industries.[9–12] This is in line with the goal of European climate legislation to reduce greenhouse gas emissions in transportation.[13,14] In addition, magnesium alloys are a promising material for biomedical applications due to their biocompatibility and mechanical properties close to those of the human bone.[15]

However, challenges arise due to the narrow range between melting and boiling temperatures (650–1107 °C) of magnesium alloys, which requires precise control of process parameters.[16] The process parameters can be divided into four groups based on the process energy and weld geometry, that is, the insufficient energy range, the high energy range, the balling effect range, and the suitable energy range.[17–19] Insufficient energy range is defined by the low energy of the process parameters, which cannot ensure the required temperature to melt all powder particles. Delamination and high porosity with an irregular pore shape are typical.[20] In the high-energy range, the powder is vaporized and expands rapidly, causing a strong recoil in the melt pool which blows away both the melt and the powder. In addition, vapors affect the performance of the laser, leading to a reduction in process energy.[21] The range of the balling effect is defined by low laser power, high laser speed, and high layer thickness. The balling effect is caused by the insufficient

J. Jaroš, O. Vaverka, J. Hurník, D. Koutný
Institute of Machine and Industrial Design
Faculty of Mechanical Engineering
Brno University of Technology
Technicka 2896/2, 616 69 Brno, Czech Republic
E-mail: Jan.Jaros2@vut.cz

D. Ožvoldík, T. Zikmund, J. Kaiser
CEITEC - Central European Institute of Technology
Brno University of Technology
Purkynova 123, 612 00 Brno, Czech Republic

K. Nopová
Faculty of Mechanical Engineering
Institute of Materials Science and Engineering
Brno University of Technology
Technická 2896/2, 616 69 Brno, Czech Republic

The ORCID identification number(s) for the author(s) of this article can be found under https://doi.org/10.1002/adem.202402625.

DOI: 10.1002/adem.202402625

wettability of the melt pool with the previous layer. This impairs the cohesion of the laser tracks and thus prevents the formation of further layers.[22] Suitable energy is defined by the stable formation of a melt pool, which leads to a high relative material density (up to 99.5%).[23]

The optimal process parameters differ with the complexity of the geometry of the desired components.[24] One of the cases of complex geometries is the strut-based lattice structure. The PBF-LB process provides a high-energy input that melts the powder particles, but also depends on the cooling rate of the molten material. With bulk material, the heat is dissipated through the previously built-up layers However, with lattice structures, the situation changes as the downskin of the inclined strut does not have enough material to dissipate all the energy through it. Part of the energy is dissipated through powder particles, which have a low dissipation rate.[25] This situation causes the material in the downskin of the strut to be kept at a high temperature for a long period of time. Therefore, the downskin of the inclined strut is prone to porosity and the powder particles are partially fused to the surface of the struts.[24,26]

Heat dissipation also affects the morphology of the molten pool, which is crucial to establish sufficient metallurgical connections with solidified material in the previous layers.[27] The microstructure can be affected by high temperatures, which can result in the boundaries of the melt pool not being clearly recognizable and the microstructure being coarse.[28,29] Changes in the process parameters or laser strategy can lower the temperature of the material and cause a fine microstructure.[30] According to Delroisse et al.[25] The different heat dissipation in the upskin and downskin of the strut lead to changes in the microstructure. The upskin has sufficient heat dissipation, resulting in a fine microstructure. The downskin has a coarser microstructure due to the high temperature.

The input energy can be controlled not only with the process parameters, but also with the laser strategy. There are promising laser strategies for the geometry of the lattice structure[31–33] that should be investigated: hatch strategy and contour strategy.

The hatch strategy is a common strategy for the production of complex components. The strategy is defined with a contour for the outer cross-section shape and parallel laser trajectories in one direction for the core. The parallel laser trajectories rotate between the layers to ensure thorough bonding of the melt pool and a fine microstructure. The connection between the contour and the inner laser trajectories is prone to pore formation as a result of the deceleration of the laser at the end of the laser trajectories. Therefore, surface processing is required in many cases.[34,35] Subsurface porosity can be reduced using skywriting.[36]

The contour laser strategy uses concentric laser trajectories and is suitable for small-volume components with circular geometry, such as the lattice structures.[37] The contour strategy was successfully used for the production of high-density zbody-centered-cubic cells (BCC) with a strut diameter of 0.5 mm and 1 mm from the magnesium alloy WE43. The relative material density was over 99.5%. The strut diameter over 1 mm led to irregular pores.[38]

The selection of process parameters and laser strategies is the key to PBF-LB production of high-quality lattice structures. According to the Gibson–Ashby material model,[39] the mechanical properties of the structures are determined by the cell topology, the mechanical properties of the parent material, and the relative density of the structure, which are defined by the volume of the material in the unit cell.[40,41] The mechanical properties of lattice structures are also influenced by the geometry of the struts, with a nonconstant cross section and a variation in pore volume having a negative effect.[42,43]

Considering a strut-based lattice structure with a cubic cell, the BCC lattice topology consists of the struts with the most unfavorable case of feasible inclination angle, that is, 35.26°.[44] Therefore, the manufacturing defects have a much greater impact on the material quality than in the case of a different strut orientation. In addition, the mechanical properties can be affected. Furthermore, according to Maxwell's criterion,[45] the dominant deformation mechanism for the BCC cell topology is bending, which is less effective in terms of load transfer than the stretching-dominated cell topologies.[46]

The combination of the inclination of the struts and the low volume of the material makes the production of BCC lattice structures difficult and, therefore, in many cases leads to the formation of porosity and a high surface roughness.[25,47] These imperfections have a negative impact on the mechanical properties of the parent material. As Dong et al.[48,49] have shown on the single struts, the Young's modulus of material can decrease by almost 30% due to the size effect and by a further 12% when the inclination angle is reduced to 35.26°. Tsopanos et al. and Červinek et al.[50,51] used multistrut tensile samples to determine the actual value of the Young's modulus of the parent material of the lattice structure. Červinek et al.[51] also showed a good correlation between the compression tests and the finite-element analysis (FEA) using the material properties of the struts. Vaverka et al.[52] used the comparison between experiment and FEA with solid geometry and the Young's modulus as a parameter to determine its actual value from the compression test. In the case of the WE43 magnesium alloy, Young's modulus of bulk material is about 45 GPa.[53,54] According to the studies mentioned above, however, the Young's modulus of the material of BCC lattice structures should be lower.

This article describes the importance of laser strategy and process parameters considering relative material density, pore formation, microstructure, mechanical properties, and failure behavior. A geometry of the BCC lattice structure with a strut diameter of 1.5 mm is used. This geometry is prone to imperfections due to the inclination of the struts; therefore, the effect of the laser strategy is highlighted. Two laser strategies are used, the contour strategy and the hatch strategy. The influence of skywriting and the combination of both strategies are also investigated.

2. Experimental Section

2.1. Process Parameters

First, the contour strategy and the hatch strategy were used to find the process parameters for the production of BCC lattice structures with high material density. The geometry of BCC lattice structures was the most challenging for production due to the most unfavorable inclination of the struts.[44] As a sample, the BCC cell with a diameter of 1.5 mm was used. The cell size was 10 mm. The BCC cells represented low volume geometry

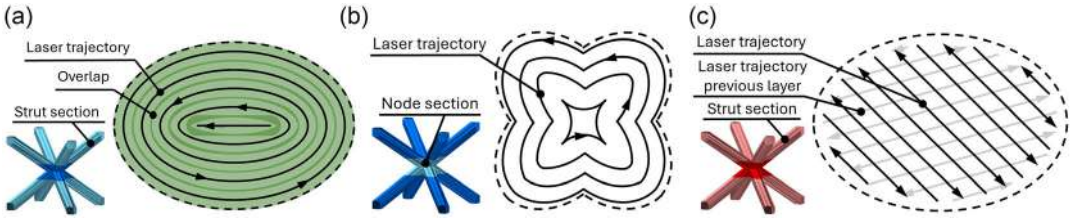

Figure 1. Laser trajectories in BCC cells for: a) contour strategy in strut, b) contour strategy in node, and c) hatch strategy in strut.

and yet had enough material to determine the effects of process parameters and laser strategies on pore formation, microstructure, and mechanical properties.[48]

The contour strategy consisted of concentric laser trajectories used to scan a cross section of the sample. In the struts, the laser trajectories formed an elliptical shape (**Figure 1**a). However, in the node of the BCC cell, where sharp edges were formed, the laser trajectories were different. In these areas, the hatch distance between the trajectories was not consistent, which is crucial for pore formation (Figure 1b).

Compared to the standard hatch strategy, a hatch strategy without a contour trajectory at the edge of the cross section was used in this study (Figure 1c). Therefore, the same variable process parameters can be used for hatch strategy and contour strategy, that is, laser power, laser speed, and hatch distance. The laser trajectories in hatch strategy rotated by 67° in each layer.

The BCC cells were produced by PBF-LB process on the SLM 280HL machine (SLM Solutions Group AG, Lübeck, Germany). This machine used an ytterbium laser with Gaussian distribution and a spot diameter of 82 µm. An atomized magnesium alloy WE43 (Luxfer MEL Technologies, Manchester, UK) with a particle size distribution of 28–60 µm and an average particle size of 39.8 µm was used. The chemical composition is listed in **Table 1**. The samples were produced in an argon atmosphere and the platform temperature was 120 °C. The layer thickness was 50 µm.

The range of process parameters was selected based on the design of experiment (DOE). The input parameters were a laser power of 50–250 W and a laser speed of 200–1200 mm s^{-1}. The overlap between two laser trajectories was defined as 40, 50, and 60% of the weld width. The hatch distance, the range of process parameters, and the overlap values were based on a previous study.[38] The hatch distance was determined by the overlap of the weld width. Therefore, the supporting data from a previous study was used to define the weld width.[55] The weld width was measured on the hollow strut samples with a diameter of 1.5 mm that represented the geometry of the strut. The response surface regression method was used to interpolate data of the weld width. The regression coefficient was 90.12%, so the data are well described. The equation used in this study to define the weld width is as follows (Equation (1)), where *TW* represents track width (mm), *LP* represents laser power (W), and *LS* represents laser speed (mm s^{-1}).

Table 1. Chemical composition of WE43 powder.

	Mg [wt%]	Y [wt%]	Zr [wt%]	Nd [wt%]	Si [wt%]	Cu [wt%]
WE43 powder	Bal.	3.96	0.56	2.30	<0.01	<0.01

$$TW = 0.3925 + 0.002454LP - 0.001157LS + 0.000001LS^2 - 0.000002LPLS \quad (1)$$

A total of 60 BCC cells were produced. The influence of the process parameters on the relative material density was measured on the metallographic cross sections due to the high number of samples. The analysis had sufficient accuracy to measure the relative density of the material to compare the samples. The center of the node is a critical area that was influenced by different laser trajectories. Therefore, the cross sections were performed in the center of the BCC cells.

2.1.1. Metallographic Cross-Sections Analysis

The relative material density from the metallographic cross section was analyzed using DOE response surface analysis. The analysis was performed using Minitab analysis software (Minitab, LLC, State College, Pennsylvania). The values of the relative material density for laser power and laser speed were interpolated with the response surfaces. Based on the interpolated data, the potentially best process parameters can be determined. These parameters were selected with the aim of maximizing the relative density of the material. Based on the prediction, two sets of process parameters were selected and evaluated by micro-computed tomography (µCT) analysis to compare the predicted process parameters with the parameters that achieved the highest relative material density in the cross sections.

2.2. Laser Strategies

In this study, five strategies were used for the production of BCC cells. 1) Contour strategy; 2) hatch strategy; 3) hatch strategy with skywriting (hatch + skywriting); 4) combination of contour strategy and hatch strategy (contour–hatch) and 5) combination of contour strategy and hatch strategy with skywriting (contour–hatch + skywriting).

2.2.1. Contour Strategy and Hatch Strategy

The relative material density of the BCC cell produced with the contour strategy and hatch strategy was evaluated by µCT analysis. This allowed the pore distribution and pore size to be recognized throughout the entire geometry. The BCC cells were produced with two perspective combinations of process parameters for each laser strategy. The first combination of process parameters represents a high relative material density obtained

from metallographic cross sections. The second combination was selected based on DOE response surface analysis. Three samples were produced for each set of process parameters and each laser strategy. A total of 12 BCC cells were produced.

2.2.2. Skywriting

Typically, the hatch strategy is used for the PBF-LB process. This strategy leads to a higher subsurface porosity due to the laser movement. The movement of the laser is controlled by a high-precision electro-optical galvanometer system. Finally, a certain amount of time is needed to accelerate and decelerate the galvanometer mirrors. This is crucial for the initial and final part of the laser trajectory, where the speed of the laser is not constant. Skywriting extends the laser trajectories beyond the scanned cross-section (**Figure 2**).The extended trajectory is used for the acceleration and deceleration of the galvanometer mirrors. Therefore, the laser trajectory covering the desired cross section of the part is scanned at a constant laser speed.[56,57]

The process parameters that lead to a higher relative material density based on the μCT analysis for hatch strategy were used. Three BCC cells were produced. The relative density of the material, the pore distribution, and the pore size of BCC cells were evaluated by μCT analysis.

2.2.3. Combination of Contour Strategy and Hatch Strategy

The combination of the contour strategy and the hatch strategy (contour–hatch) should utilize the advantages of both strategies.

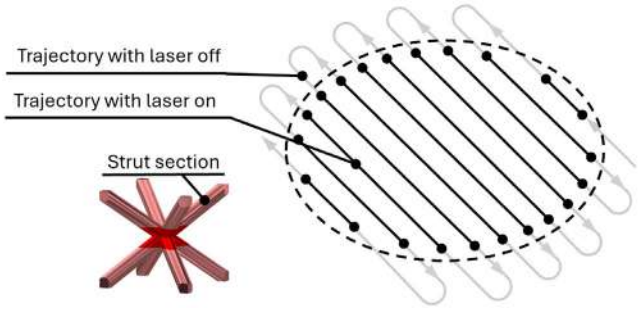

Figure 2. Hatch strategy with skywriting.

The contour strategy proved to be suitable for the production of struts due to the concentric laser trajectories (Figure 1a).[24] The hatch strategy is suitable for the production of nodes due to the larger material volume.[31] In addition, the laser trajectories in the nodes are stable over large geometry variations (Figure 1c).

The combination of contour strategy and hatch strategy with the skywriting (contour–hatch + skywriting) was also investigated. As already mentioned, skywriting can reduce the pores in zhatch strategy. The effects on the contour strategy were not tested.

Three BCC cells were produced for each combination of laser strategies. Based on the μCT analysis of the contour strategy and hatch strategy, process parameters with higher relative material density were selected. The relative material density, pore size, and pore distribution in the BCC cell were investigated by μCT analysis.

2.3. Relative Material Density

2.3.1. Metallographic Cross Sections

Metallographic cross sections are used to determine perspective process parameters. Due to the high number of samples, metallographic cross sections are used as a cheaper and faster method to determine the relative material density than μCT analysis. The BCC cells produced using the contour strategy and hatch strategy with different process parameters were metallographically grounded and polished to the cell center. The polished samples were recorded (**Figure 3**a,b) by a digital microscope (Keyence VHX-6000, objective Z250R, zoom 250×, Keyence, Mechelen, Belgium). The images were converted to binary images using the threshold method and the Otsu method.[58] The black color represents the pores, and the white color represents the material. The percentage of white color represents the relative material density of the samples.

2.3.2. μCT Analysis

The μCT analysis was used to evaluate the relative material density of whole BCC cells. The pore size, shape, and position were also determined. For small-volume samples, these factors were crucial for their mechanical performance.

CT scans of BCC cells were performed with the μCT machine (GE Phoenix V Tome X L240, GE Sensing and Inspection

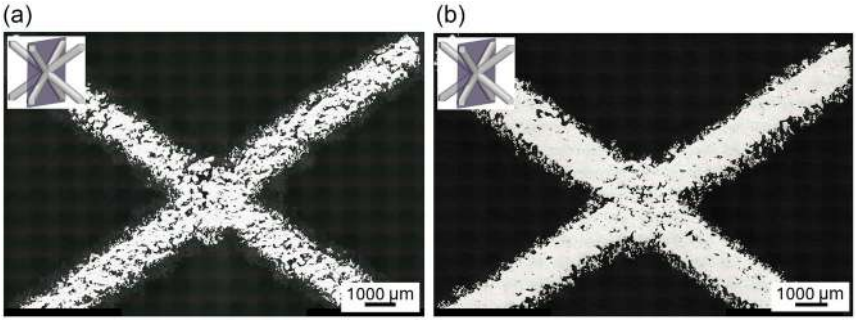

Figure 3. The metallographic cross sections of BCC cells produced with same process parameter but different laser strategies: a) contour strategy and b) hatch strategy.

Technologies GmbH; Wunstorf, Germany). The resolution of the minimum fundamental volumetric element (voxel) was 10 µm. The number of individual projections that generate a composite volume was 2000 with a rotation of 360 degrees. To achieve high-quality scans, a shift was used to define the movement of the detector to avoid possible ring artifacts.[59] The copper filter in combination with the 20° tilt of the cell reduced beam hardening artifacts. Before each measurement, the inspection setup was calibrated with the spherical rod-type VTX18CE0000 S/N 780446 (GE Sensing and Inspection Technologies GmbH; Wunstorf, Germany) using a 180 kV/15 W Nanofocus X-ray tube with a voltage setting of 110 kV, a current of 240 µA, an integration time of 334 ms, and an average of 3 images taken in one projection. The copper filter had a thickness of 0.2 mm.

The data was processed in VGSTUDIO MAX 2023.4.1 (Volume Graphics, Heidelberg, Germany). BCC cells contain partially melted powder particles that are bound to the material of the cell. The relative material density was only calculated from the material of the cell without powder particles on the surface. For this purpose, the closing and erode functions of the originally defined surface of the cell were used. The single cell with the largest volume of material was then isolated and was ready for relative material density and porosity analysis (**Figure 4**).

In addition to the relative density of the material and the pore distribution, the individual parameters of the pores were analyzed. The sphericity value was based on the ratio between the pore volume (S_{pore}) and the pore surface area (S_n). More precisely, sphericity was determined by the ratio between the surface area of a sphere with the same volume as the pore and the actual surface area of the pore (Equation (2)). The value of the sphericity describes the shape of the pore.

The second parameter of the pore was the compactness. The compactness of the pore can be described as the volume of the pore distributed in space (Equation (3)). The value was calculated as the ratio of the pore volume (V_{pore}) to the volume of the sphere (V_n), which was defined by the maximum radius around the pore.[60,61]

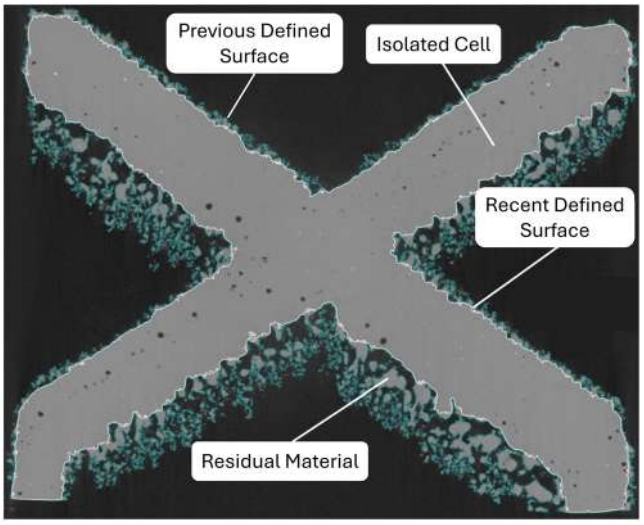

Figure 4. Raw µCT data visualized in the section.

$$\Psi = \frac{S_n}{S_{\text{pore}}} = \frac{\sqrt[3]{36\Pi V_{\text{pore}}^2}}{S_{\text{pore}}} \tag{2}$$

$$\Omega = \frac{V_{\text{pore}}}{V_n} = \frac{V_{\text{pore}}}{\frac{4}{3}\Pi R_{\text{pore}}^3} \tag{3}$$

2.4. Melt Pool Morphology and Microstructure

Melt pool morphology and microstructure are observed to determine the influence of laser strategies on material formation. The selected samples represented laser strategies with the highest relative material density measured by µCT. The samples were grounded and polished in the same orientation as in Section 2.3.1. Each sample was etched using the 2% nitric acid alcohol solution. The light microscope (Olympus GX51, Olympus, Tokyo, Japan) was used to capture images of the melt pool morphology.

Scanning electron microscopy (SEM) was used to obtain a detailed microstructure and chemical composition of the material. The analysis was performed with the SEM (Zeiss Ultra Plus, ZEISS, Oberkochen, Germany) equipped with an energy-dispersive X-ray spectrometer (EDS) (X-Max 20, Oxford Instruments, Abingdon, Oxfordshire, UK). An accelerating voltage of 10 kV was used.

2.5. Quasistatic Compression Testing

Quasistatic compression loading is used to determine the influence of laser strategies on the mechanical performance of structures. 3 × 3 × 3 BCC lattice structures with a diameter of 1.5 mm and a cell size of 10 mm were fabricated in three samples for each laser strategy. The three best laser strategies were selected based on the relative material density measured by µCT. A quasistatic compression test (Shimadzu AGX-V 100kN, Shimadzu Corporation, Kyoto, Japan) was performed. The test speed was 1 mm min^{-1}, which corresponded to a strain rate of 3.3% min^{-1}. The displacement was measured with the mechanical extensometer, which was placed on the compression plates. The sampling rate was 100 Hz.

The deformation behavior of the specimens under the quasistatic compression loading was recorded with a digital 3D image correlation system (DIC) from Dantec Dynamics (Dantec Dynamics a/s, Skovlunde, Denmark). Before the test, the samples were sprayed with a fine, high-contrast stochastic pattern. The DIC setup consisted of two 5 MPx cameras with 50 mm objectives. With a stereo base of ≈150–175 mm and an angle of 20°–25°, the setup can capture deformations in an area of ≈50 × 50 mm. The facet size and grid spacing were set to 25 and 13 px, respectively, to achieve sufficient reliability and a dense, overlapping mesh. The frame rate for the acquisition was set to 1 Hz. The images were used to visualize the directional deformation in the loading direction over the entire field to investigate the failure mode of the BCC lattice structures.

2.6. Geometry Analysis

The strut diameter of the structures is measured in order to determine the influence of the laser strategies on the material properties using FEA. The diameter of the strut was measured with an optical 3D scanner (Atos Triple Scan III, GOM GmbH, Braunschweig, Germany). The data was processed in GOM Inspect software, where polygonization and digitization were used. Two diameters were measured, namely, the maximum inscribed diameter, which represents the load-bearing material of the strut, and the minimum circumscribed diameter, which represents geometrical irregularities.

Three BCC cells were analyzed for each of the three laser strategies. The four struts at the top of the cell were measured. These struts were fully scanned due to the good visibility of the strut surface. Therefore, the four values were determined for each cell, resulting in 12 values for the laser strategy.

2.7. Finite-Element Analysis

FEA is used to determine the Young's modulus (YM) of the parent material based on the model of structure represented by the measured diameter. Based on the literature,[48–52] the YM of the parent material for the lattice structure differs from the YM of the bulk material. The simulations were performed in ANSYS Workbench (Ansys Inc., Canonsburg, Pennsylvania).

2.7.1. Material Definition

The magnesium alloy WE43 was defined by a bilinear material model. The parameters were specified by the powder manufacturer: Poisson's ratio 0.27, yield strength 220 MPa, Young's modulus 45 GPa, and tangent modulus 920 MPa. The variable parameter was Young's modulus which changed in steps of 5 GPa until the deviation between the effective elastic modulus of the experiment and the simulation was less than 5%.

2.7.2. Simulation

The quarter geometry model was used for the simulation in order to reduce the number of degrees of freedom and thus the computation time (**Figure 5**a). The rest of the structure was represented by symmetry boundary conditions in the *X* and *Z* directions, which also contributed to the computational stability of the simulation. The diameter of the struts corresponded to the maximum inscribed diameter measured in the 3D scan (Section 2.6).

The structure was placed between two plates with a thickness of 0.5 mm. The bottom plate was fixed, and a displacement of −2 mm in *Y* direction was applied to the top of the upper plate. The material of the test plates was stainless steel, which had a 50 000-fold higher YM. This means a higher rigidity of the testing machine compared to the structure. The coefficient of friction of 0.45 corresponded to the contact between stainless steel and the WE43 magnesium alloy.[62]

The size of the mesh element was determined on the basis of a mesh sensitivity analysis. An element size of 0.2–1 mm was tested and the result is shown in Figure 5b. The criterion was that the difference between the force and the force with a higher element size must be less than 1%. At the same time, the degrees of freedom must be small. The criterion was fulfilled with an element size of 0.6 mm, which was used for all samples. Direct solver was used.

The output of the simulation was the force reaction and displacement in Y direction which can be compared with the results. The force reaction was obtained from the contact between the BCC structure and the top plate. The displacement was determined by the displacement of the top plate.

3. Results and Discussion

3.1. Process Parameters Selection

The relative material density of BCC cells processed by metallographic cross sections is evaluated by DOE response surface analysis. The coefficient of determination is 94.73 and 90.89% for the contour strategy and the hatch strategy, respectively. The process parameters with an overlap of 60% achieve a higher relative material density than overlap 50 and 40%. The influence of laser power and laser speed on the relative material density is shown in **Figure 6**. The contour strategy (CS; Figure 6a) and the hatch strategy (HS; Figure 6b) show differences in the orientation of the process parameters area with high relative material density (99%). The same process parameters for both strategies lead

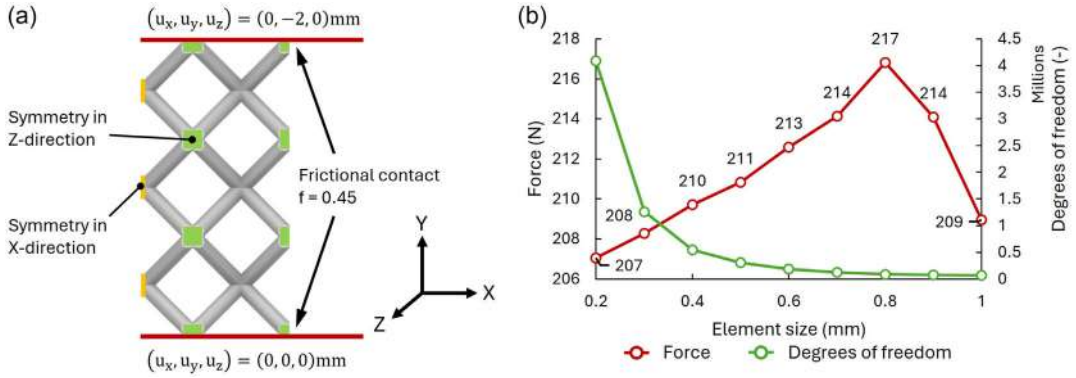

Figure 5. FEA simulation conditions: a) simulation setup and b) influence of element size on force and degrees of freedom.

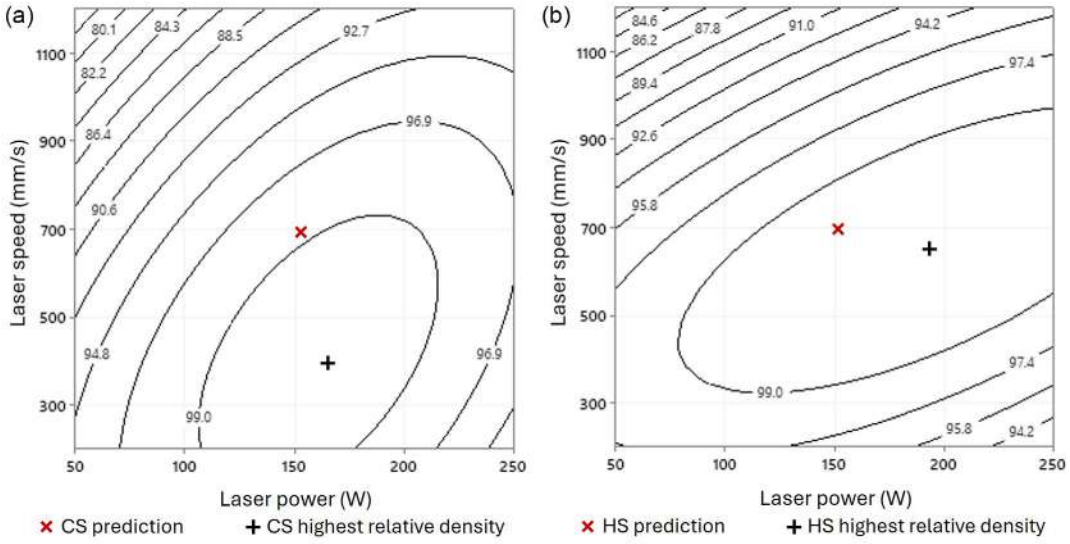

Figure 6. Dependence of relative material density on laser power and laser speed of BCC cells for overlap of 60% produced with: a) contour strategy and b) hatch strategy.

to different pore formation. The differences can be seen in the Figure 3. Figure 6 visually represents the equation from response surface analysis for the contour strategy (Equation (4)) and for the hatch strategy (Equation (5)), where *RMD* stands for the relative material density (%), *LP* for the laser power (W), and *LS* for the laser speed (mm s^{-1}).

$$RMD = 89.82 + 0.1334LP - 0.00182LS - 0.000532LP^2 - 0.000016LS^2 + 0.000092LPLS \quad (4)$$

$$RMD = 94.11 + 0.0194LP + 0.01400LS - 0.000206LP^2 - 0.000024LS^2 + 0.000091LPLS \quad (5)$$

Based on the results, two perspective combinations of the process parameters for the contour and hatch strategy are determined. The first is the process parameter that leads to a higher measured relative material density, that is, 98.99% for the contour strategy and 98.97% for the hatch strategy. The second is the combination of process parameters selected based on the prediction using the equations (Equation (4) and (5)) from the DOE surface response analysis. The aim of the analysis is to achieve maximum relative material density. The combinations of process parameters for the contour strategy (contour, prediction contour) and the hatch strategy (hatch, prediction hatch) are listed in **Table 2**.

Table 2. Perspective process parameters from metallographic sections.

Laser strategy	Laser power [W]	Laser speed [mm s^{-1}]	Overlap [%]	Hatch distance [mm]
Contour	150	200	60	0.20
Hatch	150	700	60	0.09
Prediction Contour	161	412	60	0.14
Prediction Hatch	191	655	60	0.11

3.2. Influence of Laser Strategies on the Relative Material Density

The relative material density of BCC cells produced with different laser strategies is evaluated by μCT analysis. Moreover, pore formation, distribution, shape, and size are determined. First, samples produced with perspective combinations of process parameters are evaluated. The predicted process parameters achieve a lower relative material density compared to the process parameters leading to a higher relative material density from cross sections (**Table 3**). Therefore, the process parameters (contour and hatch in Table 2) are used for further experiments.

The influence of skywriting and the combination of contour and hatch strategies is further investigated. Skywriting has the potential to reduce the pores near the surface. The combination of contour and hatch strategies can combine the advantages of botch strategies, that is, contour for struts and hatch for nodes.

The relative material density of BCC cells produced with different laser strategies is shown in **Table 4**. The hatch strategy with skywriting (hatch + skywriting) achieves a relative material density of more than 99.5%. Skywriting reduces pore formation compared to the hatch strategy without skywriting (98.8%). The combination of contour strategy for struts and hatch strategy for nodes (contour–hatch) achieves a relative material density of over 99.1%. The relative material density does not improve compared

Table 3. Average relative material density of perspective combinations of process parameters.

Laser strategy	Relative material density [%]	Std. deviation [%]
Contour	99.13	0.006
Hatch	98.87	0.111
Prediction Contour	98.76	0.038
Prediction Hatch	97.88	0.044

Table 4. Average relative material density for skywriting and combinations of laser strategies.

Laser strategy	Relative material density [%]	Std. deviation [%]
Hatch + skywriting	99.55	0.025
contour–hatch	99.11	0.020
contour–hatch + skywriting	98.67	0.029

to the contour strategy. Compared to the hatch strategy (98.87%) the relative material density is improved, which indicates the positive effect of the contour strategy on the struts. No positive effect is observed when combining the contour and hatch strategy with skywriting (contour–hatch + skywriting).

The average relative material density of over 99% is achieved with three laser strategies (Table 3 and 4), that is, contour strategy, hatch + skywriting, and contour–hatch. These strategies are further analyzed to determine the pore distribution, pore number, pore size, and pore shape. The microstructure is also discussed with respect to the strategies and process parameters. The quality of the material is important for the mechanical properties, that are determined based on the compressive load and simulation.

3.2.1. Pore Distribution

The pore distribution can help to understand the pore formation in the material depending on the laser strategy. The μCT images show the distribution of the pores through the BCC cell and one of the cell struts (**Figure 7**). The majority of the pores have a volume of up to 0.0016 mm^3. The pore distribution and the number of pores differ depending on the laser strategy. In the case of hatch + skywriting (Figure 7a), the node contains a small number of pores. This indicates the suitability of the hatch strategy for a higher volume of material in the node.[48] The pores in the struts are located mainly in the area of the downskin, which is due to heat dissipation during production.[25] The downskin area is kept at high temperature, which increases the flowability of the melt pool and leads to the creation of keyhole pores.[24] Skywriting has a positive effect on pore formation in the subsurface area (Figure 7a), compared to the hatch strategy without skywriting (Figure 7b). The slowing down of the laser at the end of the trajectories has a visible influence.[63]

The pores in the contour strategy are located between the laser trajectories (Figure 7c). This pore formation is typical for the lack of fusion pores caused by insufficient overlap of the laser trajectories.[32] The effect is magnified by the unidirectional pattern of the laser trajectories.[64] The node contains more pores than in the hatch strategy, which may be caused by overheating of the material at the sharp edges of the laser trajectories (Figure 1b).

The pore distribution in the contour–hatch (Figure 7d) corresponds to the laser strategy used specifically in the struts or in the node. The hatch strategy in the node region reduces the formation of pores compared to the contour strategy. In the struts, the contour strategy shows a distribution of pores between the laser trajectories.

The pore distribution is also influenced by the flow of the inert gas atmosphere. In magnesium alloys, this influence is

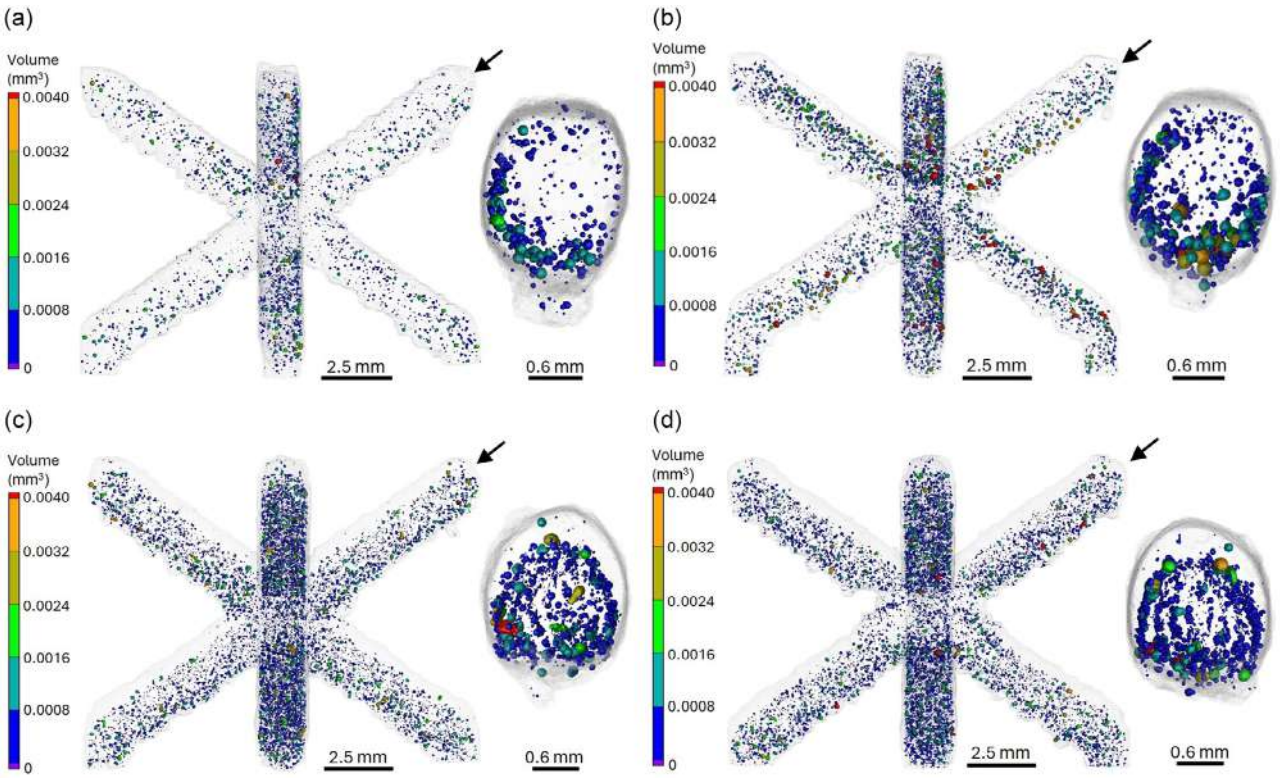

Figure 7. Pore distribution in BCC cells with details of the strut for: a) hatch + skywriting, b) hatch strategy, c) contour strategy, and d) contour–hatch.

further magnified by the formation of fumes during PBF-LB processing.[65] The contour strategy is less susceptible to this phenomenon which can be seen in the Figure 7c,d, where pores are evenly distributed. In the case of hatch strategy and hatch + skywriting, the pores gather closer to the gas outlet (left side of the strut - Figure 7a,b). As the powder is melted, the fumes are removed by the atmospheric argon flow.[21] Due to the high speed of the process, the laser power is reduced especially in the area near the outlet of the atmosphere, where the fumes are still present. These areas are therefore susceptible to the formation of pores.

The laser strategy influences not only the number of pores and their distribution in the material but also the volume (Figure 7) and shape (**Figure 8**). The compactness to sphericity graphs is used to visualize the pore geometry.[61] Pore geometry can be used to determine the effect of pores on the initiation of potential cracks during loading, especially in cyclic tests.[66,67] Pores with a compactness of 0–0.5 and a sphericity of 0–0.55 have an irregular shape and can be classified as potentially dangerous.

The hatch + skywriting reduces the number of pores and the number of dangerous pores (Figure 8a). The main concentration of pores is between a compactness of 0.4–0.8 and a sphericity of 0.6–0.7. The hatch + skywriting has a lower number of dangerous pores, which can have a positive effect on mechanical performance. The contour strategy (Figure 8b) and the contour–hatch (Figure 8c) lead to a higher number of pores. In addition, more dangerous pores are accumulated in the material. More dangerous pores lead to high stresses in the material in the area closer to the pore irregularity. This can have a negative effect during loading.[61]

3.3. Melt Pool Morphology and Material Microstructure

The morphology of the melt pools formed by the PBF-LB process is shown in **Figure 9**. All investigated samples show a typical melt pool morphology consisting of overlapping solidified melt pools, indicating good metallurgical bonding between the layers (Figure 9a). The microstructure within the melt pool consists of a lamellar region near the melt pool boundary and a region with equiaxed grains in the center of the melt pool (Figure 9b). The gradual transition of the microstructure can be attributed to decreasing cooling rates and the decreasing temperature gradient from the boundary of the melt pool to the center of the melt pool.[28,68] Solidification leads to an increase in the strength and ductility of the material.[69]

The metallographic sections of the struts showed a lower occurrence of keyhole pores in the hatch + skywriting (**Figure 10**a) than in the contour strategy (Figure 10b). This effect can be attributed to the higher energy density (75 J mm^{-3}) in the contour strategy than in the hatch strategy (47.62 J mm^{-3}). Moreover, the higher-energy input leads to an increase in the flowability of the melt pool, which causes no clear boundaries of the melt pool. For hatch + skywriting (Figure 10a), no clear boundaries can be recognized only in the downskin area of the struts. This is

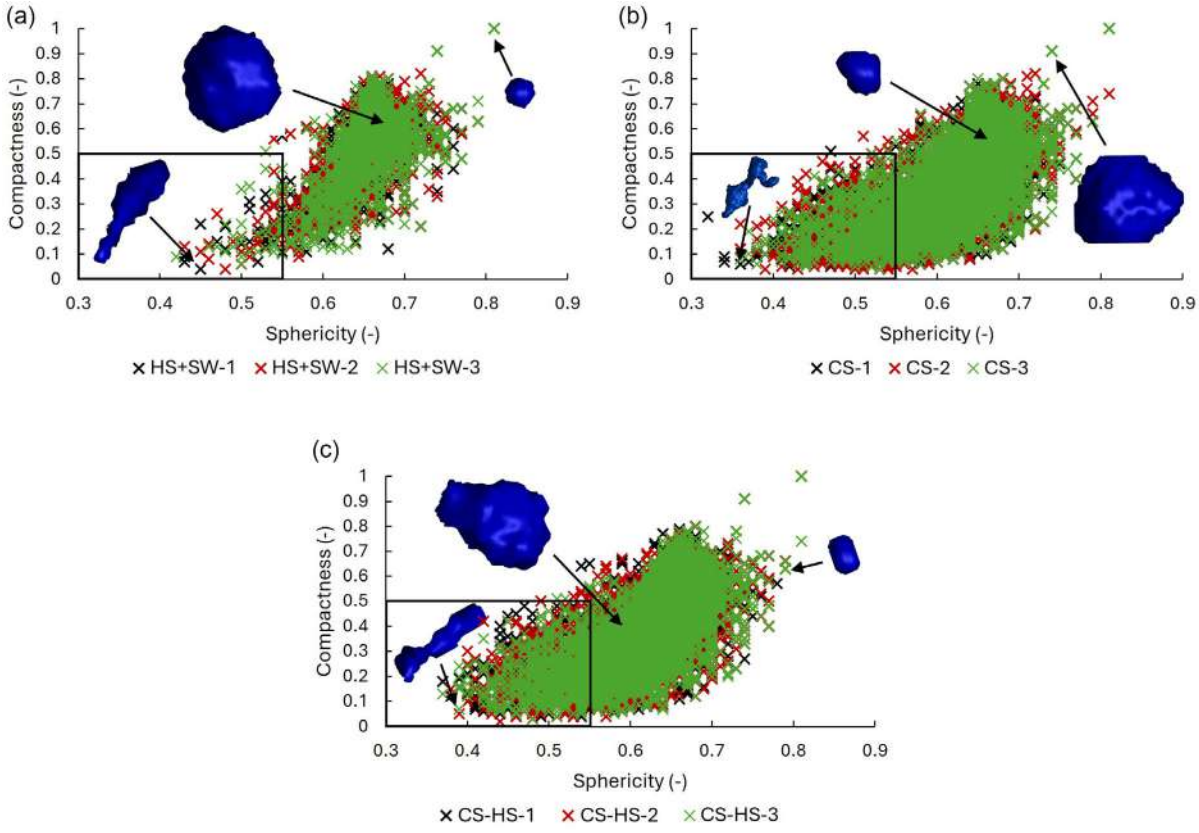

Figure 8. Compactness–sphericity dependence of pores for: a) hatch + skywriting, b) contour strategy, and c) contour–hatch.

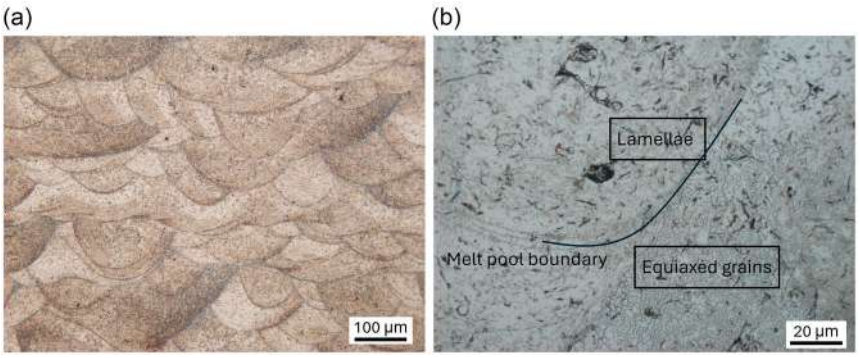

Figure 9. Melt pool morphology: a) superposition of melt pools for hatch + skywriting and b) enlarged melt pool boundary for contour–hatch.

Figure 10. Keyhole pores and the effect of no clear boundaries: a) hatch + skywriting, b) contour strategy, and c) transition between node and strut for contour–hatch.

due to the low heat dissipation in the downskin.[25] No clear boundaries are visible in upskin and downskin area of the struts for contour strategy (Figure 10b). In the case of contour–hatch the same phenomenon is visible in the transition area between contour and hatch strategies. The lack of clear boundaries of the melt pool can have a negative effect on the mechanical properties.[68]

The metallographic sections of the nodes show clear melt pool boundaries for hatch + skywriting (**Figure 11**a) and hatch strategy in the contour–hatch (Figure 11c). The round keyhole pores are present in small numbers. In the case of the contour strategy (Figure 11b), the situation is different. The boundaries of the melt pool are clearly visible only in the center of the node. The node contains more pores, especially more irregular pores (represented by the red arrows in Figure 11b). The irregular pores are located on the side of the melt pool, which corresponds to the formation of pore in the contour strategy (Figure 7c). The pores are formed between the laser trajectories, which is due to a lack of fusion. The contour–hatch strategy leads to visible boundaries of the melt pool in the bottom area of the node (Figure 11c). The upper area is affected by the high energy of the contour strategy used for struts. The large depth of the weld width causes the boundaries of the weld pool to disappear.[17]

The nodes of the BCC structures are used for the SEM–EDS analysis. For all three laser strategies, the chemical composition corresponds to the chemical composition of the WE43 powder (Table 1). The chemical composition is not influenced by the

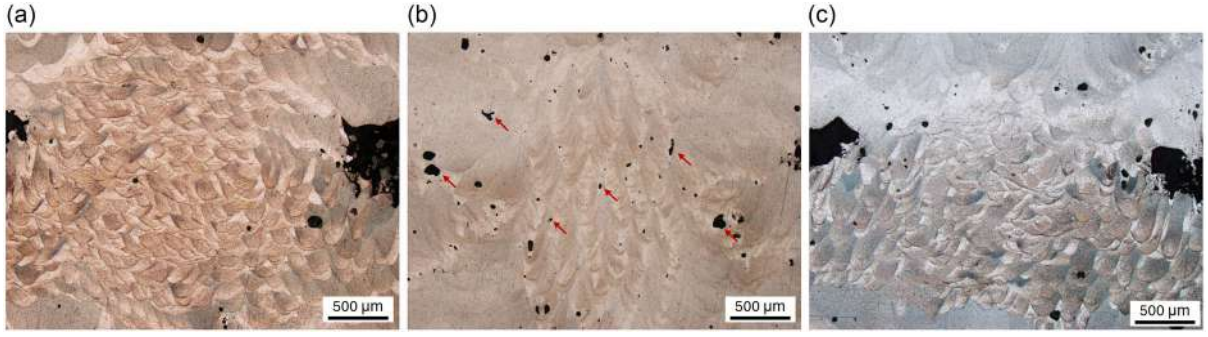

Figure 11. Microstructure and porosity in the node for: a) hatch + skywriting, b) contour strategy, and c) contour–hatch.

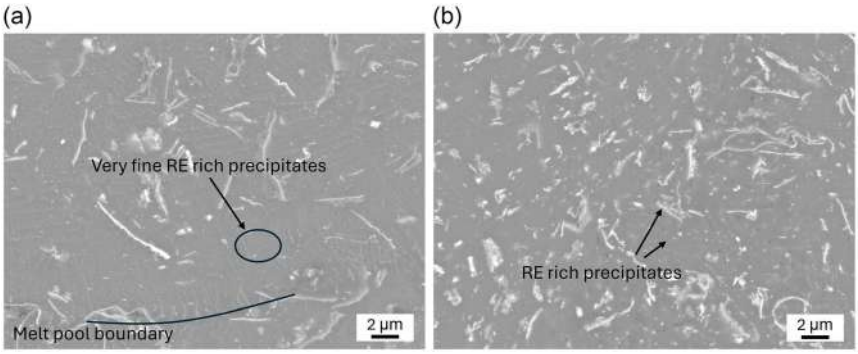

Figure 12. SEM–BSE of the node of BCC cells for: a) hatch + skywriting and b) contour strategy.

energy density of the process parameters even when the process energy of the contour strategy is about 57% higher than for the hatch strategy.

The backscatter electron micrographs from SEM analysis (**Figure 12**) show the occurrence of very small dispersed rare earth (RE) elements-rich precipitates for hatch strategy (Figure 12a). The same precipitates are observed for the contour–hatch and the hatch + skywriting. The skywriting has no influence on the occurrence of a precipitate. The presence of very small dispersed precipitations is reduced only in the area without visible boundaries of the melt pools (downskin of the struts). In the case of the contour strategy (Figure 12b), the very fine dispersed precipitates are not observed in any areas such as areas with visible melt pool boundaries and without boundaries. This can be attributed to the slower solidification of the melt pool as a result of the higher process energy. The spherical- and ribbon-shaped precipitates are contained in both the hatch strategy (Figure 12a) and the contour strategy (Figure 12b). Ribbon-shaped precipitates have a very long length compared to a width of tens of nanometers.[29] The fine microstructure has a positive effect on the mechanical performance of the material.[30] Therefore, a better performance is expected from hatch + skywriting.

Detailed SEM–EDS analyses revealed a microstructure consisting of basic matrix α-Mg precipitates rich in RE, mainly Y and Nb (**Table 5**). However, individual phases cannot be determined using this method. The chemical composition corresponds to the phases Y_2O_3, Mg_3Nd, and $Mg_{24}Y_5$ according to the literature.[29,70,71]

3.4. Mechanical Properties

The mechanical properties are determined using three samples of BCC lattice structures under quasistatic compressive loading.

Table 5. EDS results for areas highlighted in the Figure 12.

Laser strategy	Precipitate	Mg [wt%]	Y [wt%]	Nd [wt%]
Hatch + skywriting	Area of very fine particles	94.1	2.4	3.5
Contour	Ribbon	75.2	18.8	6.0
Contour	Spherical	80.8	12.3	6.9

The average maximum force and the effective elastic modulus are shown in **Table 6**. The effective elastic modulus is determined by the slope of the elastic area with a coefficient of determination greater than 0.99. The contour–hatch strategy leads to stiffer structures. The maximum force is achieved with the contour strategy, but the standard deviation is high. The laser strategy has an influence on the mechanical properties. However, the diameter of the strut must be taken into account in order to fully describe the mechanical properties.

3.5. Strut Diameter

The average strut diameters of the BCC cells produced by perspective laser strategies are listed in **Table 7**. All measured diameters are larger than the nominal diameter of 1.5 mm. This is due to the definition of the strategy when the actual diameter of the sample is not compensated with the beam compensation parameter.

The diameter of the load-bearing strut is represented by the maximum inscribed diameter. With the strategy hatch + skywriting, a smaller strut diameter is achieved than with the contour or contour–hatch strategy. This can be attributed to

Table 6. Average maximum force and average effective elastic modulus for 3 × 3 × 3 BCC lattice structures.

Laser strategy	Max force [N]	Std. deviation [N]	Effective elastic modulus [MPa]	Std. deviation [MPa]
Hatch + skywriting	3041	60.07	136.4	9.56
Contour	3788	98.29	130.7	23.31
Contour–hatch	3422	56.36	152.76	3.57

Table 7. Average strut diameter of BCC cells produced with perspective laser strategies.

Laser strategy	Maximum inscribed diameter [mm]	Std. deviation [mm]	Minimum circumscribed diameter [mm]	Std. deviation [mm]
Hatch + skywriting	1.67	0.02	3.51	0.17
Contour	1.96	0.03	3.87	0.14
Contour–hatch	1.96	0.02	4.05	0.13

the higher energy density of the process parameters, specifically 75 J mm^{-3} for the contour strategy compared to 47.62 J mm^{-3} for the hatch strategy. A higher energy of the process parameters leads to wider laser welds which influence the diameter of the strut.[17]

The minimum circumscribed diameter is 2.3–2.7 times higher than the nominal diameter. The difference between the maximum inscribed diameter and the minimum circumscribed diameter refers to the material of the strut that is not involved in load transfer. The uninvolved material on the strut is mainly related to the inclination of the struts. The downskin area is kept at the high temperature that leads to the melting of the surrounding powder particles.[25] The particles are bonded to the surface of the struts (Figure 4). This effect is magnified by the low melting temperature of the magnesium alloy.[16]

The maximum inscribed diameter is used for the FEA simulation to describe the influence of the laser strategies on the material properties. This diameter is directly related to the load transfer.

3.6. Young's Modulus of the Material

A dependence of the laser strategies on the Young's modulus is observed. The comparison of experiment and FEA is shown in **Figure 13**. The condition of convergence is fulfilled for hatch + skywriting with Young's modulus of 40 GPa, for the contour strategy with 15 GPa, and for contour–hatch with 20 GPa. The best result is achieved with hatch + skywriting (Figure 13a). The curve fits well in the elastic and plastic regions of deformation. The Young's modulus 15 GPa for the contour strategy (Figure 13b) and 20 GPa for the contour–hatch (Figure 13c) matches the experiment in the elastic region, but there is a higher deviation in the plastic region.

The Young's modulus of 40 GPa for hatch + skywriting represents 11% decrease compared to the nominal Young's modulus of magnesium alloy WE43 (44–45 GPa).[53,54] In comparison with the results of Dong et al.[48,49] the decrease in Young's modulus is not as pronounced. The authors referred to a decrease of about 30% caused by a reduction in the diameter of the test sample from 5 to 1 mm. In addition, the inclination also caused a decrease of about 12% when the inclination angle changed from 90° to 35.5°. The positive effect of hatch + skywriting is even more pronounced compared to the other strategies tested. With the contour strategy and the contour–hatch strategy, the Young's modulus decreased by 67 and 56% respectively.

The performance of hatch + skywriting can be attributed to several factors, that is, the relative material density (99.55%), the small occurrence of dangerous pores (Figure 8a), and the fine microstructure (Figure 12a). The fine microstructure consists of very small dispersed precipitates, that determine the high strength of the LBF-PB material.[30] The lower value of the Young's modulus is achieved with the contour strategy despite a higher relative density (99.11%) than in the case of

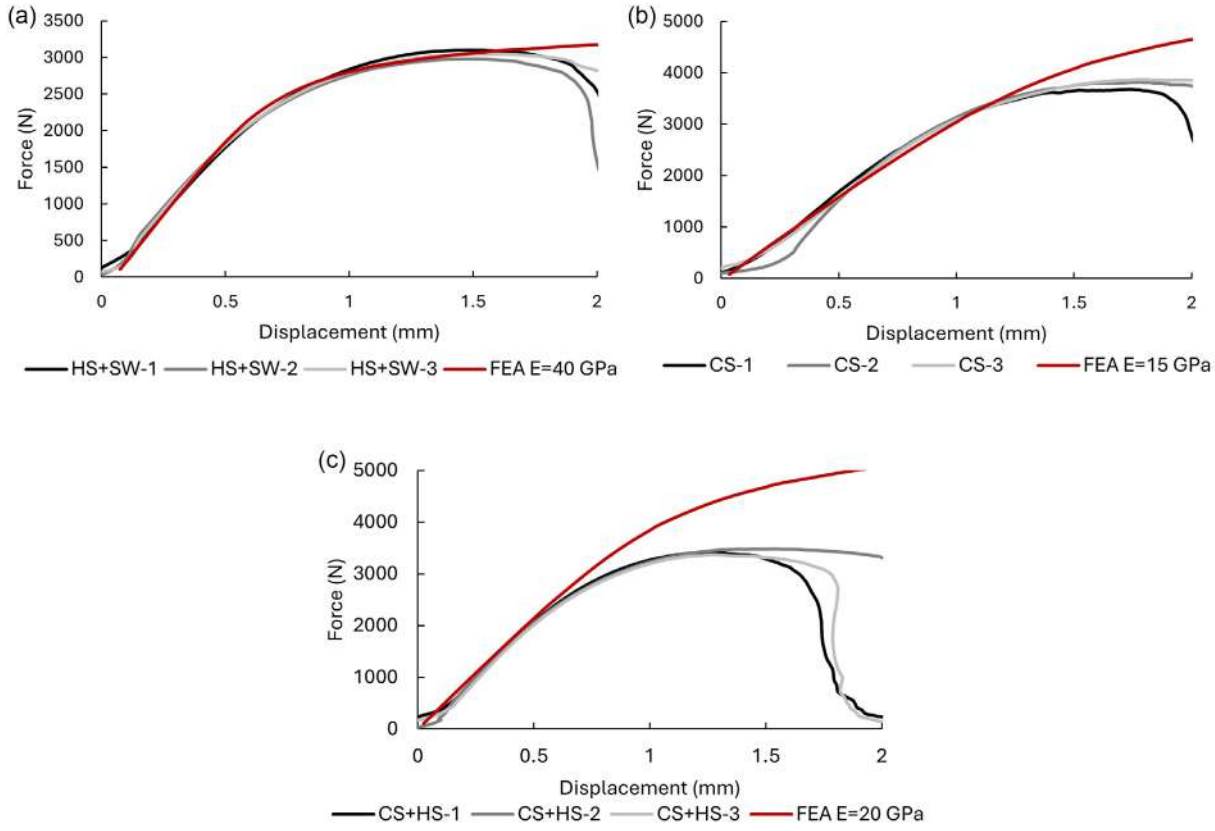

Figure 13. Comparison of experimental results with simulation of BCC lattice structures loaded in compression for: a) hatch + skywriting, b) contour, and c) contour–hatch strategies.

contour–hatch (98.67%). This can be attributed to the number of pores in the area of the node (Figure 7a), where the hatch strategy has a positive effect. The node is a critical part of the BCC structure during loading. The coarse microstructure in the node area can influence the mechanical performance of the contour strategy.[27,28,72]

3.7. Deformation Behavior

BCC lattice structures under quasistatic compressive loading show similar loading curves (**Figure 14**). The first peak is followed by the failure of the structure and densification typical of BCC structures.[73] The deformation behavior of the hatch + skywriting and the contour–hatch has the same character (Figure 14a,b,e,f). The shear failure band is caused by a fracture in the connection between the node and the strut, which is typical for bending–dominant structures.[74] However, the deformation behavior of the structure is different for the contour strategy (Figure 14c,d). The deformation occurs in one layer. Different microstructures and porosities in the nodes where the stresses accumulate during loading can have effect.[75,76] The DIC images represent the behavior of all BCC lattice structures produced with a specific laser strategy.

The combination of a microstructure without clear boundaries and a higher number of pores and irregular pores with sharp edges might have led to a different deformation behavior of the BCC lattice structures produced with the contour strategy.

4. Conclusion

The article described the influence of laser strategy on the mechanical performance of BCC lattice structures from the WE43 magnesium alloy produced by PFB-LB. Mechanical

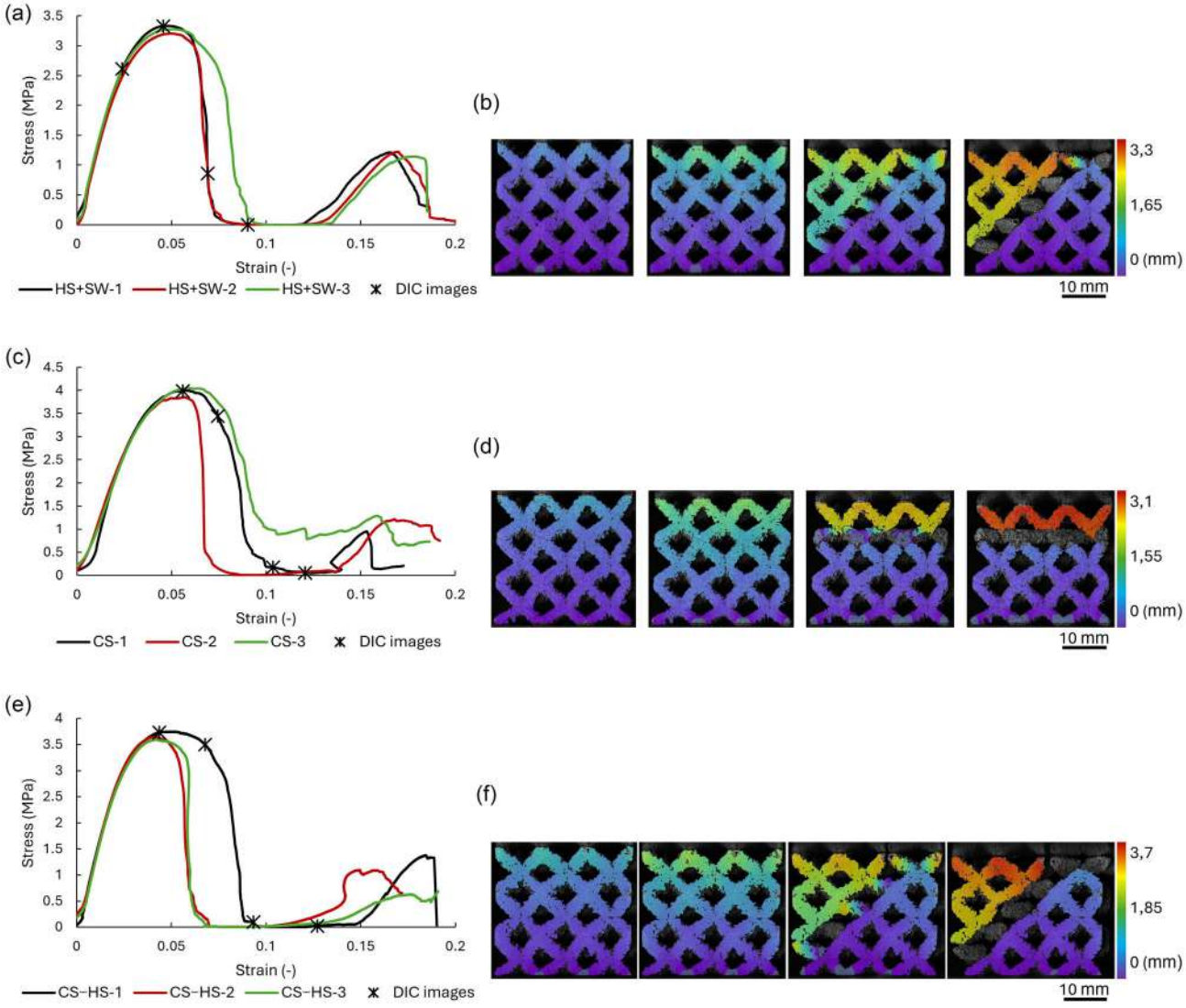

Figure 14. Engineering stress–strain curves with indicated points for DIC images of deformation in vertical direction for: a,b) hatch + skywriting, c,d) contour strategy, and e,f) contour–hatch.

performance is affected by relative material density, pore distribution, pore shape, and microstructure. In addition, the production of lattice structures requires specific process parameters in order to achieve a high relative material density, which differs depending on the laser strategy. This situation is even more critical for magnesium alloys, as the low melting temperature must be taken into account. Although the WE43 magnesium alloy was used, the authors believe that the principles could also be applicable to other materials. The following conclusions can be summarized as follows. 1) The hatch strategy with skywriting achieved Young's modulus of 40 GPa, which is about 12% lower than Young's modulus of bulk WE43. Considering the BCC lattice structure with an inclination angle is 35.26° and a diameter of 1.5 mm, the decrease is not significant compared to the literature.[48,49] The Young's modulus was determined from the FEA of the quasistatic compression testing of BCC lattice structures. The actual diameter of the strut was considered. With the contour strategy and the combination of contour and hatch strategy, a Young's modulus of 15 and 20 GPa was achieved. The effective elastic modulus from the experimental testing was 136 MPa for the hatch strategy with skywriting. 2) The mechanical performance could have been influenced by the microstructure. Clear melt pool boundaries were obtained for the hatch strategy with skywriting. Very fine RE-rich precipitates were observed, which had a positive effect on the mechanical properties. In contrast, the contour strategy led to strongly heat-affected areas without clear melt pool boundaries. The microstructure was dominated by ribbon-shaped and spherical precipitates The microstructure correlated with the energy density of the process parameters for the hatch strategy ($47.62\,J\,mm^{-3}$) and the contour strategy ($75\,J\,mm^{-3}$). 3) Although the energy density for the contour strategy was about 36% higher than for the hatch strategy, the relative material density was above 99% in both cases. This suggests that the contour and hatch strategies require different energy densities, which could be due to the alignment of the laser trajectories. Furthermore, neither energy density resulted in vaporization of the WE43 alloying elements. 4) The laser trajectories of the contour and hatch strategies also influenced pore formation and pore shape. The dangerous pores with irregular shape occurred more frequently with the contour strategy and with the combination of contour and hatch strategy. The pores were predominantly located between the laser trajectories. This could have an effect on the mechanical performance, as the Young's modulus was 62 and 50% lower than for the hatch strategy with skywriting. 5) Skywriting for the hatch strategy led to a strong reduction of pores in the subsurface area. This led to an increase in the average relative material density of 0.68% compared to the hatch strategy without skywriting. This effect is more pronounced for the lattice structures due to the the small material volume. Skywriting had no positive effect on the contour strategy. This could be due to the fact that the laser trajectories end at the same point at which they begin.

Acknowledgements

The research was funded by the project "Mechanical Engineering of Biological and Bio-inspired Systems," which was funded under the project number CZ.02.01.01/00/22_008/0004634 by the programme Johannes Amos Commenius, Excellent Research and Specific Research projects at the Brno University of Technology, no. FSI-S-23-8340 and no. CEITEC VUT/FSI-J-23-8433.

Open access publishing facilitated by Vysoke uceni technicke v Brne, as part of the Wiley - CzechELib agreement.

Conflict of Interest

The authors declare no conflict of interest.

Author Contributions

Jan Jaroš: conceptualization (lead); data curation (lead); formal analysis (lead); funding acquisition (equal); investigation (lead); methodology (lead); visualization (lead); writing—original draft (lead); writing—review & editing (lead). **Daniel Ožvoldík**: funding acquisition (equal); investigation (equal); visualization (equal); writing—original draft (supporting). **Ondřej Vaverka**: validation (equal); writing—review & editing (supporting). **Klára Nopová**: investigation (equal). **Jakub Hurník**: investigation (supporting); writing—review & editing (supporting). **Tomáš Zikmund**: supervision (equal). **Jozef Kaiser**: supervision (supporting). **Daniel Koutný**: funding acquisition (equal); supervision (equal); writing—review & editing (supporting).

Data Availability Statement

The data that support the findings of this study are openly available in [Zenodo.org] at [10.5281/zenodo.13918239], reference number [13918239].

Keywords

FEA simulation, laser beam powder bed fusion, laser strategies, lattice structures, magnesium alloy WE43, material quality mechanical properties

Received: November 8, 2024
Revised: February 15, 2025
Published online:

[1] S. Ford, M. Despeisse, *J. Clean. Prod.* **2016**, *137*, 1573.
[2] M. Attaran, *Bus. Horiz.* **2017**, *60*, 677.
[3] J. Ho, K. Leong, T. Wong, *Int. J. Therm. Sci.* **2019**, *137*, 276.
[4] I. Flores, N. Kretzschmar, A. H. Azman, S. Chekurov, D. B. Pedersen, A. Chaudhuri, *Addit. Manuf.* **2020**, *31*, 100947.
[5] S. Agnew, J. Nie, *Scr. Mater.* **2010**, *63*, 671.
[6] K. Luo, L. Zhang, G. Wu, W. Liu, W. Ding, *J. Magnesium Alloys* **2019**, *7*, 345.
[7] S. Li, X. Yang, J. Hou, W. Du, *J. Magnesium Alloys* **2020**, *8*, 78.
[8] K. Sugimoto, K. Niiya, T. Okamoto, K. Kishitake, *Trans. Jpn Inst. Met.* **1977**, *18*, 277.
[9] H. Friedrich, S. Schumann, *J. Mater. Process. Technol.* **2001**, *117*, 276.
[10] M. Easton, A. Beer, M. Barnett, C. Davies, G. Dunlop, Y. Durandet, S. Blacket, T. Hilditch, P. Beggs, *JOM* **2008**, *60*, 57.
[11] T. Kurzynowski, A. Pawlak, I. Smolina, *Arch. Civil Mech. Eng.* **2020**, *20*, 23.
[12] F. Czerwinski, *Corros. Sci.* **2014**, *86*, 1.
[13] K. Kawajiri, M. Kobayashi, K. Sakamoto, *J. Clean. Prod.* **2020**, *253*, 119805.
[14] L. E. Erickson, *Environ. Prog. Sustainable Energy* **2017**, *36*, 982.

[15] G. E. J. Poinern, S. Brundavanam, D. Fawcett, *Am. J. Biomed. Eng.* **2013**, *2*, 218.
[16] A. Pawlak, M. Rosienkiewicz, E. Chlebus, *Arch. Civil Mech. Eng.* **2017**, *17*, 9.
[17] J. Suchy, M. Horynova, L. Klakurkova, D. Palousek, D. Koutny, L. Celko, *Materials* **2020**, *13*, 2623.
[18] K. Wei, M. Gao, Z. Wang, X. Zeng, *Mater. Sci. Eng. A* **2014**, *611*, 212.
[19] B. Zhang, H. Liao, C. Coddet, *Mater. Des.* **2012**, *34*, 753.
[20] B. Song, S. Dong, S. Deng, H. Liao, C. Coddet, *Opt. Laser Technol.* **2014**, *56*, 451.
[21] X. Cao, M. Jahazi, J. Immarigeon, W. Wallace, *J. Mater. Process. Technol.* **2006**, *171*, 188.
[22] E. Li, Z. Zhou, L. Wang, R. Zou, A. Yu, *Powder Technol.* **2022**, *409*, 117789.
[23] N. Ahmed, I. Barsoum, G. Haidemenopoulos, R. A. Al-Rub, *J. Manuf. Process.* **2022**, *75*, 415.
[24] R. Vrana, J. Jaros, D. Koutny, J. Nosek, T. Zikmund, J. Kaiser, D. Palousek, *J. Magnesium Process.* **2022**, *74*, 640.
[25] P. Delroisse, P. J. Jacques, E. Maire, O. Rigo, A. Simar, *Scr. Mater.* **2017**, *141*, 32.
[26] J. C. Snyder, K. A. Thole, *J. Manuf. Sci. Eng.* **2020**, *142*, 071003.
[27] T. Ronneberg, C. M. Davies, P. A. Hooper, *Mater. Des.* **2020**, *189*, 108481.
[28] M. Esmaily, Z. Zeng, A. Mortazavi, A. Gullino, S. Choudhary, T. Derra, F. Benn, F. D'Elia, M. Müther, S. Thomas, A. Huang, A. Allanore, A. Kopp, N. Birbilis, *Addit. Manuf.* **2020**, *35*, 101321.
[29] F. Guaglione, L. Caprio, B. Previtali, A. G. Demir, *Addit. Manuf.* **2021**, *48*, 102426.
[30] W. Shifeng, L. Shuai, W. Qingsong, C. Yan, Z. Sheng, S. Yusheng, *J. Mater. Process. Technol.* **2014**, *214*, 2660.
[31] N. Nadammal, T. Mishurova, T. Fritsch, I. Serrano-Munoz, A. Kromm, C. Haberland, P. D. Portella, G. Bruno, *Addit. Manuf.* **2021**, *38*, 101792.
[32] S. Pauly, C. Schricker, S. Scudino, L. Deng, U. Kühn, *Mater. Des.* **2017**, *135*, 133.
[33] T. Gustmann, A. Neves, U. Kühn, P. Gargarella, C. Kiminami, C. Bolfarini, J. Eckert, S. Pauly, *Addit. Manuf.* **2016**, *11*, 23.
[34] E. Malekipour, H. El-Mounayri, *Volume 2A: Advanced Manufacturing* **2020**, V02AT02A055.
[35] X. Yang, G. J. Gibbons, D. A. Tanner, Z. Li, P. Wilson, M. A. Williams, H. R. Kotadia, *Mater. Des.* **2023**, *232*, 112160.
[36] A. Mancisidor, F. Garciandia, M. S. Sebastian, P. Álvarez, J. Díaz, I. Unanue, *Phys. Procedia* **2016**, *83*, 864.
[37] R. Vrána, D. Koutný, D. Paloušek, L. Pantělejev, J. Jaroš, T. Zikmund, J. Kaiser, *Materials* **2018**, *11*, 1763.
[38] J. Jaros, O. Vaverka, S. Senck, D. Koutny, *Micromachines* **2024**, *15*, 278.
[39] L. J. Gibson, M. F. Ashby, *Cellular Solids*, Cambridge University Press, Cambridge **1997**.
[40] X. Yue, J. Shang, M. Zhang, B. Hur, X. Ma, *Mater. Sci. Eng. A* **2022**, *859*, 144167.
[41] M. Ashby, *Philos. Trans. R. Soc. A: Math. Phys. Eng. Sci.* **2005**, *364*, 15.
[42] G. Campoli, M. Borleffs, S. A. Yavari, R. Wauthle, H. Weinans, A. Zadpoor, *Mater. Des.* **2013**, *49*, 957.
[43] K. Cwieka, B. Wysocki, J. Skibinski, A. Chmielewska, W. Swieszkowski, *J. Mech. Behav. Biomed. Mater.* **2024**, *151*, 106359.
[44] M. Leary, M. Mazur, J. Elambasseril, M. McMillan, T. Chirent, Y. Sun, M. Qian, M. Easton, M. Brandt, *Mater. Des.* **2016**, *98*, 344.
[45] J. C. Maxwell, *Lond. Edinb. Dubl. Phil. Mag. J. Sci.* **1864**, *27*, 294.
[46] V. Deshpande, M. Ashby, N. Fleck, *Acta Mater.* **2001**, *49*, 1035.
[47] Y. Tian, D. Tomus, P. Rometsch, X. Wu, *Addit. Manuf.* **2017**, *13*, 103.
[48] Z. Dong, X. Zhang, W. Shi, H. Zhou, H. Lei, J. Liang, *Materials* **2018**, *11*, 2463.
[49] Z. Dong, Y. Liu, W. Li, J. Liang, *J. Alloys Compd.* **2019**, *791*, 490.
[50] S. Tsopanos, R. A. W. Mines, S. McKown, Y. Shen, W. J. Cantwell, W. Brooks, C. J. Sutcliffe, *J. Manuf. Sci. Eng.* **2010**, *132*, 041011.
[51] O. Červinek, B. Werner, D. Koutný, O. Vaverka, L. Pantělejev, D. Paloušek, *Materials* **2021**, *14*, 2462.
[52] O. Vaverka, O. Cervinek, J. Jaros, D. Koutny, L. Pantelejev, *Adv. Eng. Mater.* **2024**, *26*, 2400127.
[53] M. Jahedi, B. A. McWilliams, P. Moy, M. Knezevic, *Acta Mater.* **2017**, *113*, 221.
[54] G. Mani, M. D. Feldman, D. Patel, C. M. Agrawal, *Biomaterials* **2007**, *28*, 1689.
[55] J. Jan, V. Ondřej, S. Sascha, K. Daniel, [Data set], *Zenodo* **2023**, https://doi.org/10.5281/zenodo.10154211.
[56] D. Manfredi, F. Calignano, M. Krishnan, R. Canali, E. Paola, S. Biamino, D. Ugues, M. Pavese, P. Fino, *Light Metal Alloys Applications*, IntechOpen, London, UK **2014**.
[57] S. Moylan, J. Slotwinski, A. Cooke, K. Jurrens, M. A. Donmez, *J. Res. Natl. Inst. Stand. Technol.* **2014**, *119*, 429.
[58] N. Otsu, *IEEE Trans. Syst. Man Cybern.* **1979**, *9*, 62.
[59] A. du Plessis, P. Sperling, A. Beerlink, W. B. du Preez, S. G. le Roux, *MethodsX* **2018**, *5*, 1336.
[60] H. Wadell, *J. Geol.* **1932**, *40*, 443.
[61] N. Nudelis, P. Mayr, *Metals* **2021**, *11*, 1912.
[62] A. Barylski, K. Aniołek, G. Dercz, I. Matuła, S. Kaptacz, J. Rak, R. Paszkowski, *Materials* **2024**, *17*, 2011.
[63] K. Kempen, L. Thijs, J. V. Humbeeck, J.-P. Kruth, *Phys. Procedia* **2012**, *39*, 439.
[64] E. Li, Z. Zhou, L. Wang, Q. Zheng, R. Zou, A. Yu, *Powder Technol.* **2022**, *405*, 117533.
[65] Y. Qin, P. Wen, H. Guo, D. Xia, Y. Zheng, L. Jauer, R. Poprawe, M. Voshage, J. H. Schleifenbaum, *Acta Biomater.* **2019**, *98*, 3.
[66] Z. Li, Y. Jing, H. Guo, X. Sun, K. Yu, A. Yu, X. Jiang, X. J. Yang, *Metall. Mater. Trans. B* **2019**, *50*, 1204.
[67] R. Jiang, D. Bull, A. Evangelou, A. Harte, F. Pierron, I. Sinclair, M. Preuss, X. Hu, P. Reed, *Int. J. Fatigue* **2018**, *114*, 22.
[68] Y. Shi, K. Guo, H. Shi, X. Huang, B. Yang, J. Sun, *Mater. Today Commun.* **2024**, *39*, 109151.
[69] W. Xu, J. Li, Z. Zhang, H. Yuan, G. An, H. Shi, C. Cai, W. Jiang, W. Li, Q. Wei, *J. Magnesium Alloys* **2024**, https://doi.org/10.1016/j.jma.2024.03.012.
[70] S. Gangireddy, B. Gwalani, K. Liu, E. J. Faierson, R. S. Mishra, *Addit. Manuf.* **2019**, *26*, 53.
[71] H. Hyer, L. Zhou, G. Benson, B. McWilliams, K. Cho, Y. Sohn, *Addit. Manuf.* **2020**, *33*, 101123.
[72] J. Yang, J. Han, H. Yu, J. Yin, M. Gao, Z. Wang, X. Zeng, *Mater. Des.* **2016**, *110*, 558.
[73] B. Hanks, J. Berthel, M. Frecker, T. W. Simpson, *Addit. Manuf.* **2020**, *35*, 101301.
[74] H. Lei, C. Li, X. Zhang, P. Wang, H. Zhou, Z. Zhao, D. Fang, *Addit. Manuf.* **2021**, *37*, 101674.
[75] M. Araghi, H. Rokhgireh, A. Nayebi, *Mater. Des.* **2023**, *232*, 112125.
[76] M. Isaenkova, A. Yudin, A. Rubanov, A. Osintsev, L. Degadnikova, *J. Mater. Res. Technol.* **2020**, *9*, 15177.

7 CONCLUSIONS

The thesis focused on the development of PBF-LB process parameters for the production of lattice structures from lightweight materials. The scientific questions addressing the main problems were identified based on the literature review. The PBF-LB process parameters and laser strategies should have been considered for the fabrication of lattice structures from materials such as aluminum and magnesium alloys.

In the literature, the studies describe the effects of the PBF-LB process parameters on the quality of the lattice structures, usually using materials that are easy to process such as aluminum alloys. The negative effects of low volume and strut inclination have also been described. However, the process for achieving high relative material density of lattice structures within the wide range of strut diameters was not described. Furthermore, the production of magnesium alloy lattice structures was not described. The geometry of lattice structures seems to be suitable for contour strategy using circumscribed laser trajectories, therefore the effect on the reduction of imperfections should be analyzed.

In the first phase of this thesis, the contour strategy was used for the production of vertical and inclined struts representing the geometry of lattice structures made of the aluminum alloy AlSi10Mg. It was shown that the contour strategy can lead to a relative material density of over 99.8% and achieves better results in terms of surface roughness and dimensional accuracy than the hatch (meander) strategy with the process parameters recommended by the powder manufacturer. The circumscribed laser trajectories of the contour strategy fit well with the circular or elliptical cross-sections of the vertical and inclined struts. In order to obtain struts with minimum imperfections, the selection of the PBF-LB process parameters had to be taken into account. In the case of the contour strategy, the overlap between two laser trajectories was crucial. The value of 35% proved to be suitable to reduce porosity. The determination of the hatch distance from the overlap was based on the weld width, the energy of the process parameters and the inclination of the struts. The weld width was measured on hollow struts with the same strut diameter to represent real production conditions. In order to achieve high dimensional accuracy, the beam distance parameter was set to 1/3 of the weld width.

In the second phase, the contour strategy was used for the production of BCCZ cells from a WE43 magnesium alloy. The relative material density of over 99.8% was achieved for BCCZ cells with diameters of 0.5 and 1 mm. The selection of process parameters was based on the results of a previous study. The hollow struts were used to determine the actual weld width. However, various suitable overlap values in the range of 45-80% was determined, depending on the input energy of the PBF-LB process parameters and the strut diameter. Due to the narrow range of 450° between the melting and boiling points of the magnesium alloy, the energy of the PBF-LB process was partially dissipated by the surrounding powder particles. This resulted in a surface roughness Ra between 30-64 μm depending on the strut diameter and inclination. Also, the deviation of the maximum inscribed diameter was between 4-44% and the deviation of the minimum inscribed diameter reached a maximum value of 3.5 times the nominal diameter. However, high relative material density was achieved in BCCZ cells with strut diameters of 0.5 and 1 mm, while diameters of 2 and 3 mm resulted in irregular open pores, probably due to problems associated with magnesium alloy processing. The node of the cell also exhibited irregular pores due to sharp edges in the laser trajectories for contour strategy.

The third phase therefore focused on the BCC lattice structures with a diameter of 1.5 mm from the WE43 magnesium alloy. The different laser strategies were used to achieve high relative material density and to determine the influence of PBF-LB production on mechanical performance. The relative material density of over 99% was achieved with the contour strategy, the combination of contour and hatch strategy and hath strategy with skywriting. The contour strategy led to a higher occurrence of pores in the cell nodes, therefore the combination of both strategies was used, i.e. the contour strategy for the struts and the hatch strategy for the nodes. The effective elastic modulus from the compression test of the BCC lattice structures was 130 MPa for the contour strategy, 136 MPa for the hatch strategy with skywriting and 152 MPa for the combination of both strategies. However, the effective elastic modulus did not take into account the actual diameter of the struts. Therefore, the Young's modulus of material was determined from the FEA using the maximum inscribed diameter and the results of the compressive loading. The Young's modulus of 40 GPa was achieved using the hatch strategy with skywriting. This laser strategy reduced the occurrence of dangerous pores in the material of the lattice structures and the microstructure showed very fine areas rich in rare elements, which contributed to the mechanical performance. The lower Young's modulus of 15 GPa was achieved with the contour strategy. The combination of both strategies led to a Young's modulus of 20 GPa.

Based on the tested hypothesis, the results can be summarized in the following conclusions:

Q1 Does the contour strategy lead to a reduction of imperfections such as material porosity, dimensional inaccuracy and rough surface that occur during PBF-LB production of lattice structures compared to the commonly used process parameters?

Optimization of the PBF-LB process parameters for the contour strategy resulted in a relative material density of over 99.8% for a wide range of strut diameters from 0.6-3 mm. The hatch strategy achieved a lower relative material density, except for inclined struts with diameters of 0.6 mm and 0.7 mm, where the laser trajectories were formed by only one contour. The median value of the dimensional deviation was 0.03 mm for inclined struts and 0.04 mm for vertical struts. The surface roughness Ra was reduced with the contour strategy, but the values were dependent on the energy of the PBF-LB process parameters. The contour strategy reduced imperfection during PBF-LB production, but required individual adjustment of process parameters for input energy, strut diameter and strut orientation. **Thus, the first hypothesis was not falsified.**

Q2 Does the contour strategy result in a relative material density of over 99.5% for lattice structures when using the magnesium alloy WE43?

The contour strategy resulted in a relative material density of over 99.8 % for WE43 magnesium alloy BCCZ cells with diameters of 0.5 mm and 1 mm produced with PBF-LB. Specific selection of process parameters based on input energy, strut diameter and strut orientation was used. Using the same approach to optimize the process parameters, the 2 mm and 3 mm strut diameters exhibited severe open pores due to the difficult processing of the magnesium alloy. The relative material density was therefore lower than 99.5% in these cases. In addition, the irregular pores were identified in the junction of the BCCZ cells where the contour strategy resulted in sharp laser trajectories. The relative material density above 99.5% was achieved at diameters of 0.5 mm and 1 mm, but diameters of 2 mm and 3 mm resulted in lower values. **The second hypothesis was therefore not falsified.**

Q3 Does the contour strategy improve the mechanical performance of the lattice structures compared to the hatch strategy for WE43 magnesium alloy?

The contour strategy and the hatch strategy with skywriting achieved a relative material density of over 99.1% and 99.5%, respectively. The compression test of BCC lattice structures produced with the PBF-LB technology from the magnesium alloy WE 43 resulted in an effective elastic modulus of 130 MPa for the contour and 136 MPa for the hatch strategy with skywriting. Taking into account the actual diameter of the struts, the Young's modulus was determined from the FEA and the results of the compressive load. The contour strategy achieved Young's modulus of 15 GPa. The hatch strategy with skywriting achieved Young's modulus of 40 GPa. The main factors for the better performance of the hatch strategy with skywriting were the fewer dangerous pores and the fine microstructure. Skywriting reduced the dangerous pores that accumulated near the surface as well as the pores in the nodes of the cells. **The third hypothesis was therefore falsified.**

8 LIST OF PUBLICATIONS

8.1 Papers published in journals with impact factor

VRÁNA, R.; KOUTNÝ, D.; PALOUŠEK, D.; PANTĚLEJEV, L.; JAROŠ, J.; ZIKMUND, T.; KAISER, J. Selective Laser Melting Strategy for Fabrication of Thin Struts Usable in Lattice Structures. *Materials,* 2018, vol. 11, no. 9, p. 1-20. ISSN: 1996-1944.

VRÁNA, R.; JAROŠ, J.; KOUTNÝ, D.; NOSEK, J.; ZIKMUND, T.; KAISER, J.; PALOUŠEK, D. Contour laser strategy and its benefits for lattice structure manufacturing by selective laser melting technology. *Journal of Manufacturing Processes,* 2022, vol. 74, no. 1, p. 640-657. ISSN: 1526-6125.

SLAVÍČEK, J.; FRANKE, J.; JAROŠ, J.; KOUTNÝ, D. Strategies for wire arc additive manufacturing of thin walls and overhangs. *Journal of Mechanical Science and Technology,* 2023, vol. 37, no. 1, p. 5529-5534. ISSN: 1738-494X.

NOPOVÁ, K.; JAROŠ, J.; ČERVINEK, O.; PANTĚLEJEV, L.; GNEIGER, S.; SENCK, S.; KOUTNÝ, D. Processing of AZ91D Magnesium Alloy by Laser Powder Bed Fusion. *Applied Sciences - Basel,* 2023, vol. 13, no. 1, ISSN: 2076-3417.

JAROŠ, J.; KOUTNÝ, D.; KLAKURKOVÁ, L.; GNEIGER, S.; SENCK, S. Ultrasonic atomization of magnesium alloy AZ61 based on the TIG melting method. *Journal of Mechanical Science and Technology,* 2023, vol. 37, no. 10, ISSN: 1976-3824.

VAVERKA, O.; ČERVINEK, O.; JAROŠ, J.; KOUTNÝ, D.; PANTĚLEJEV, L. Numerical and Experimental Evaluation of Structured Material for Use in Multi-scale Topology Optimization. *Advanced Engineering Materials,* 2024, vol. 26, no. 13, p. 1-10. ISSN: 1527-2648.

JAROŠ, J.; VAVERKA, O.; SENCK, S.; KOUTNÝ, D. Influence of Process Energy on the Formation of Imperfections in Body-Centered Cubic Cells with Struts in the Vertical Orientation Produced by Laser Powder Bed Fusion from the Magnesium Alloy WE43. *Micromachines,* 2024, vol. 15, no. 2, p. 1-16. ISSN: 2072-666X.

MINÁRIK, P.; ZEMKOVÁ, M.; ŠAŠEK, S.; DITTRICH, J.; KNAPEK, M.; LUKÁČ, F.; KOUTNÝ, D.; JAROŠ, J.; KRÁL, R. Comparative analysis of microstructure, mechanical, and corrosion properties of biodegradable Mg-3Y alloy prepared by selective laser melting and spark plasma sintering. *Journal of Magnesium and Alloys,* 2024, vol. 12, no. 4, p. 1496-1510. ISSN: 2213-9567.

JAROŠ, Jan; OŽVOLDÍK, Daniel; VAVERKA, Ondřej; NOPOVÁ, Klára; HURNÍK, Jakub. Influence of Laser Strategies on Performance of Lattice Structures from Magnesium Alloy WE43 Produced by Laser Beam Powder Bed Fusion. Online, *Advanced Engineering Materials*, 2025, ISSN 1438-1656

8.2 Conference contribution

JAROŠ, J.; DUCHOŇ, M.; VÍCHA, D.; PCHÁLEK, V.; ŠVÁB, Č.; KOUTNÝ, D. *TiAl6V4 bistable mechanism produced by Laser Powder Bed Fusion.*

8.3 Other results

Software (RIV-R) – *SLM Contour Strategy Checker 1.0*

Functional specimen (RIV-G) – *Intramedullary bone canal plug; Porous biodegradable WE43 alloy implant*

Functional specimen (RIV-G) – *Intramedullary bone canal plug; Biodegradable WE43 alloy implant with a bulk core and porous surface layer*

Functional specimen (RIV-G) – *Intramedullary bone canal plug; Biodegradable implant made of bulky metal material*

Functional specimen (RIV-G) – *Additively manufactured aluminium alloy heat sink with electrochemically smoothed surface*

9 LITERATURE

[1] WONG, Kaufui V. and HERNANDEZ, Aldo. A Review of Additive Manufacturing. *ISRN Mechanical Engineering*. 16 August 2012. Vol. 2012, p. 1–10. DOI 10.5402/2012/208760.

[2] BHUVANESH KUMAR, M. and SATHIYA, P. *Methods and materials for additive manufacturing: A critical review on advancements and challenges*. 1 February 2021. Elsevier Ltd.

[3] GALY, Cassiopée, LE GUEN, Emilie, LACOSTE, Eric and ARVIEU, Corinne. *Main defects observed in aluminum alloy parts produced by SLM: From causes to consequences*. 1 August 2018. Elsevier B.V.

[4] ABOULKHAIR, Nesma T., EVERITT, Nicola M., ASHCROFT, Ian and TUCK, Chris. Reducing porosity in AlSi10Mg parts processed by selective laser melting. *Additive Manufacturing*. 1 October 2014. Vol. 1, p. 77–86. DOI 10.1016/j.addma.2014.08.001.

[5] MAAMOUN, Ahmed H., XUE, Yi F., ELBESTAWI, Mohamed A. and VELDHUIS, Stephen C. Effect of selective laser melting process parameters on the quality of al alloy parts: Powder characterization, density, surface roughness, and dimensional accuracy. *Materials*. 2018. Vol. 11, no. 12. DOI 10.3390/ma11122343.

[6] PAULY, S., SCHRICKER, C., SCUDINO, S., DENG, L. and KÜHN, U. Processing a glass-forming Zr-based alloy by selective laser melting. *Materials & Design*. December 2017. Vol. 135, p. 133–141. DOI 10.1016/j.matdes.2017.08.070.

[7] OLAKANMI, E. O., COCHRANE, R. F. and DALGARNO, K. W. A review on selective laser sintering/melting (SLS/SLM) of aluminium alloy powders: Processing, microstructure, and properties. *Progress in Materials Science*. Online. 2015. Vol. 74, p. 401–477. DOI 10.1016/j.pmatsci.2015.03.002.

[8] DAS, Suman. Physical Aspects of Process Control in Selective Laser Sintering of Metals. *Advanced Engineering Materials*. 2003. Vol. 5, no. 10, p. 701–711. DOI 10.1002/adem.200310099.

[9] GU, D. D., MEINERS, W., WISSENBACH, K. and POPRAWE, R. Laser additive manufacturing of metallic components: Materials, processes and mechanisms. *International Materials Reviews*. 2012. Vol. 57, no. 3, p. 133–164. DOI 10.1179/1743280411Y.0000000014.

[10] AGARWALA, Mukesh, BOURELL, David, BEAMAN, Joseph, MARCUS, Harris and BARLOW, Joel. Direct selective laser sintering of metals. *Rapid Prototyping Journal*. 1995. Vol. 1, no. 1, p. 26–36. DOI 10.1108/13552549510078113.

[11] NIU, H. J. and CHANG, I. T.H. Selective laser sintering of gas atomized M2 high speed steel powder. *Journal of Materials Science*. 2000. Vol. 35, no. 1, p. 31–38. DOI 10.1023/A:1004720011671.

[12] WANG, Xiaoqing, GONG, Xibing and CHOU, Kevin. Review on powder-bed laser additive manufacturing of Inconel 718 parts. *Proceedings of the Institution of Mechanical Engineers, Part B: Journal of Engineering Manufacture*. 2017. Vol. 231, no. 11, p. 1890–1903. DOI 10.1177/0954405415619883.

[13] LIU, Jianli, YU, Huijun, CHEN, Chuanzhong, WENG, Fei and DAI, Jingjie. Research and development status of laser cladding on magnesium alloys: A review. *Optics and Lasers in Engineering*. Online. 2017. Vol. 93, no. November 2016, p. 195–210. DOI 10.1016/j.optlaseng.2017.02.007.

[14] WANG, Lin zhi, WANG, Sen and HONG, Xingfu. Pulsed SLM-manufactured AlSi10Mg alloy: Mechanical properties and microstructural effects of designed laser energy densities. *Journal of Manufacturing Processes*. Online. 2018. Vol. 35, no. November 2017, p. 492–499. DOI 10.1016/j.jmapro.2018.09.007.

[15] ZHANG, Dongyun, WANG, Weidong, GUO, Yanwu, HU, Songtao, DONG, Dongdong, POPRAWE, Reinhart, SCHLEIFENBAUM, Johannes Henrich and ZIEGLER, Stephan. Numerical simulation in the absorption behavior of Ti6Al4V powder materials to laser energy during SLM. *Journal of Materials Processing Technology*. Online. 2019. Vol. 268, no. 100, p. 25–36. DOI 10.1016/j.jmatprotec.2019.01.002.

[16] VRÁNA, Radek, KOUTNÝ, Daniel, PALOUŠEK, David, PANTĚLEJEV, Libor, JAROŠ, Jan, ZIKMUND, Tomáš and KAISER, Jozef. Selective laser melting strategy for fabrication of thin struts usable in lattice structures. *Materials*. 18 September 2018. Vol. 11, no. 9. DOI 10.3390/ma11091763.

[17] BIFFI, C. A., FIOCCHI, J. and TUISSI, A. Selective laser melting of AlSi10 Mg: Influence of process parameters on Mg2Si precipitation and Si spheroidization. *Journal of Alloys and Compounds*. 2018. Vol. 755, p. 100–107. DOI 10.1016/j.jallcom.2018.04.298.

[18] ZHOU, Xin, LIU, Xihe, ZHANG, Dandan, SHEN, Zhijian and LIU, Wei. Balling phenomena in selective laser melted tungsten. *Journal of Materials Processing Technology*. Online. 2015. Vol. 222, p. 33–42. DOI 10.1016/j.jmatprotec.2015.02.032.

[19] NAZIR, Aamer, ABATE, Kalayu Mekonen, KUMAR, Ajeet and JENG, Jeng Ywan. A state-of-the-art review on types, design, optimization, and additive manufacturing of cellular structures. *International Journal of Advanced Manufacturing Technology*. 2019. Vol. 104, no. 9–12, p. 3489–3510. DOI 10.1007/s00170-019-04085-3.

[20] GIBSON, Lorna J. The hierarchical structure and mechanics of plant materials. *Journal of the Royal Society Interface*. 2012. Vol. 9, no. 76, p. 2749–2766. DOI 10.1098/rsif.2012.0341.

[21] SARANATHAN, Vinodkumar, OSUJI, Chinedum O., MOCHRIE, Simon G.J., NOH, Heeso, NARAYANAN, Suresh, SANDY, Alec, DUFRESNE, Eric R. and PRUM, Richard O. Structure, function, and self-assembly of single network gyroid (I4 132) photonic crystals in butterfly wing scales. *Proceedings of the National Academy of Sciences of the United States of America*. 2010. Vol. 107, no. 26, p. 11676–11681. DOI 10.1073/pnas.0909616107.

[22] HO, J.Y., LEONG, K.C. and WONG, T.N. Experimental and numerical investigation of forced convection heat transfer in porous lattice structures produced by selective laser melting. *International Journal of Thermal Sciences*. March 2019. Vol. 137, p. 276–287. DOI 10.1016/j.ijthermalsci.2018.11.022.

[23] FLORES, Iñigo, KRETZSCHMAR, Niklas, AZMAN, Abdul Hadi, CHEKUROV, Sergei, PEDERSEN, David Bue and CHAUDHURI, Atanu. Implications of lattice structures on economics and productivity of metal powder bed fusion. *Additive Manufacturing*. January 2020. Vol. 31, p. 100947. DOI 10.1016/j.addma.2019.100947.

[24] GALY, Cassiopée, LE GUEN, Emilie, LACOSTE, Eric and ARVIEU, Corinne. Main defects observed in aluminum alloy parts produced by SLM: From causes to consequences. *Additive Manufacturing*. Online. 2018. Vol. 22, no. July 2017, p. 165–175. DOI 10.1016/j.addma.2018.05.005.

[25] YAN, Chunze, HAO, Liang, HUSSEIN, Ahmed, BUBB, Simon Lawrence, YOUNG, Philippe and RAYMONT, David. Evaluation of light-weight AlSi10Mg periodic cellular lattice structures fabricated via direct metal laser sintering. *Journal of Materials Processing Technology*. Online. 2014. Vol. 214, no. 4, p. 856–864. DOI 10.1016/j.jmatprotec.2013.12.004.

[26] LEARY, Martin, MAZUR, Maciej, ELAMBASSERIL, Joe, MCMILLAN, Matthew, CHIRENT, Thomas, SUN, Yingying, QIAN, Ma, EASTON, Mark and BRANDT, Milan. Selective laser melting (SLM) of AlSi12Mg lattice structures. *Materials & Design*. May 2016. Vol. 98, p. 344–357. DOI 10.1016/j.matdes.2016.02.127.

[27] DELROISSE, Pauline, JACQUES, Pascal J., MAIRE, Eric, RIGO, Olivier and SIMAR, Aude. Effect of strut orientation on the microstructure heterogeneities in AlSi10Mg lattices processed by selective laser melting. *Scripta Materialia*. December 2017. Vol. 141, p. 32–35. DOI 10.1016/j.scriptamat.2017.07.020.

[28] LIU, Mulin, TAKATA, Naoki, SUZUKI, Asuka and KOBASHI, Makoto. Microstructural characterization of cellular AlSi10Mg alloy fabricated by selective laser melting. *Materials and Design*. Online. 2018. Vol. 157, p. 478–491. DOI 10.1016/j.matdes.2018.08.005.

[29] DONG, Zhichao, ZHANG, Xiaoyu, SHI, Wenhua, ZHOU, Hao, LEI, Hongshuai and LIANG, Jun. Study of size effect on microstructure and mechanical properties of AlSi10Mg samples made by selective laser melting. *Materials*. 2018. Vol. 11, no. 12. DOI 10.3390/ma11122463.

[30] QIU, Chunlei, YUE, Sheng, ADKINS, Nicholas J.E., WARD, Mark, HASSANIN, Hany, LEE, Peter D., WITHERS, Philip J. and ATTALLAH, Moataz M. Influence of processing conditions on strut structure and compressive properties of cellular lattice structures fabricated by selective laser melting. *Materials Science and Engineering: A*. 5 March 2015. Vol. 628, p. 188–197. DOI 10.1016/j.msea.2015.01.031.

[31] PEI, Wei, ZHENGYING, Wei, ZHEN, Chen, JUNFENG, Li, SHUZHE, Zhang and JUN, Du. Numerical simulation and parametric analysis of selective laser melting process of AlSi10Mg powder. *Applied Physics A: Materials Science and Processing*. 2017. Vol. 123, no. 8, p. 1–15. DOI 10.1007/s00339-017-1143-7.

[32] LOUVIS, Eleftherios, FOX, Peter and SUTCLIFFE, Christopher J. Selective laser melting of aluminium components. *Journal of Materials Processing Technology*. Online. 2011. Vol. 211, no. 2, p. 275–284. DOI 10.1016/j.jmatprotec.2010.09.019.

[33] GROSSMANN, Alexander, MÖLLENEY, Jan, FRÖLICH, Tilman, MERSCHROTH, Holger, FELGER, Julian, WEIGOLD, Matthias, SIELAFF, Axel and MITTELSTEDT, Christian. Dimensionless process development for lattice structure design in laser powder bed fusion. *Materials and Design*. 2020. Vol. 194, p. 1–16. DOI 10.1016/j.matdes.2020.108952.

[34] LI, Zixin, JING, Yuhai, GUO, Hongmin, SUN, Xiuyuan, YU, Kun, YU, Anshan, JIANG, Xingwang and YANG, X. J. Study of 3D Pores and Its Relationship with Crack Initiation Factors of Aluminum Alloy Die Castings. *Metallurgical and Materials Transactions B*. 15 June 2019. Vol. 50, no. 3, p. 1204–1212. DOI 10.1007/s11663-019-01550-y.

[35] JIANG, R., BULL, D.J., EVANGELOU, A., HARTE, A., PIERRON, F., SINCLAIR, I., PREUSS, M., HU, X.T. and REED, P.A.S. Strain accumulation and fatigue crack initiation at pores and carbides in a SX superalloy at room temperature. *International Journal of Fatigue*. September 2018. Vol. 114, p. 22–33. DOI 10.1016/j.ijfatigue.2018.05.003.

[36] NUDELIS, Natan and MAYR, Peter. A Novel Classification Method for Pores in Laser Powder Bed Fusion. *Metals*. 26 November 2021. Vol. 11, no. 12, p. 1912. DOI 10.3390/met11121912.

[37] HAN, Xuesong, ZHU, Haihong, NIE, Xiaojia, WANG, Guoqing and ZENG, Xiaoyan. Investigation on Selective Laser Melting AlSi10Mg Cellular Lattice Strut: Molten Pool Morphology, Surface Roughness and Dimensional Accuracy. *Materials*. 7 March 2018. Vol. 11, no. 3, p. 392. DOI 10.3390/ma11030392.

[38] TIAN, Yang, TOMUS, Dacian, ROMETSCH, Paul and WU, Xinhua. Influences of processing parameters on surface roughness of Hastelloy X produced by selective laser melting. *Additive Manufacturing*. January 2017. Vol. 13, p. 103–112. DOI 10.1016/j.addma.2016.10.010.

[39] VRÁNA, Radek, KOUTNÝ, Daniel, PALOUŠEK, David and ZIKMUND, Tomáš. Influence of Selective Laser Melting Process Parameters on Impact Resistance of Lattice Structure made from AlSi10Mg. In : *World PM2016 Proceedings*. Hamburk, 2016. p. 6. DOI ISBN: 978-1-899072-48-4.

[40] VRANA, Radek, VAVERKA, Ondrej, KOUTNY, Daniel, DOCEKALOVA, Katerina and PALOUSEK, David. Shape and dimensional analysis of lattice structures produced by selective laser melting. *MM Science Journal*. 2020. Vol. 2020, no. June, p. 3938–3942. DOI 10.17973/MMSJ.2020_06_2020013.

[41] GROSSMANN, Alexander, GOSMANN, Julian and MITTELSTEDT, Christian. Lightweight lattice structures in selective laser melting: Design, fabrication and mechanical properties. *Materials Science and Engineering: A*. 24 October 2019. Vol. 766. DOI 10.1016/j.msea.2019.138356.

[42] VRÁNA, Radek, CERVINEK, Ondrej, MANAS, Pavel, KOUTNÝ, Daniel and PALOUŠEK, David. Dynamic loading of lattice structure made by selective laser melting-numerical model with substitution of geometrical imperfections. *Materials*. 2018. Vol. 11, no. 11. DOI 10.3390/ma11112129.

[43] KEMPEN, K., THIJS, L., VAN HUMBEECK, J. and KRUTH, J. P. Mechanical Properties of AlSi10Mg Produced by Selective Laser Melting. In : *Physics Procedia*. Elsevier B.V., 2012. p. 439–446. DOI 10.1016/j.phpro.2012.10.059.

[44] MOYLAN, Shawn, SLOTWINSKI, John, COOKE, April, JURRENS, Kevin and DONMEZ, M. Alkan. An additive manufacturing test artifact. *Journal of Research of the National Institute of Standards and Technology*. 2014. Vol. 119, p. 429–459. DOI 10.6028/jres.119.017.

[45] MANCISIDOR, A. M., GARCIANDIA, F., SEBASTIAN, M. San, ÁLVAREZ, P., DÍAZ, J. and UNANUE, I. Reduction of the residual porosity in parts manufactured by selective laser melting using skywriting and high focus offset strategies. In : *Physics Procedia*. Elsevier B.V., 2016. p. 864–873. DOI 10.1016/j.phpro.2016.08.090.

[46] GIBSON, Lorna J. and ASHBY, Michael F. *Cellular Solids*. . Cambridge University Press, 1997. ISBN 9780521499118.

[47] CAMPOLI, G., BORLEFFS, M. S., AMIN YAVARI, S., WAUTHLE, R., WEINANS, H. and ZADPOOR, A. A. Mechanical properties of open-cell metallic biomaterials manufactured using additive manufacturing. *Materials and Design*. 2013. Vol. 49, p. 957–965. DOI 10.1016/j.matdes.2013.01.071.

[48] CWIEKA, Karol, WYSOCKI, Bartlomiej, SKIBINSKI, Jakub, CHMIELEWSKA, Agnieszka and SWIESZKOWSKI, Wojciech. Numerical design of open-porous titanium scaffolds for Powder Bed Fusion using Laser Beam (PBF-LB). *Journal of the Mechanical Behavior of Biomedical Materials*. 1 March 2024. Vol. 151. DOI 10.1016/j.jmbbm.2023.106359.

[49] LEARY, Martin, MAZUR, Maciej, ELAMBASSERIL, Joe, MCMILLAN, Matthew, CHIRENT, Thomas, SUN, Yingying, QIAN, Ma, EASTON, Mark and BRANDT, Milan. Selective laser melting (SLM) of AlSi12Mg lattice structures. *Materials and Design*. 15 May 2016. Vol. 98, p. 344–357. DOI 10.1016/j.matdes.2016.02.127.

[50] MAXWELL, J. Clerk. On the calculation of the equilibrium and stiffness of frames. *The London, Edinburgh, and Dublin Philosophical Magazine and Journal of Science*. 26 April 1864. Vol. 27, no. 182, p. 294–299. DOI 10.1080/14786446408643668.

[51] DESHPANDE, V.S., ASHBY, M.F. and FLECK, N.A. Foam topology: bending versus stretching dominated architectures. *Acta Materialia*. Online. April 2001. Vol. 49, no. 6, p. 1035–1040. DOI 10.1016/S1359-6454(00)00379-7.

[52] DONG, Zhichao, LIU, Yabo, LI, Weijie and LIANG, Jun. Orientation dependency for microstructure, geometric accuracy and mechanical properties of selective laser melting AlSi10Mg lattices. *Journal of Alloys and Compounds*. 30 June 2019. Vol. 791, p. 490–500. DOI 10.1016/j.jallcom.2019.03.344.

[53] TSOPANOS, S., MINES, R. A.W., MCKOWN, S., SHEN, Y., CANTWELL, W. J., BROOKS, W. and SUTCLIFFE, C. J. The influence of processing parameters on the mechanical properties of selectively laser melted stainless steel microlattice structures. *Journal of Manufacturing Science and Engineering*. 2010. Vol. 132, no. 4, p. 0410111–04101112. DOI 10.1115/1.4001743.

[54] ČERVINEK, Ondřej, WERNER, Benjamin, KOUTNÝ, Daniel, VAVERKA, Ondřej, PANTĚLEJEV, Libor and PALOUŠEK, David. Computational approaches of quasi-static compression loading of SS316L lattice structures made by selective laser melting. *Materials*. 1 May 2021. Vol. 14, no. 9. DOI 10.3390/ma14092462.

[55] VAVERKA, Ondřej, ČERVINEK, Ondřej, JAROŠ, Jan, KOUTNÝ, Daniel and PANTĚLEJEV, Libor. Numerical and Experimental Evaluation of Structured Material for Use in Multiscale Topology Optimization. *Advanced Engineering Materials*. 1 July 2024. Vol. 26, no. 13. DOI 10.1002/adem.202400127.

[56] ZHU, L., LI, N. and CHILDS, P. R.N. Light-weighting in aerospace component and system design. *Propulsion and Power Research*. 1 June 2018. Vol. 7, no. 2, p. 103–119. DOI 10.1016/j.jppr.2018.04.001.

[57] WILLIAMS, James C. and STARKE, Edgar A. Progress in structural materials for aerospace systems. *Acta Materialia*. 2003. Vol. 51, no. 19, p. 5775–5799. DOI 10.1016/j.actamat.2003.08.023.

[58] HEINZ, A., HASZLER, A., KEIDEL, C., MOLDENHAUER, S., BENEDICTUS, R. and MILLER, W. S. Recent development in aluminium alloys for aerospace applications. *Materials Science and Engineering: A*. 2000. Vol. 280, no. 1, p. 102–107. DOI 10.1016/S0921-5093(99)00674-7.

[59] XU, Weifeng, LUO, Yuxuan, ZHANG, Wei and FU, Mingwang. Comparative study on local and global mechanical properties of bobbin tool and conventional friction stir welded 7085-T7452 aluminum thick plate. *Journal of Materials Science and Technology*. Online. 2018. Vol. 34, no. 1, p. 173–184. DOI 10.1016/j.jmst.2017.05.015.

[60] ABOULKHAIR, Nesma T., MASKERY, Ian, TUCK, Chris, ASHCROFT, Ian and EVERITT, Nicola M. On the formation of AlSi10Mg single tracks and layers in selective laser melting: Microstructure and nano-mechanical properties. *Journal of Materials Processing Technology*. 2016. Vol. 230, p. 88–98. DOI 10.1016/j.jmatprotec.2015.11.016.

[61] KRUTH, J. P., LEVY, G., KLOCKE, F. and CHILDS, T. H.C. Consolidation phenomena in laser and powder-bed based layered manufacturing. *CIRP Annals - Manufacturing Technology*. 2007. Vol. 56, no. 2, p. 730–759. DOI 10.1016/j.cirp.2007.10.004.

[62] SUGIMOTO, Koichi, NIIYA, Kazunori, OKAMOTO, Taira and KISHITAKE, Katsuhiko. A Study of Damping Capacity in Magnesium Alloys. *Transactions of the Japan Institute of Metals*. Online. 1977. Vol. 18, no. 3, p. 277–288. DOI 10.2320/matertrans1960.18.277.

[63] FRIEDRICH, H and SCHUMANN, S. Research for a ``new age of magnesium'' in the automotive industry. *Journal of Materials Processing Technology*. November 2001. Vol. 117, no. 3, p. 276–281. DOI 10.1016/S0924-0136(01)00780-4.

[64] EASTON, Mark, BEER, Aiden, BARNETT, Matthew, DAVIES, Chris, DUNLOP, Gordon, DURANDET, Yvonne, BLACKET, Stuart, HILDITCH, Tim and BEGGS, Peter. Magnesium alloy applications in automotive structures. *JOM*. 13 November 2008. Vol. 60, no. 11, p. 57–62. DOI 10.1007/s11837-008-0150-8.

[65] KURZYNOWSKI, T., PAWLAK, A. and SMOLINA, I. The potential of SLM technology for processing magnesium alloys in aerospace industry. *Archives of Civil and Mechanical Engineering*. Online. 2020. Vol. 20, no. 1, p. 1–13. DOI 10.1007/s43452-020-00033-1.

[66] EDDY JAI POINERN, Gérrard, BRUNDAVANAM, Sridevi and FAWCETT, Derek. Biomedical Magnesium Alloys: A Review of Material Properties, Surface Modifications and Potential as a Biodegradable Orthopaedic Implant. *American Journal of Biomedical Engineering*. 7 January 2013. Vol. 2, no. 6, p. 218–240. DOI 10.5923/j.ajbe.20120206.02.

[67] YOU, Sihang, HUANG, Yuanding, KAINER, Karl Ulrich and HORT, Norbert. Recent research and developments on wrought magnesium alloys. *Journal of Magnesium and Alloys*. Online. 2017. Vol. 5, no. 3, p. 239–253. DOI 10.1016/j.jma.2017.09.001.

[68] MINÁRIK, Peter, KRÁL, Robert, ČÍŽEK, Jakub and CHMELÍK, František. Effect of different c/a ratio on the microstructure and mechanical properties in magnesium alloys processed by ECAP. *Acta Materialia*. 2016. Vol. 107, p. 83–95. DOI 10.1016/j.actamat.2015.12.050.

[69] GUAN, Dikai, RAINFORTH, W. Mark, MA, Le, WYNNE, Brad and GAO, Junheng. Twin recrystallization mechanisms and exceptional contribution to texture evolution during annealing in a magnesium alloy. *Acta Materialia*. 2017. Vol. 126, p. 132–144. DOI 10.1016/j.actamat.2016.12.058.

[70] CHEN, Junxiu, TAN, Lili, YU, Xiaoming, ETIM, Iniobong P., IBRAHIM, Muhammad and YANG, Ke. Mechanical properties of magnesium alloys for medical application: A review. *Journal of the Mechanical Behavior of Biomedical Materials*. Online. 2018. Vol. 87, no. April 2017, p. 68–79. DOI 10.1016/j.jmbbm.2018.07.022.

[71] AGHION, E., BRONFIN, B. and ELIEZER, D. The role of the magnesium industry in protecting the environment. *Journal of Materials Processing Technology*. 2001. Vol. 117, no. 3, p. 381–385. DOI 10.1016/S0924-0136(01)00779-8.

[72] YADROITSEV, I. and SMUROV, I. Surface morphology in selective laser melting of metal powders. *Physics Procedia*. Online. 2011. Vol. 12, no. PART 1, p. 264–270. DOI 10.1016/j.phpro.2011.03.034.

[73] SORKIN, A., TAN, J.L. and WONG, C.H. Multi-material modelling for selective laser melting. *Procedia Engineering*. Online. 2017. Vol. 216, p. 51–57. DOI 10.1016/j.proeng.2018.02.088.

[74] NASAB, Milad Hamidi, GASTALDI, Dario, LECIS, Nora Francesca and VEDANI, Maurizio. On morphological surface features of the parts printed by selective laser melting (SLM). *Additive Manufacturing*. Online. 2018. Vol. 24, no. July, p. 373–377. DOI 10.1016/j.addma.2018.10.011.

[75] SALEHI, Mojtaba, MALEKSAEEDI, Saeed, FARNOUSH, Hamidreza, NAI, Mui Ling Sharon, MEENASHISUNDARAM, Ganesh Kumar and GUPTA, Manoj. An investigation into interaction between magnesium powder and Ar gas: Implications for selective laser melting of magnesium. *Powder Technology*. Online. 2018. Vol. 333, p. 252–261. DOI 10.1016/j.powtec.2018.04.026.

[76] PAWLAK, Andrzej, ROSIENKIEWICZ, Maria and CHLEBUS, Edward. Design of experiments approach in AZ31 powder selective laser melting process optimization. *Archives of Civil and Mechanical Engineering*. January 2017. Vol. 17, no. 1, p. 9–18. DOI 10.1016/j.acme.2016.07.007.

[77] STAIGER, Mark P., PIETAK, Alexis M., HUADMAI, Jerawala and DIAS, George. Magnesium and its alloys as orthopedic biomaterials: A review. *Biomaterials*. 2006. Vol. 27, no. 9, p. 1728–1734. DOI 10.1016/j.biomaterials.2005.10.003.

[78] HARTWIG, Andrea. Role of magnesium in genomic stability. *Mutation Research - Fundamental and Molecular Mechanisms of Mutagenesis*. 2001. Vol. 475, no. 1–2, p. 113–121. DOI 10.1016/S0027-5107(01)00074-4.

[79] SARIS, Nils Erik L., MERVAALA, Eero, KARPPANEN, Heikki, KHAWAJA, Jahangir A. and LEWENSTAM, Andrzei. Magnesium: An update on physiological, clinical and analytical aspects. *Clinica Chimica Acta*. 2000. Vol. 294, no. 1–2, p. 1–26. DOI 10.1016/S0009-8981(99)00258-2.

[80] REVELL, P. A., DAMIEN, E., ZHANG, X. S., EVANS, P. and HOWLETT, C. R. The Effect of Magnesium Ions on Bone Bonding to Hydroxyapatite Coating on Titanium Alloy Implants. *Key Engineering Materials*. 2004. Vol. 254–256, p. 447–450. DOI 10.4028/www.scientific.net/kem.254-256.447.

[81] ZREIQAT, H., HOWLETT, C. R., ZANNETTINO, A., EVANS, P., SCHULZE-TANZIL, G., KNABE, C. and SHAKIBAEI, M. Mechanisms of magnesium-stimulated adhesion of osteoblastic cells to commonly used orthopaedic implants. *Journal of Biomedical Materials Research*. 2002. Vol. 62, no. 2, p. 175–184. DOI 10.1002/jbm.10270.

[82] LEVOROVA, Jitka, DUSKOVA, Jaroslava, DRAHOS, Milan, VRBOVA, Radka, VOJTECH, D., KUBASEK, Jiri, BARTOS, Martin, DUGOVA, Lenka, ULMANN, Dan and FOLTAN, Rene. In vivo study on biodegradable magnesium alloys: Bone healing around WE43 screws. *Journal of Biomaterials Applications*. 2018. Vol. 32, no. 7, p. 886–895. DOI 10.1177/0885328217743321.

[83] GE, Shuping, WANG, Yi, TIAN, Jie, LEI, Daoxi, YU, Qingsong and WANG, Guixue. An in vitro study on the biocompatibility of WE magnesium alloys. *Journal of Biomedical Materials Research - Part B Applied Biomaterials*. 2016. Vol. 104, no. 3, p. 482–487. DOI 10.1002/jbm.b.33388.

[84] VAN DER STOK, Johan, VAN DER JAGT, Olav P., AMIN YAVARI, Saber, DE HAAS, Mirthe F.P., WAARSING, Jan H., JAHR, Holger, VAN LIESHOUT, Esther M.M., PATKA, Peter, VERHAAR, Jan A.N., ZADPOOR, Amir A. and WEINANS, Harrie. Selective laser melting-produced porous titanium scaffolds regenerate bone in critical size cortical bone defects. *Journal of Orthopaedic Research*. 2013. Vol. 31, no. 5, p. 792–799. DOI 10.1002/jor.22293.

[85] NG, C. C., SAVALANI, M. M., MAN, H. C. and GIBSON, I. Layer manufacturing of magnesium and its alloy structures for future applications. *Virtual and Physical Prototyping*. 2010. Vol. 5, no. 1, p. 13–19. DOI 10.1080/17452751003718629.

[86] NG, Chi Chung, SAVALANI, Monica and MAN, Hau Chung. Fabrication of magnesium using selective laser melting technique. *Rapid Prototyping Journal*. 2011. Vol. 17, no. 6, p. 479–490. DOI 10.1108/13552541111184206.

[87] NG, C. C., SAVALANI, M. M., LAU, M. L. and MAN, H. C. Microstructure and mechanical properties of selective laser melted magnesium. *Applied Surface Science*. 2011. Vol. 257, no. 17, p. 7447–7454. DOI 10.1016/j.apsusc.2011.03.004.

[88] SAVALANI, Monica Mahesh and PIZARRO, Jorge Martinez. Effect of preheat and layer thickness on selective laser melting (SLM) of magnesium. *Rapid Prototyping Journal*. 2016. Vol. 22, no. 1, p. 115–122. DOI 10.1108/RPJ-07-2013-0076.

[89] HU, Dong, WANG, Yong, ZHANG, Dingfei, HAO, Liang, JIANG, Junjie, LI, Zhonghua and CHEN, Yitao. Experimental Investigation on Selective Laser Melting of Bulk Net-Shape Pure Magnesium. *Materials and Manufacturing Processes*. Online. 2015. Vol. 30, no. 11, p. 1298–1304. DOI 10.1080/10426914.2015.1025963.

[90] ZHANG, Baicheng, LIAO, Hanlin and CODDET, Christian. Effects of processing parameters on properties of selective laser melting Mg–9%Al powder mixture. *Materials & Design*. February 2012. Vol. 34, p. 753–758. DOI 10.1016/j.matdes.2011.06.061.

[91] WEI, Kaiwen, GAO, Ming, WANG, Zemin and ZENG, Xiaoyan. Effect of energy input on formability, microstructure and mechanical properties of selective laser melted AZ91D magnesium alloy. *Materials Science and Engineering: A*. August 2014. Vol. 611, p. 212–222. DOI 10.1016/j.msea.2014.05.092.

[92] SUCHY, Jan, HORYNOVÁ, Miroslava, KLAKURKOVÁ, Lenka, PALOUSEK, David, KOUTNY, Daniel and CELKO, Ladislav. Effect of Laser Parameters on Processing of Biodegradable Magnesium Alloy WE43 via Selective Laser Melting Method. *Materials*. 9 June 2020. Vol. 13, no. 11, p. 2623. DOI 10.3390/ma13112623.

[93] SONG, Bo, DONG, Shujuan, DENG, Sihao, LIAO, Hanlin and CODDET, Christian. Microstructure and tensile properties of iron parts fabricated by selective laser melting. *Optics & Laser Technology*. March 2014. Vol. 56, p. 451–460. DOI 10.1016/j.optlastec.2013.09.017.

[94] ATTAR, H., CALIN, M., ZHANG, L. C., SCUDINO, S. and ECKERT, J. Manufacture by selective laser melting and mechanical behavior of commercially pure titanium. *Materials Science and Engineering A*. Online. 2014. Vol. 593, p. 170–177. DOI 10.1016/j.msea.2013.11.038.

[95] ATTAR, Hooyar, BÖNISCH, Matthias, CALIN, Mariana, ZHANG, Lai Chang, SCUDINO, Sergio and ECKERT, Jürgen. Selective laser melting of in situ titanium-titanium boride composites: Processing, microstructure and mechanical properties. *Acta Materialia*. 2014. Vol. 76, p. 13–22. DOI 10.1016/j.actamat.2014.05.022.

[96] YAP, C. Y., CHUA, C. K., DONG, Z. L., LIU, Z. H., ZHANG, D. Q., LOH, L. E. and SING, S. L. Review of selective laser melting: Materials and applications. *Applied Physics Reviews*. Online. 2015. Vol. 2, no. 4. DOI 10.1063/1.4935926.

[97] YADROITSEV, I., KRAKHMALEV, P. and YADROITSAVA, I. Hierarchical design principles of selective laser melting for high quality metallic objects. *Additive Manufacturing*. Online. 2015. Vol. 7, p. 45–56. DOI 10.1016/j.addma.2014.12.007.

[98] NIU, H. J. and CHANG, I. T.H. Instability of scan tracks of selective laser sintering of high speed steel powder. *Scripta Materialia*. 1999. Vol. 41, no. 11, p. 1229–1234. DOI 10.1016/S1359-6462(99)00276-6.

[99] COLLUR, M. M., PAUL, A. and DEBROY, T. Mechanism of alloying element vaporization during laser welding. *Metallurgical Transactions B*. 1987. Vol. 18, no. 4, p. 733–740. DOI 10.1007/BF02672891.

[100] WEI, Kaiwen, WANG, Zemin and ZENG, Xiaoyan. Influence of element vaporization on formability, composition, microstructure, and mechanical performance of the selective laser melted Mg-Zn-Zr components. *Materials Letters*. Online. 2015. Vol. 156, p. 187–190. DOI 10.1016/j.matlet.2015.05.074.

[101] RONNEBERG, Tobias, DAVIES, Catrin M. and HOOPER, Paul A. Revealing relationships between porosity, microstructure and mechanical properties of laser powder bed fusion 316L stainless steel through heat treatment. *Materials and Design*. 1 April 2020. Vol. 189. DOI 10.1016/j.matdes.2020.108481.

[102] SHIFENG, Wen, SHUAI, Li, QINGSONG, Wei, YAN, Chunze, SHENG, Zhang and YUSHENG, Shi. Effect of molten pool boundaries on the mechanical properties of selective laser melting parts. *Journal of Materials Processing Technology*. 2014. Vol. 214, no. 11, p. 2660–2667. DOI 10.1016/j.jmatprotec.2014.06.002.

[103] ESMAILY, M., ZENG, Z., MORTAZAVI, A. N., GULLINO, A., CHOUDHARY, S., DERRA, T., BENN, F., D'ELIA, F., MÜTHER, M., THOMAS, S., HUANG, A., ALLANORE, A., KOPP, A. and BIRBILIS, N. A detailed microstructural and corrosion analysis of magnesium alloy WE43 manufactured by selective laser melting. *Additive Manufacturing*. Online. 2020. Vol. 35, no. April, p. 101321. DOI 10.1016/j.addma.2020.101321.

[104] GUAGLIONE, Fabio, CAPRIO, Leonardo, PREVITALI, Barbara and DEMIR, Ali Gökhan. Single point exposure LPBF for the production of biodegradable Zn-alloy lattice structures. *Additive Manufacturing*. 1 December 2021. Vol. 48. DOI 10.1016/j.addma.2021.102426.

[105] SHI, Yangyang, GUO, Kai, SHI, Hao, HUANG, Xiaoming, YANG, Bin and SUN, Jie. Effects of process parameters on microstructure properties of WE43 magnesium alloy by selective laser melting. *Materials Today Communications*. 1 June 2024. Vol. 39. DOI 10.1016/j.mtcomm.2024.109151.

[106] FRIEDRICH, H and SCHUMANN, S. Research for a “new age of magnesium” in the automotive industry. *Journal of Materials Processing Technology*. November 2001. Vol. 117, no. 3, p. 276–281. DOI 10.1016/S0924-0136(01)00780-4.

[107] OTSU, Nobukyuki. A threshold selection method from gray-level histograms. *IEEE transactions on systems, man, and cybernetics*. January 1979.

[108] METEL, Alexander S., STEBULYANIN, Michael M., FEDOROV, Sergey V. and OKUNKOVA, Anna A. Power Density Distribution for Laser Additive Manufacturing (SLM): Potential, Fundamentals and Advanced Applications. *Technologies*. 1 March 2019. Vol. 7, no. 1. DOI 10.3390/technologies7010005.

[109] JAHEDI, Mohammad, MCWILLIAMS, Brandon A., MOY, Paul and KNEZEVIC, Marko. Deformation twinning in rolled WE43-T5 rare earth magnesium alloy: Influence on strain hardening and texture evolution. *Acta Materialia*. 1 June 2017. Vol. 131, p. 221–232. DOI 10.1016/j.actamat.2017.03.075.

[110] MANI, Gopinath, FELDMAN, Marc D., PATEL, Devang and AGRAWAL, C. Mauli. *Coronary stents: A materials perspective*. March 2007.

LIST OF FIGURES AND TABLES

9.1 List of figures

9.2 List of tables

LIST OF ABBREVIATIONS AND SYMBOLS

PBF-LB / LPBF	Laser beam powder bed fusion
SLM	Selective laser melting
E_{lin} / LE	Linear energy
E_{area} / AE	Area energy
E_{vol}	Volume energy
LP	Laser power
LS	Laser speed
HD	Hatch distance
OL	Overlap
LT	Layer thickness
CD	Contour distance
TW	Track width
HT	Track thickness of hollow struts
WW	Weld width
2W	Hollow strut with two welds
BC	Beam compensation
PCD	First peripheral contour track
SD	Strut diameter
V	Vertical strut
IN	Inclined strut
2D	Two dimensional
3D	Three dimensional
TPMS	Triply periodic minimal surface
BCC	Body-centered cubic
FCC	Face-centered cubic
BCCZ	Body-centered cubic with vertical struts
CT	Computed tomography
µCT	Micro-computed tomography
E	Elastic modulus
UTS	Ultimate tensile strength
YS	Yield strength

EL	Elongation
Young’s modulus	YM
RSA	Response surface analysis
DOE	Design of experiment
FEA	Finite element analysis
SEM	Scanning electron microscopy
EDS	Energy-dispersive X-ray spectrometer
DIC	Digital 3D image correlation
CS	Contour strategy
Hatch + skywriting	Hatch strategy with skywriting
Contour - hatch	Combination of contour and hatch strategies
Contour – hatch + skywriting	Combination of contour and hatch strategies with skywriting
RE	Rare earth

www.ustavkonstruovani.cz